

Responses of the Climate System to Opposing Solar and CO₂ Forcings

Rick Russotto

A dissertation
submitted in partial fulfillment of
the requirements for the degree of

Doctor of Philosophy

University of Washington

2018

Reading Committee:

Thomas P. Ackerman, Chair

Philip Rasch

Robert Wood

Program Authorized to Offer Degree:
Department of Atmospheric Sciences

©Copyright 2018

Rick Russotto

University of Washington

Abstract

Responses of the Climate System to Opposing Solar and CO₂ Forcings

Rick Russotto

Chair of the Supervisory Committee:
Professor Thomas P. Ackerman
Department of Atmospheric Sciences

This thesis analyzes various aspects of the response of Earth's climate to a simultaneously imposed increase in atmospheric CO₂ concentrations and decrease in the solar constant, based on an analysis of experiment G1 of the Geoengineering Model Intercomparison Project. I particularly focus on changes in meridional temperature gradients, tropical precipitation, cloud fraction, the atmosphere's radiative balance, and the seasonal cycle, and I propose and evaluate a theory for the amount of solar constant reduction required to maintain global mean temperature under increased CO₂.

The atmosphere transports less heat from the tropics to the poles in G1 than in preindustrial conditions, which implies that the phenomenon of polar warming and tropical cooling in G1 must be directly caused by the imposition of a net negative forcing in the tropics and a net positive forcing in high latitudes. Damping of the polar warming by the reduction in energy transport helps to explain why most of the polar amplification of warming in quadrupled-CO₂ experiments is canceled in G1. Changes in cross-equatorial energy transport by the atmosphere help account for the inter-model spread in tropical rain shifts in G1. Radiative effects of changes in clouds are the largest source of inter-model spread in changes in meridional energy transport.

The required solar constant reduction to achieve energy balance G1 is between 3.2% and

5.0%, depending on the model, and is uncorrelated with the models' equilibrium climate sensitivity, while a formula from the experiment specifications based on the models' effective CO₂ forcing and planetary albedo is well correlated with but consistently underpredicts the required solar reduction. I propose instead that the required solar reduction should be equal to the sum of the instantaneous CO₂ forcing and the shortwave and longwave radiative adjustments to the combined forcing. To test this hypothesis, I analyze changes in cloud fraction and the atmospheric profile of temperature and humidity, and I quantify the radiative effects of these changes at the top of atmosphere. Low cloud fraction decreases in all models in G1, likely due to reductions in boundary layer inversion strength over the ocean and plant physiological responses to increased CO₂ over land. High cloud fraction increases in the global mean in most models. Among the various radiative adjustments, there are strong warming effects due to reductions in low cloud fraction and upper tropospheric and stratospheric cooling. Reductions in water vapor roughly offset the tropospheric temperature effect, while cloud changes have little effect in the longwave. Taken together, the sum of the diagnosed radiative adjustments and the CO₂ instantaneous forcing predicts the required solar forcing in G1 to within about 6%.

The seasonal migration of the tropical precipitation median is damped in G1, due to preferential cooling of the summer hemisphere by the solar reduction. The amplitude of the seasonal temperature cycle is reduced in much of the troposphere due to reductions in insolation and water vapor concentrations. There is an increase in seasonal temperature amplitude in parts of the stratosphere. Implications of this work for efforts to understand the climate response to solar forcings and for the possibility of testing and implementing solar geoengineering are discussed in the concluding chapter.

TABLE OF CONTENTS

	Page
List of Figures	iii
List of Tables	vii
Chapter 1: Introduction	1
1.1 Science questions	3
1.2 Prior publication	4
1.3 Overview of GeoMIP and list of models	4
1.4 Review of global mean precipitation changes under CO ₂ and solar forcings	7
Chapter 2: Meridional energy transport, tropical precipitation, and polar amplification	12
2.1 Energy and moisture transport changes	14
2.2 Attribution of changes using a moist energy balance model	24
2.3 Chapter conclusions	40
Chapter 3: Changes in clouds and atmospheric physical properties and implications for required solar reduction	44
3.1 Temperature and humidity profiles	47
3.2 Cloud fraction profiles and maps	51
3.3 Predictors of low cloud changes	54
3.4 Radiative effects	61
3.5 Theory of required solar reduction	69
3.6 Chapter conclusions	73
Chapter 4: Changes in the seasonal cycle	76
4.1 Changes in the seasonal migration of the ITCZ	76
4.2 Changes in the amplitude of the seasonal temperature cycle	82

Chapter 5: Conclusions and implications	87
5.1 Implications for future modeling work into CO ₂ and solar forcings	88
5.2 Implications for the possibility of solar geoengineering	91
Bibliography	95
Appendix A: Results from Ch. 2 using a dry instead of a moist EBM	113
Appendix B: Time series plots of APRP results	120

LIST OF FIGURES

Figure Number	Page
2.1 Northward energy transport (PW) for G1 minus piControl, poleward of 30° N (a-c) and 30° S (d-f), for total moist static energy transport (a, d), latent energy transport (b, e) and dry static energy transport (c, f), in various GeoMIP models and the multi-model mean.	18
2.2 As in Figure 2.1 but for abrupt4xCO2 minus piControl.	19
2.3 Zonal mean temperature changes relative to piControl for G1 (a) and abrupt4xCO2 (b), and analogous zonal mean saturation vapor pressure changes (c,d), in various GeoMIP models and multi-model mean. (a) and (b) are similar to panels of Figure 1 of Kravitz <i>et al.</i> (2013a), but I show only the models analyzed here, and I use a y-axis scaling that shows more detail for G1 - piControl.	20
2.4 Shift in the ITCZ in GeoMIP models for G1 minus piControl, plotted against change in northward MSE transport across the equator (a) and northern hemisphere mean surface temperature change minus southern hemisphere mean temperature change (b). The quantity r is the correlation coefficient.	22
2.5 Scatter plots of surface air temperature vs. clear-sky outgoing longwave radiation in piControl (monthly means, years 1-40) for each of the 8 models included in the EBM analysis. Shown is linear fit line used to fit the coefficients a and b	28
2.6 Energy flux into atmosphere input into moist EBM, calculated from the GCM pi-Control output (years 1-40) using Equation 2.10.	29
2.7 Meridional energy transport changes calculated by moist EBM (x -axis) versus those diagnosed from the GCM output (y -axis). (a): northward energy transport across the equator, for G1 minus piControl; (b): poleward energy transport changes across 40° N and S, for G1 minus piControl; (c): as in (b) but for abrupt4xCO2 minus pi-Control.	30
2.8 EBM energy input terms, minus the piControl EI, for the all_G1 experiment (a) and six attribution experiments in the G1 - piControl case (b-g), calculated using Equations 2.11 through 2.17. Experiment names following Table 2.3. Multi-model mean maps of the perturbations calculated using APRP (panels b-d) are shown in Figure 3.8.	34
2.9 As in Figure 2.8 but for abrupt4xCO2 minus piControl.	35

2.10 Changes in northward cross-equatorial energy transport calculated by moist EBM for G1 minus piControl in various attribution experiments.	36
2.11 As in Figure 2.10 but for changes in poleward atmospheric energy transport across 40° N (a) and 40° S (b), for G1 minus piControl.	37
2.12 As in Figure 2.11 but for abrupt4xCO ₂ minus piControl.	39
3.1 Percent solar constant reduction for models running the G1 experiment, versus (a) equilibrium climate sensitivity in the models, from <i>Sherwood et al.</i> (2014), and (b) solar constant reduction predicted by Equation 3.2, based on effective radiative forcing values from <i>Sherwood et al.</i> (2014) and piControl planetary albedo values from <i>Kravitz et al.</i> (2013a). CESM-CAM5.1-FV and CSIRO-Mk3L-1-2 are excluded from this figure because these models were not included in <i>Sherwood et al.</i> (2014).	45
3.2 Zonal mean temperature change for G1 minus piControl in each model as a function of pressure.	49
3.3 Zonal mean change in the natural log of specific humidity for G1 minus piControl in each model as a function of pressure.	50
3.4 Zonal mean change in cloud fraction for G1 minus piControl in each model as a function of pressure, or height for HadGEM2-ES. To help comparisons with other models, the vertical axis for HadGEM2-ES is scaled according to $e^{-z/8000}$ m (where z is height), which is approximately proportional to pressure.	51
3.5 Multi-model mean, zonal mean change in cloud fraction for G1 minus piControl. HadGEM2-ES excluded because of different coordinate system. Hatching indicates areas where fewer than 8 of 10 models agree on sign of change. Plotted layers correspond to values archived at the pressure level at the bottom of each layer.	53
3.6 Multi-model mean changes in low (a), middle (b), and high (c) cloud fraction for G1 - piControl. Hatching indicates areas where fewer than 9 of the 11 models agree on the sign of the change.	55
3.7 Multi-model mean changes in EIS (a) and LTS (b) for G1 - piControl. Hatching indicates areas where fewer than 7 of 9 models agree on the sign of the change. CSIRO-Mk3L-1-2 and MPI-ESM-LR models are excluded from this plot because near-surface specific humidity output, which is required to calculate EIS, was not available.	57
3.8 Multi-model mean change in net downward SW radiation at the TOA in G1 - piControl due to changes in cloud properties (a), non-cloud atmospheric absorption and scattering (b), and surface albedo (c), calculated using APRP method (<i>Taylor et al.</i> , 2007). Hatching indicates areas where fewer than 7 of 9 models agree on the sign of the change. CSIRO-Mk3L-1-2 and GISS-E2-R models are excluded because not all fields necessary for APRP were correctly archived.	63

3.9 Multi-model mean change in OLR in G1 - piControl due to changes in atmospheric temperature (a), surface temperature (b), and specific humidity (c), calculated using radiative kernels (<i>Shell et al.</i> , 2008). Hatching indicates areas where fewer than 9 of 11 models agree on the sign of the change.	66
3.10 Multi-model mean change in LW cloud radiative effect in G1 - piControl, corrected for cloud masking of LW air temperature, surface temperature and water vapor adjustments and CO ₂ forcing. Positive values indicate a decrease in OLR, <i>i.e.</i> a warming effect. Hatching indicates areas where fewer than 9 of 11 models agree on the sign of the change.	68
3.11 Excess required solar radiative forcing in G1 vs. that expected from effective CO ₂ forcing (black bar), global mean SW and LW radiative adjustments (colored bars), and sum of all the radiative adjustments (gray bar), in models for which all of these quantities were calculated. For all except F_{excess} , positive values indicate a warming effect (increase in absorbed SW radiation or reduction in OLR). The first three colored bars correspond to the SW radiative adjustments calculated using APRP (multi-model mean maps shown in Figure 3.8). The three blue and green bars correspond to the LW radiative adjustments calculated using radiative kernels (multi-model mean maps shown in Figure 3.9). The magenta bar corresponds to the change in LW cloud radiative effect, corrected for cloud masking effects using radiative kernels (multi-model mean map shown in Figure 3.10).	70
3.12 As in Figure 3.11 but with excess solar forcing calculated using instantaneous instead of effective CO ₂ radiative forcing. Navy blue bar indicates the reduction in OLR due to stratospheric temperature adjustment from CO ₂ quadrupling given by <i>Zhang and Huang</i> (2014), to illustrate the portion of the atmospheric temperature adjustment to G1 attributable to stratospheric cooling.	71
4.1 (a): Monthly ITCZ deviation from annual mean position in multi-model mean, in G1 (years 11-50) and piControl (years 1-40). (b): Difference between G1 and piControl ITCZ deviation from annual mean in each month, in each of 11 GeoMIP models. Thick line is the multi-model mean difference. The mean of the 12 monthly means was subtracted from each month's position before multi-model mean calculations or difference between runs were taken. 11 GeoMIP models were included in this calculation (all models listed in Table 1.2 except CSIRO-Mk3L-1-2).	78

4.2 ITCZ position in each model in piControl (years 1-40) and G1 (years 11-50). For each model, there are two rows of three dots, one for piControl and one for G1. In each row, the left dot is the JFM (January, February and March) average position, the middle dot is the annual mean position, and the right dot is the JAS (July, August and September) position. The length of the horizontal line connecting the dots shows the extent of the ITCZ seasonal migration; this migration is damped in every model in G1 compared with piControl. This figure was contributed to <i>Smyth et al. (2017)</i> (Figure 10).	80
4.3 ITCZ shift in G1 minus piControl scattered against northern hemisphere warming relative to southern hemisphere in (a) annual mean, (b) boreal summer (JAS) mean, and (c) boreal winter (JFM) mean. Panel (a) is the same as Figure 2.4b except that a slightly different set of models is used here. This figure was contributed to <i>Smyth et al. (2017)</i> (Figure 9).	81
4.4 Amplitude (a) and phase (b) of the seasonal cycle of zonal mean temperature in an example model, CCSM4, and multi-model mean change in amplitude in G1 - piControl (c) and abrupt4xCO ₂ (d). For (c) and (d), stippling indicates where fewer than 9 of 11 models agree on the sign of the change.	84
A.1 Meridional energy transport changes calculated by dry EBM (<i>x</i> -axis) versus those diagnosed from the GCM output (<i>y</i> -axis). (a): northward energy transport across the equator, for G1 minus piControl; (b): poleward energy transport changes across 40° N and S, for G1 minus piControl; (c): as in (b) but for abrupt4xCO ₂ minus piControl. <i>cf.</i> Figure 2.7.	115
A.2 Changes in northward cross-equatorial energy transport calculated by dry EBM for G1 minus piControl in various attribution experiments. <i>cf.</i> Figure 2.10. The “all_G1” experiment was called “G1-full” when this plot was made. OLR fit coefficients in the “greenhouse” and “G1-full” experiments involved re-fitting both the slope and intercept of the OLR- T_s fit (Table A.1), versus only the intercept for the version in Chapter 2 (Table 2.2).	116
A.3 As in Figure A.2 but for changes in poleward atmospheric energy transport across 40°N (a) and 40°S (b), for G1 minus piControl. <i>cf.</i> Figure 2.11.	117
A.4 As in Figure A.3 but for abrupt4xCO ₂ minus piControl. <i>cf.</i> Figure 2.12.	118
B.1 Global mean SW radiative responses calculated using APRP for each year of G1 minus the piControl baseline, in each of nine models.	121

LIST OF TABLES

Table Number	Page
1.1 Publications corresponding to specific sections	4
1.2 Models included in the thesis, with references, institutions, solar constant reduction in the G1 experiment (ΔS_0), and global mean surface air temperature change in G1 - piControl (ΔT). Global mean temperature differences were calculated by me. Solar constant reductions for most models are taken from Table 2 of <i>Kravitz et al.</i> (2013a). For the CSIRO model, I calculated the solar constant reduction from the TOA downward SW flux fields in G1 and piControl. The values of ΔS_0 and ΔT listed for BNU-ESM are from a new realization, r3i1p1, that has a greater solar constant reduction and better compensates global mean temperature than the original; Duoying Ji provided to me the solar constant reduction for this model. The original BNU realization had a solar constant reduction of 3.8%, which did not adequately restore global mean temperature, so I excluded the BNU model from Chapter 2, for which I did the analysis before the new realization was available. Chapter 3 and Section 4.2 include the new BNU realization. Section 4.1 includes the old BNU realization, due to my coauthors' prior decision to include that model in the <i>Smyth et al.</i> (2017) paper. Two of the models originally participating in G1 had very limited output available. Of these, HadCM3 is included only in Section 4.1, and EC-Earth (<i>Hazeleger et al.</i> , 2012) is excluded entirely. The rest of the listed models are included in most or all parts of the analysis; exceptions due to unavailable or corrupted variables are noted locally in the text or figure captions.	6
2.1 Northward energy transport residual error at north pole in different models and runs, to 4 decimal places.	17
2.2 Values of fit coefficients for clear-sky OLR as a function of temperature for use in moist EBM analysis.	27
2.3 Summary of attribution experiments run with moist energy balance model.	31
3.1 Global mean changes in low, middle and high cloud fraction in G1 minus piControl.	56

3.2 Global mean radiative adjustments in G1 minus piControl, and excess and total solar forcing in G1, in W m^{-2} . Positive values indicate a warming effect (increase in absorbed SW radiation or decrease in OLR), except for solar forcing where positive values represent a cooling. SW adjustments correspond to multi-model means plotted in Figure 3.8. LW adjustments correspond to multi-model means plotted in Figures 3.9 and 3.10, with sign flipped for Figure 3.9. “Sum” is the sum of all the SW and LW adjustments. F_{excess} is calculated using Equation 3.13 and represents the actual instantaneous solar forcing (F_{solar}) in G1 minus that predicted based on CO ₂ effective or instantaneous forcing. F_{solar} represents the total instantaneous solar forcing calculated from theory (Equation 3.15) or actually used in G1 (Equation 3.16).	64
A.1 Values of fit coefficients for clear-sky OLR as a function of temperature used in the original EBM analysis, when I re-fit both a and b instead of just b	114

ACKNOWLEDGMENTS

First and foremost, I want to express my gratitude to my advisor, Tom Ackerman, for the support he has shown me over the past six years. Tom has always paid attention to my well-being as a student and as a person, from supporting my decision to switch topics from tropical cirrus clouds to geoengineering, to encouraging me to maintain a healthy work-life balance, to making sure I got a more powerful work computer when my existing one wasn't up to the job. I believe my writing has improved significantly as a result of Tom's very thorough comments on my papers. He has always supported my travel to scientific conferences, which were indispensable for obtaining feedback on my work, and he even sent me to a geoengineering policy conference in Oxford when he could not go. Over the past few months, I've been particularly grateful to Tom for providing valuable guidance on my postdoc search, something some advisors are reluctant to do, and for patiently writing reference letters for many different positions as the search continued to drag on. Tom has been a very highly respected scientist dating back to his work on topics like nuclear winter early in his career, and I consider it an honor and a privilege to have been able to work with him.

I also want thank my other committee members for their efforts. Phil Rasch made sure to take the time to meet with me during his visits to Seattle from Pacific Northwest National Laboratory, and always had very insightful questions on my work that challenged me to think through the logic of my assertions more carefully. Phil also helped me obtain model output that I needed and wrote letters for my postdoc applications. Rob Wood, who also served on my Master's committee, has consistently been available as a resource for advice and feedback on my work and on cloud physics and geoengineering-related topics in general. Dargan Frierson suggested several research directions that proved very fruitful, provided valuable insights from

past work on similar topics by his group, and insisted on a rigorous treatment of certain issues that ultimately strengthened and improved the study in Chapter 2.

I have had a number of research collaborators outside the department whom I want to acknowledge. Trude Storelvmo, my undergraduate thesis advisor, encouraged me to apply to UW for grad school in the first place. When we later met up at a GeoMIP workshop in Oslo, she suggested a collaboration with her student, Jane Smyth, which led to the work on the seasonal cycle shown in Section 4.1. Trude also wrote letters for my postdoc applications. I also enjoyed working with Stephen Gardiner and Alex Lenferna in the UW Philosophy department on an interdisciplinary paper on ethics of testing geoengineering, which is discussed in Section 5.2. Ben Kravitz served as a mentor during my month-long stint at PNNL in 2015, when I was just getting started studying geoengineering and analyzing climate model output. Ben has since been instrumental in providing needed model output and helping with various technical issues.

I have benefited greatly from the many grad student friends on whom I've been able to rely for advice, collaboration, and support, including my classmates who entered the department in 2012—Trevor Morgan, Kim Nighelli, Lee Picard, Greg Quetin, Viral Shah, and Matthew Woelfle—and our counterparts in physical oceanography, Sarah Dewey and Earle Wilson; my officemates, including Kelly McCusker, Marysa Laguë, Joe Zagrodnik, Jennifer DeHart, Kelsey Larson, Lauren Schmeisser, Fiona Lo, and Lucas Vargas Zeppetello; recent members of Tom's and Roger Marchand's research groups, particularly Tra Dinh, Stu Evans, Ben Hillman, Andrew Geiss, Wei Zhao, Litai Kang and Emily Tansey; and other friends including Jonathan Weyn, Steph Rushley, and too many others to list here. Students here are eager to share their technical and computing knowledge, which has helped me to break many logjams I've encountered in research, and I especially appreciate the Python workshops run by Jeremy McGibbon and Andre Perkins, which helped me transition from Matlab to Python and learn version control. I also thank the people who have been active in our UAW chapter for helping to ensure that Seattle remains affordable for grad students and that we are treated fairly.

This department is truly remarkable for its collegiality and for prioritizing students' well-being. I appreciate the hard work by the faculty and staff that goes into keeping it that way. The faculty here are excellent at teaching, and I'm grateful that I got the broad and deep education in atmospheric science that I wanted to get out of grad school. The department staff have also done much to make my life easier, and I've been especially helped out by Erica Coleman and Jennifer Weiss, and by Collen Marquist at JISAO, who has helped me track down Tom many times when I needed to find him.

My doctoral study was funded by the US Department of Defense (DoD) through the National Defense Science and Engineering Graduate Fellowship (NDSEG) Program through August 2016, and subsequently by a grant to JISAO from the Fund for Innovative Climate and Energy Research. The portions of this thesis that are published have benefited from the helpful comments of anonymous reviewers. For their roles in producing, coordinating, and making available the CMIP5 and GeoMIP model output, I acknowledge the climate modeling groups listed in Table 1.2, the World Climate Research Programme's (WCRP) Working Group on Coupled Modelling (WGCM), and the Global Organization for Earth System Science Portals (GO-ESSP). Duoying Ji, Helene Muri, Ulrike Niemeier, Stephen Phipps and Jin-Ho Yoon helped me obtain model output that was not yet available online. Yen-Ting Hwang provided Matlab codes that formed the basis of the APRP and EBM analyses in this thesis. Kyle Armour, Eui-Seok Chung, Aaron Donohoe, Blaž Gasparini, Cristian Proistosescu, Brian Rose, Karen Shell, Balwinder Singh, and Ashly Spevacek all provided helpful information and feedback in various ways.

Finally, I want to express my appreciation for my family's love and support during my time at UW, especially my parents, who provided financial and logistical help for my move to the opposite corner of the country, hosted me back at home many times during breaks, and were always willing to listen and provide advice when I needed it. I am looking forward to being close enough to come home for Thanksgiving again after I move to New York for my postdoc.

(This page intentionally left blank.)

Chapter 1

INTRODUCTION

The temperature of Earth is governed by the balance between the absorption of radiation emitted by the sun and the emission of radiation by Earth's atmosphere and surface. The solar radiation is mostly in the visible, near infrared, and ultraviolet regions of the electromagnetic spectrum, and is referred to as "shortwave" (SW) radiation. The radiation emitted by the Earth is in the thermal infrared region and is referred to as "longwave" (LW) radiation. Earth's surface is warmer than it would be in the absence of an atmosphere because of the absorption and re-emission of LW radiation by atmospheric gases and clouds, an effect known as the greenhouse effect. Due to concerns (to put it lightly) about fossil fuel combustion causing LW-absorbing gases such as carbon dioxide (CO_2) to accumulate in the atmosphere, strengthening the greenhouse effect and warming the planet, the response of Earth's climate to changes in LW radiation has been extensively studied (e.g. *IPCC*, 2013). Not as much attention has been paid to the response to changes in absorbed SW radiation, and much of what has been done on the SW side been motivated by understanding prehistoric climates in which the sun was weaker (*Feulner*, 2012) or ruling out changes in the strength of the sun as the cause of the observed global warming (e.g. *Santer et al.*, 2003).

In the absence of progress in curbing global emissions of greenhouse gases—for example, atmospheric CO_2 concentrations increased by a record amount in 2016 (*World Meteorological Organization*, 2017)—there has been increasingly serious discussion about the possibility of artificially increasing the percentage of reflected sunlight in order to cool the Earth, bringing new urgency to understanding the response of the climate to SW forcings. Such albedo modification efforts, along with the possibilities of directly removing CO_2 from the atmosphere and seeding cirrus clouds to reduce their absorption of LW radiation (*Mitchell and Finnegan*, 2009), are re-

ferred to as “geoengineering” or “climate engineering”. Proposals to reflect more sunlight are sometimes referred to as “solar radiation management”, or SRM, but this term is controversial because it prematurely implies that solar radiation can in fact be managed, so I will refer to them as “solar geoengineering”. The most commonly discussed solar geoengineering methods include injecting reflective aerosols, usually sulfates, into the stratosphere (e.g. *Crutzen*, 2006), and marine cloud brightening (MCB), which involves spraying sea salt aerosols into the marine boundary layer in order to increase the albedo of clouds (e.g. *Latham et al.*, 2012). Putting mirrors in space to reduce the sunlight reaching Earth is often mentioned as a less realistic but more idealized representation of the idea of solar geoengineering, but *Bewick et al.* (2012) argue that this could actually be done by extracting dust from an asteroid and placing it at the L1 Lagrange point between Earth and the sun. Solar geoengineering, particularly stratospheric aerosol injection, has been argued to be quickly deployable and much cheaper than reducing CO₂ emissions (e.g. *Keith*, 2013), but also carries a number of risks (e.g. *Robock*, 2008), for example that rapid warming would follow abrupt termination (*Robock et al.*, 2008; *Jones et al.*, 2013; *McCusker et al.*, 2014). Also, solar geoengineering would attempt to compensate for a LW forcing with a SW forcing, meaning that even if global mean temperature could be held constant, many other aspects of the climate response to increased greenhouse gases would not be perfectly compensated.

In order to better understand how solar geoengineering would affect Earth’s climate, experiments simulating solar geoengineering have been run with global climate models (GCMs), starting with the single-model studies by *Govindasamy and Caldeira* (2000) and *Govindasamy et al.* (2003). More recently, multiple climate models have been run for the same geoengineering experiments, in an international effort known as the Geoengineering Model Intercomparison Project (GeoMIP; *Kravitz et al.*, 2011a). The simplest of the GeoMIP experiments is called the G1 experiment, in which the CO₂ concentration is abruptly quadrupled relative to preindustrial levels and the solar constant, or the flux of solar radiation impinging on the top of Earth’s atmosphere (TOA), is simultaneously reduced by an amount that maintains TOA energy balance and therefore keeps global mean temperature approximately at preindustrial. The G1 setup most lit-

erally represents the space mirrors idea, and approximates the global SW effects of other forms of solar geoengineering. The forcing (enough to compensate a CO₂ quadrupling) is much larger than what most would seriously propose actually doing in the real world; the scientific community has largely reached a consensus that solar geoengineering cannot simply be a substitute for cutting CO₂ emissions, and much of the discussion has focused on temporary deployments intended to limit the rate of warming (*MacMartin et al.*, 2014) or to cap the total amount of warming until elimination of greenhouse gas emissions is achieved (*Tilmes et al.*, 2016). Imposing such a large forcing in the models, however, has the advantage of providing a large signal with which to identify ways in which the two forcings do not fully compensate each other, and the imposition of equal and opposite forcings is a fascinating scenario from a theoretical perspective even irrespective of geoengineering considerations.

In this thesis I analyze the GeoMIP G1 model output to answer some unresolved questions about the behavior of the climate in this scenario, and explore the implications for understanding the climate response to solar forcings and the possibility of testing and implementing solar geoengineering.

1.1 Science questions

This thesis is focused on the following questions, each of which corresponds to a chapter.

In the GeoMIP G1 experiment:

1. What happens to meridional energy transport, and how does this affect regional precipitation and the meridional temperature gradient?
2. How do cloud fraction and other physical properties of the atmosphere change? What are the radiative effects of these changes, and how do they affect the required solar constant reduction?
3. How is the seasonal cycle of precipitation and temperature affected?

1.2 Prior publication

Table 1.1 lists where, if anywhere, the work in different sections is published. The sections that are published are very similar to the published versions but contain additional figures, methodological details, and other material that did not make it into the papers. Unpublished figures in the published sections include Figures 2.5, 2.6, 2.8, 2.9, 3.5, and 4.1. Some parts of the introductions and conclusions of the published papers have been incorporated into Chapters 1 and 5, respectively. For the paper with Jane Smyth and Trude Storelvmo where I was the second author, only portions for which I was directly responsible are included in the thesis.

Table 1.1: Publications corresponding to specific sections

Section	Reference
Chapter 2	<i>Russotto and Ackerman</i> (2018a)
Chapter 3	<i>Russotto and Ackerman</i> (2018b) (in review)
Section 4.1	<i>Smyth et al.</i> (2017)
Section 4.2	Unpublished
Appendices	Unpublished

1.3 Overview of GeoMIP and list of models

Before getting into my investigations of the specific scientific questions, I want to describe the GeoMIP experiments in more detail, list the included models, and discuss some methodological considerations common to all the chapters.

Experiment G1 was designed to be compared to two runs from the Coupled Model Intercomparison Project, Phase 5 (CMIP5; *Taylor et al.*, 2012): piControl, in which the models were run for hundreds of years at preindustrial conditions, and abrupt4xCO₂, in which CO₂ was abruptly quadrupled relative to preindustrial but the solar constant was unchanged. I have generally followed this approach, plotting differences in multi-annual means between G1 and

piControl to show the effect of the combined forcings on various aspects of the climate. I have also plotted the differences between abrupt4xCO₂ and piControl, to see how the variables are changed in a climate warmed by increased CO₂ without any compensating forcing. In most cases this was just to verify that I could reproduce previous work, and I have not included these plots in the thesis except where relevant.¹ G1 was run out for at least 50 years in each model, and abrupt4xCO₂ typically for 150 years. Following the precedent set by *Kravitz et al.* (2013a), I have averaged quantities over years 11-50 of the G1 experiment, to average out interannual variability while excluding transient effects that occur in the first few years of the simulation. I have also averaged over years 11-50 in abrupt4xCO₂, and over the first 40 available years in piControl.²

Table 1.2 lists the models that are included in my analysis. All of the models were run with a full dynamical ocean coupled to the atmosphere. Some models were excluded from certain portions of the analysis because necessary output files were not available or were corrupted. The percent solar constant reduction in G1 in each model, which is listed in Table 1.2, was tuned for each model to achieve a TOA energy balance within 0.1 W m⁻² (*Kravitz et al.*, 2011b; *Schmidt et al.*, 2012). The tuning procedure, and my proposed theory explaining the inter-model differences in this amount, is discussed in detail in Chapter 3. All of the models achieved a global mean surface air temperature in G1 within 0.3 K of preindustrial, as shown in the last column of Table 1.2.³

Besides G1, there were three other experiments in the first phase of GeoMIP, described by *Kravitz et al.* (2011a). While my analysis is entirely focused on G1, I sometimes refer to the other experiments when suggesting future research directions. In G2, CO₂ is increased at 1% per year

¹As another sanity check, I also plotted the climatologies of many variables in piControl to make sure the values were reasonable; most of these plots are not included in the thesis.

²The model output was reported starting with the models' ocean and atmospheric circulations already having been spun up.

³I did not calculate this quantity for HadCM3 because it is not included in most of my analysis, but zonal mean temperature difference plots (*Kravitz et al.*, 2013a) suggest that it was reasonably well compensated.

Table 1.2: Models included in the thesis, with references, institutions, solar constant reduction in the G1 experiment (ΔS_0), and global mean surface air temperature change in G1 - piControl (ΔT). Global mean temperature differences were calculated by me. Solar constant reductions for most models are taken from Table 2 of *Kravitz et al.* (2013a). For the CSIRO model, I calculated the solar constant reduction from the TOA downward SW flux fields in G1 and piControl. The values of ΔS_0 and ΔT listed for BNU-ESM are from a new realization, r3i1p1, that has a greater solar constant reduction and better compensates global mean temperature than the original; Duoying Ji provided to me the solar constant reduction for this model. The original BNU realization had a solar constant reduction of 3.8%, which did not adequately restore global mean temperature, so I excluded the BNU model from Chapter 2, for which I did the analysis before the new realization was available. Chapter 3 and Section 4.2 include the new BNU realization. Section 4.1 includes the old BNU realization, due to my coauthors' prior decision to include that model in the *Smyth et al.* (2017) paper. Two of the models originally participating in G1 had very limited output available. Of these, HadCM3 is included only in Section 4.1, and EC-Earth (*Hazeleger et al.*, 2012) is excluded entirely. The rest of the listed models are included in most or all parts of the analysis; exceptions due to unavailable or corrupted variables are noted locally in the text or figure captions.

Model	Reference	Institution	ΔS_0	ΔT (K)
BNU-ESM	<i>Ji et al.</i> (2014)	Beijing Normal University	4.4%	0.025
CanESM-2	<i>Arora et al.</i> (2011)	Canadian Centre for Climate Modeling and Analysis	4.0%	-0.013
CCSM4	<i>Gent et al.</i> (2011)	National Center for Atmospheric Research	4.1%	0.233
CESM-CAM5.1-FV	<i>Hurrell et al.</i> (2013)	National Center for Atmospheric Research	4.7%	-0.157
CSIRO-Mk3L-1-2	<i>Phipps et al.</i> (2011)	Commonwealth Scientific and Industrial Research Organization/ Bureau of Meteorology	3.2%	0.034
GISS-E2-R	<i>Schmidt et al.</i> (2014)	NASA Goddard Institute for Space Studies	4.5%	-0.292
HadCM3	<i>Gordon et al.</i> (2000)	Met Office Hadley Centre	4.1%	
HadGEM2-ES	<i>Collins et al.</i> (2011)	Met Office Hadley Centre	3.9%	0.241
IPSL-CM5A-LR	<i>Dufresne et al.</i> (2013)	Institut Pierre Simon Laplace	3.5%	0.109
MIROC-ESM	<i>Watanabe et al.</i> (2011)	Atmosphere and Ocean Research Institute (The University of Tokyo), National Institute for Environmental Studies, and Japan Agency for Marine-Earth Science and Technology	5.0%	-0.065
MPI-ESM-LR	<i>Giorgetta et al.</i> (2013)	Max Planck Institute for Meteorology	4.7%	-0.011
NorESM1	<i>Bentsen et al.</i> (2013)	Bjerknes Centre for Climate Research, Norwegian Meteorological Institute	4.0%	-0.044

for 50 years, while the solar constant is linearly reduced⁴ to keep the global mean temperature

⁴This works because the radiative forcing of CO₂ is proportional to the logarithm of CO₂ concentration.

the same. G3 and G4 are intended to be more realistic experiments, in which greenhouse gas concentrations follow the IPCC's RCP4.5 scenario and solar geoengineering is applied through the model's aerosol treatment rather than by reducing the solar constant. In G3, aerosols are injected into the tropical lower stratosphere at a rate sufficient to approximately balance the RCP4.5 radiative forcing increase between 2020 and 2070, and in G4, SO₂ is injected at a rate of 5 teragrams per year between 2020 and 2070. Experiments G2, G3, and G4 also include a 20-year period at the end in order to investigate what happens when SCE is abruptly terminated while CO₂ concentrations remain elevated.

Initial analyses of G1 and G2 showed a consensus among the models regarding several properties of the response to SCE that had previously been seen in studies involving only one or several models. These included that the tropics are cooled and the poles are warmed relative to preindustrial (*Kravitz et al.*, 2013a); that precipitation decreases in the global mean (*Tilmes et al.*, 2013); and that sudden termination of SCE under elevated CO₂ leads to abrupt warming (*Jones et al.*, 2013). Experiments G3 and G4 were more problematic because of the great variety in the treatment of aerosols between the different models. As a result, a different version of G4, called G4SSA (for "specified stratospheric aerosols"), was run in which stratospheric aerosols were specified in terms of concentrations, rather than emissions (*Tilmes et al.*, 2015). Three additional experiments, described by *Kravitz et al.* (2013b), were performed that simulate MCB scenarios. Looking further ahead, a 2nd phase of GeoMIP will make use of the next generation of GCMs in coordination with CMIP Phase 6 (*Kravitz et al.*, 2015a).

1.4 Review of global mean precipitation changes under CO₂ and solar forcings

This section contains a review of the causes for changes in global mean precipitation under CO₂ and solar forcings, adapted from the proposal for my dissertation work. While planning for my thesis I realized that this issue is fairly well addressed in the existing literature, so I did not make this an investigative question of my thesis. I include a review of this literature here because it provides useful context for the subsequent chapters. Existing literature more directly related to my own work is reviewed within the subsequent chapters.

1.4.1 CO₂ forcing

A good starting point for understanding the effects of CO₂-induced warming on precipitation is the paper by *Held and Soden* (2006). Their most cited result is that global mean precipitation increases more slowly than water vapor in GCMs. Column-integrated water vapor increases at roughly 7.5% per K of surface warming, following the scaling given by the Clausius-Clapeyron relation (which gives saturation vapor pressure as a function of temperature) if relative humidity (RH) is held approximately constant. Global mean precipitation, on the other hand, increases at only about 1% or 2% per K. These numbers were fairly robust across 20 GCMs in future warming and historical simulations run for the 4th Assessment Report of the Intergovernmental Panel on Climate Change (IPCC).

In the global mean, precipitation must balance evaporation, because the atmosphere's capacity to store water is extremely limited compared to the fluxes of water in and out of the atmosphere. This means that precipitation is constrained by the surface energy budget. Held and Soden identified the following reasons for the increase in global mean evaporation (and therefore precipitation) with warming: (1) radiative effects of increased CO₂ on the surface holding the atmospheric state constant; (2) radiative effects of the increase in water vapor with warming, holding RH constant; (3) decreases in surface albedo (presumably owing to ice loss and forestation); and (4) decreases in the Bowen ratio, or the ratio of sensible heat flux to latent heat flux. The first 3 of these terms serve to increase the net downward flux of radiation at the surface, which must be balanced by increases in sensible and latent heat flux. Since the Bowen ratio decreases, the latent heat flux must increase, which implies greater global mean precipitation. Held and Soden used the GFDL AM2 atmospheric GCM to isolate each of these effects and concluded that none of them can keep up with the Clausius-Clapeyron scaling.

The reduction in global mean precipitation under global warming conditions can also be understood from an atmospheric energy budget perspective, since, at equilibrium, the energy released to the atmosphere by condensation or deposition of water vapor (and by surface sensible heat fluxes) must be balanced by the net radiative cooling of the atmosphere. *Pendergrass*

and Hartmann (2014) use this perspective to explain why precipitation increases more slowly than specific humidity with global warming, and show that differences in the change in the net atmospheric radiative cooling rate are responsible for the inter-model spread in precipitation changes.

Unlike in fully coupled or slab ocean simulations, precipitation actually decreases in GCM runs in which CO₂ is increased but sea surface temperatures (SSTs) are held constant (*Mitchell*, 1983; *Yang et al.*, 2003); these types of simulations are sometimes thought of as analogous to the G1 scenario. One explanation for this is that increased LW absorption by CO₂ reduces the net atmospheric cooling rate, which forces there to be less latent heat release by precipitation formation (*Bala et al.*, 2008). An alternative explanation, given by *Andrews and Forster* (2010) who cite *Dong et al.* (2009) for it, is that heating the atmosphere but not the ocean increases stability, which suppresses convective precipitation. *Andrews and Forster* (2010) argue that this mechanism also suppresses precipitation in transient climate change simulations, in which CO₂ increases gradually with time, because the atmosphere heats up faster than the ocean does, owing to the ocean's high heat capacity. They call this the “fast response” of precipitation to greenhouse gases, to distinguish it from the “slow response” (the equilibrium response), in which precipitation is enhanced. Note that arguments for precipitation changes based on surface energy balance cannot be applied to fixed-SST simulations; fixing SSTs artificially imposes a heat sink at the surface, so we cannot explain changes in surface latent heat flux based on changes in absorbed radiation at the surface in this context.

1.4.2 Solar forcing

Wetherald and Manabe (1975) were the first to use a general circulation model to study the effects of changing the solar constant on climate.⁵ They found that increasing the solar constant resulted in a dramatic increase in precipitation. This is a result of an increase in the net down-

⁵This was an atmospheric general circulation model but not a global climate model, as it only contained 1/6 of the globe. It also did not consider oceanic heat transport and had an idealized ocean/continent configuration. Nonetheless, the results are still relevant today from a theoretical perspective.

ward surface radiation, in both the SW (as a direct result of the solar constant increase) and the LW, for two reasons: (1) the atmospheric water vapor content increases due to the temperature increase, which increases the downward longwave radiation from the atmosphere; and (2) the atmospheric lapse rate decreases with warming due to the tropical atmosphere following a moist adiabatic temperature profile, and this increases atmospheric emission relative to surface emission. This increase in downward radiative flux is balanced primarily by an increase in latent heat flux, therefore increasing precipitation.⁶ In a solar geoengineering scenario, in which incoming sunlight was reduced, the signs of each of these terms would be reversed.

More recently, *Bala et al.* (2008) studied the effects of solar geoengineering on precipitation using a fully coupled atmosphere-ocean global climate model (the Community Climate Model, version 3), in an experiment similar to G1. They ran three equilibrium simulations: one in which CO₂ was doubled relative to a baseline concentration of 355 ppmv; one in which the solar constant was cut by 1.8%; and a “stabilized” case in which both of these changes were applied in order to keep the global mean temperature constant. There was an increase in precipitation in the doubled-CO₂ run, as expected, but there was a larger decrease in precipitation in the reduced-sunlight run, and a decrease in precipitation in the stabilized case. *Bala et al.* (2008) argue that the radiative flux changes at the surface are greater for the solar forcing case, resulting in a reduction in global mean precipitation when the two forcings are combined.

In the GeoMIP era, a wealth of new model output has become available to study precipitation changes with solar geoengineering. *Kravitz et al.* (2013c) examined the change in each of the terms of the surface energy budget between G1 and the CMIP5 preindustrial control experiment in the multi-model mean (see their Figure 1b). The net surface downward SW radiation was reduced by about 5 W m⁻², while the surface sensible heat flux had negligible changes. About 25% of the reduction in SW flux was balanced by a reduction in the net upward LW flux; the rest is balanced by a reduction in latent heat flux, which constrains global mean precipitation. *Kravitz et al.* (2013c) also examined the atmospheric energy budget, and found that the

⁶Since the Bowen ratio, or the ratio of sensible to latent heat flux, is small in the global mean, most of the compensation for surface radiative flux changes is manifest as a change in evaporation.

changes in global mean precipitation could be explained by the sum of changes in radiative flux convergence into the atmosphere and changes in sensible heat.

Solar constant reduction experiments underestimate the precipitation reduction compared to model runs that increase the concentration of sulfate aerosols in the stratosphere, as shown by *Niemeier et al.* (2013), in a single-model study, and *Ferraro and Griffiths* (2016), for the GeoMIP G3 and G4 experiments. This is best understood through the atmospheric energy perspective: sulfate aerosols absorb LW radiation, which reduces the net atmospheric radiative cooling rate and therefore allows for less precipitation.

Chapter 2

MERIDIONAL ENERGY TRANSPORT, TROPICAL PRECIPITATION, AND POLAR AMPLIFICATION

Two important issues related to the feasibility and risks of solar geoengineering are whether the polar amplification of CO₂-induced warming can be fully counteracted, and whether regional precipitation patterns will shift, exacerbating flooding in some areas and drought in others (*Irvine et al.*, 2010). Polar amplification is the phenomenon in which the poles warm by more than the tropics when atmospheric CO₂ concentrations are increased. While the reasons for polar amplification are not yet completely understood, it has already been observed in the instrumental temperature record (*Bekryaev et al.*, 2010) and is a robust behavior in climate models (*Holland and Bitz*, 2003). Since reflecting sunlight would affect the tropics more strongly than the poles, it has been hypothesized that it would reduce the meridional temperature gradient (*Keith and Dowlatabadi*, 1992), leading to tropical cooling and polar warming under the combined CO₂ and geoengineering forcings. I refer to this effect as “residual polar amplification”. Early model simulations of solar geoengineering scenarios, involving a simultaneous CO₂ increase and solar constant decrease (*Govindasamy and Caldeira*, 2000; *Govindasamy et al.*, 2003), found that the residual polar amplification was relatively small, with meridional temperature gradients looking much more like the preindustrial climate than the climate under increased CO₂ without geoengineering. However, some residual polar amplification still occurs as a robust feature of these types of model experiments (e.g. *Kravitz et al.*, 2013a).

Questions about shifts in regional precipitation under solar geoengineering are motivated by evidence from paleoclimate data and climate model studies that if one hemisphere is preferentially warmed, the intertropical convergence zone (ITCZ) shifts toward that hemisphere (e.g. *Broccoli et al.*, 2006). Model studies have shown that such an effect could occur for changes in

many different variables that affect the inter-hemispheric albedo contrast, such as high-latitude ice cover (*Chiang and Bitz*, 2005), mid-latitude forest extent (*Swann et al.*, 2012; *Lagu  and Swann*, 2016), and tropospheric sulfate aerosol concentration (*Hwang et al.*, 2013). In the context of solar geoengineering, *Haywood et al.* (2013) demonstrated that preferentially injecting reflective aerosols into one hemisphere shifts the ITCZ towards the other hemisphere, causing drought in some tropical areas. Even under a hemispherically symmetric solar geoengineering deployment, such as space-based mirrors (represented by a solar constant reduction), ITCZ shifts can still occur (*Smyth et al.*, 2017).

Both polar amplification and ITCZ shifts are closely related to the meridional transport of energy by the atmosphere, which makes atmospheric energy transport an important aspect of the effects of solar geoengineering to study. The sensitivity of the ITCZ, in particular, to energy transport in the atmosphere and ocean in present and future climates has recently been a topic of great research interest. Studies with slab ocean models with imposed hemispherically asymmetric energy fluxes (*Kang et al.*, 2008; *Yoshimori and Broccoli*, 2008) found that an anomalous Hadley circulation transports energy from the warmed hemisphere across the equator, shifting the ITCZ towards the warmed hemisphere (because moisture is transported by the lower branch of the Hadley cell, while energy is transported by the upper branch). However, later studies (*Kay et al.*, 2016; *Hawcroft et al.*, 2017) found that this effect is substantially weaker in GCM simulations that include a full ocean circulation coupled to the atmosphere. This is because an anomalous wind-driven ocean circulation develops in response to changes in the atmospheric Hadley circulation, allowing the ocean to do most of the work of transporting the excess energy in one hemisphere across the equator (*Green and Marshall*, 2017). Still, we can consider the ITCZ position in the framework of the atmosphere and take ocean heat transport and storage into account via surface energy fluxes.

In this chapter, I build off the methods of a particular set of studies of atmospheric energy transport in projects in which multiple GCMs were run for the same global warming scenarios scenarios. *Hwang and Frierson* (2010) showed that poleward transport of atmospheric moist static energy (MSE) increases under increased CO₂ concentrations in Coupled Model Inter-

comparison Project, Phase 3 (CMIP3) models. They used a moist energy balance model (EBM) to attribute the change in MSE transport across 40° latitude to different forcing and feedback terms, and found that cloud feedbacks are responsible for most of the inter-model spread in this quantity. *Hwang et al.* (2011) found that poleward dry static energy (DSE) transport in mid-to-high latitudes decreases with warming due to the reduced equator-to-pole temperature gradient (since warming is amplified at the poles), but moisture transport increases due to the overall warming combined with the nonlinearity of the Clausius-Clapeyron equation and the increase in moisture transport is enough to lead to an increase in MSE transport overall. *Frierson and Hwang* (2012) found that shifts in the ITCZ with warming in the CMIP3 slab ocean ensemble are anticorrelated with changes in atmospheric energy transport across the equator, with cloud feedbacks again being the largest source of uncertainty.

Here I apply similar methods to the GeoMIP G1 experiment to investigate changes in meridional energy transport under solar geoengineering, the factors responsible for these changes, and the associated effects on tropical precipitation and residual polar amplification. Section 2.1 describes the energy and latent heat transport changes that occur in the G1 and abrupt4xCO₂ experiments. Section 2.2 attributes these energy transport changes to different forcing and feedback terms, using the moist energy balance model (EBM) of *Hwang and Frierson* (2010).

2.1 Energy and moisture transport changes

Using the TOA and surface energy and moisture fluxes from the GeoMIP GCM experiments, I calculate changes in the meridional transport of MSE by the atmosphere. By subtracting the MSE transport in piControl from that in G1, we can understand how the combined CO₂ increase and solar constant decrease affect MSE transport, or, in other words, how well solar reductions can restore preindustrial patterns of atmospheric energy transport. For comparison, I also examine how the CO₂ increase alone affects MSE transport by subtracting the MSE transport in piControl from that in abrupt4xCO₂.

2.1.1 Details of GCM-derived energy transport calculations

I calculate the energy flux into the atmosphere from the GCM output as the sum of terms on the right-hand side of the following energy budget equation:

$$\nabla \cdot F_M = R_{\text{net,TOA}}^{\downarrow} + R_{\text{net,surface}}^{\uparrow} + \text{SH} + \text{LH} \quad (2.1)$$

where F_M is the vertically integrated horizontal moist static energy flux, $R_{\text{net,TOA}}^{\downarrow}$ is the net downward radiative flux at the top of the atmosphere, $R_{\text{net,surface}}^{\uparrow}$ is the net upward radiative flux at the surface, SH is the net upward surface sensible heat flux, and LH is the net upward surface latent heat flux. Since the net energy flux into the atmospheric column must be balanced by energy transport out of the column, we can calculate the northward atmospheric moist static energy transport as a function of latitude by integrating $\nabla \cdot F_M$, first zonally and then cumulatively northward from the south pole. It is also useful to decompose the MSE transport into latent energy (moisture) transport and dry static energy (DSE) transport, in order to identify how moisture changes affect the total energy transport changes, following the methodology of *Hwang et al.* (2011). I calculate the latent energy transport from the latent heat flux and precipitation GCM output by integrating the following equation zonally and meridionally:

$$\nabla \cdot F_L = \text{LH} - L_v P \quad (2.2)$$

where F_L is the vertically integrated horizontal latent energy flux, L_v is the latent heat of vaporization of water and P is precipitation. I calculate the DSE transport by subtracting the latent energy transport from the MSE transport.

Often, there is a residual energy transport at the north pole, because the models' internal energy conservation involves terms that are not included in the reported fields energy flux fields, or else because the models used slightly different values of physical constants than I assumed. For some models (CCSM4, CESM-CAM5.1-FV, GISS-E2-R, HadGEM2-ES, MIROC-ESM and NorESM1-M), this error can be reduced or nearly eliminated by adding $L_f P_{\text{snow}}$ to the right side of Equation 2.1, where L_f is the latent heat of fusion of ice and P_{snow} is the mass flux of snowfall at the surface. This term accounts for the net energy flux into the atmosphere when

snow crystals form in the atmosphere and then melt on land or in the ocean. For the rest of the models, including this term increases the north pole residual, so I omitted it, assuming that this term had been already accounted for inside the latent heat flux output field.¹ Omitting this term in the first set of models as well did not significantly affect the results.

To correct for any remaining energy flux residual, I subtract the following error function E from the northward energy transport profile:

$$E(\phi) = \frac{N}{2} (1 + \sin(\phi)) \quad (2.3)$$

where ϕ is the latitude and N is the residual northward energy transport at the north pole. This correction function assumes that each unit area of Earth's surface contributes equally to the error. To demonstrate that the error is small, Table 2.1 shows the values of N in piControl and the change in N in the other 2 runs relative to piControl. The errors are generally small (< .15 PW), except for MIROC-ESM, but even in this case the difference in the error between the runs is still small (all models have error < .06 PW for G1 minus piControl, or .09 PW for abrupt4xCO₂ minus piControl). Once the correction in Equation 2.3 is applied, the energy transport residual should only affect the results (in terms of differences between runs) if the errors are spatially nonuniform and the spatial pattern of the error differs between the runs. Since even the total error differences are small between runs, these residuals should not be a significant source of error in this analysis.

2.1.2 Poleward transport in mid-latitudes

Changes in the zonal mean northward MSE, latent energy and dry static energy (DSE) transport for G1 minus piControl are shown in Figure 2.1. Poleward MSE transport in mid-latitudes is reduced under G1 in all 10 models included in this chapter² and, when decomposed into the latent and DSE components, both of these terms are reduced as well. Figure 2.2 shows the same

¹For consistency, I also subtract $L_f P_{\text{snow}}$ from the right side of Equation 2.2 (for moisture transport) in the models where I subtract it from the total MSE transport.

²BNU-ESM is excluded for reasons described in the caption of Table 1.2.

Table 2.1: Northward energy transport residual error at north pole in different models and runs, to 4 decimal places.

Model	N (piControl) (PW)	N (G1 - piControl) (PW)	N (abrupt4xCO ₂ - piControl) (PW)
CanESM-2	-0.0531	0.0411	0.0809
CCSM4	0.0162	-0.0025	0.0015
CESM-CAM5.1-FV	0.0172	-0.0138	0.0027
CSIRO-Mk3L-1-2	0.1429	-0.0093	0.0857
GISS-E2-R	0.0135	-0.0002	0.0033
HadGEM2-ES	-0.0270	0.0137	0.0164
IPSL-CM5A-LR	0.0373	-0.0549	0.0027
MIROC-ESM	-1.9135	0.0593	0.0734
MPI-ESM-LR	-0.1174	0.0526	-0.0515
NorESM1	0.0137	-0.00004	0.0027

calculations for abrupt4xCO₂ minus piControl. In this case, poleward DSE transport decreases but moisture transport increases by more than enough to compensate, leading to an increase in total MSE transport. This corroborates the result seen by *Held and Soden* (2006) and *Hwang et al.* (2011) in CMIP3 global warming scenarios.

To understand why the energy transport changes are different for global warming and geo-engineering conditions, I plotted zonal mean changes in temperature and saturation vapor pressure. Figures 2.3a,b show the zonal mean temperature change in G1 and abrupt4xCO₂ relative to preindustrial. (These are also plotted in Figure 1 of *Kravitz et al.* (2013a), but my plots include only the models analyzed here and, for G1, I use a smaller y -axis range to show more detail.) In G1, we see the canonical pattern of tropical cooling and polar warming (Figure 2.3a). There is warming everywhere in abrupt4xCO₂ but more so in the polar regions, especially the Arctic (Figure 2.3b). In both cases, this pattern of temperature change results in a weakening of the equator-to-pole temperature gradient and reduces the poleward transport of dry static

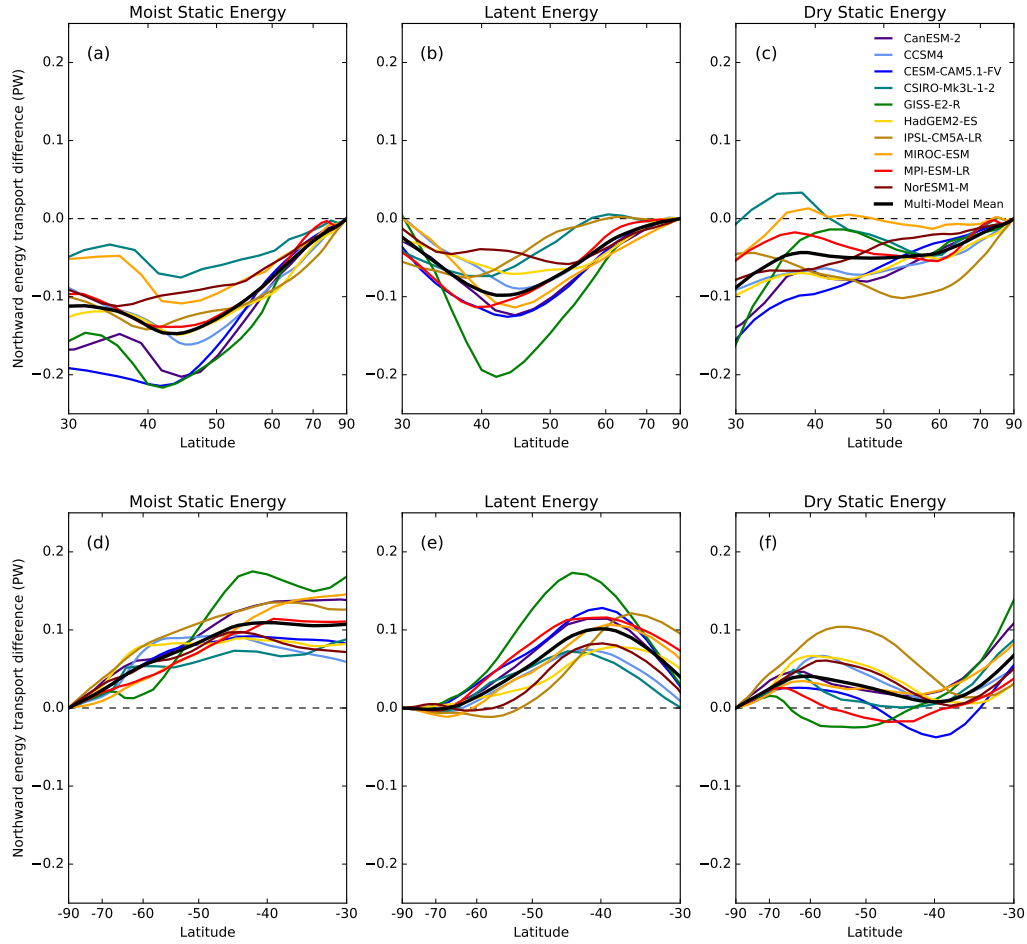


Figure 2.1: Northward energy transport (PW) for G1 minus piControl, poleward of 30° N (a-c) and 30° S (d-f), for total moist static energy transport (a, d), latent energy transport (b, e) and dry static energy transport (c, f), in various GeoMIP models and the multi-model mean.

energy (Figures 2.1c,f and 2.2c,f), similar to the result found by *Hwang et al.* (2011).

The mechanism for the difference in moisture transport is apparent from changes in saturation vapor pressure, e_s , which I calculate using an approximate form of the Clausius-Clapeyron

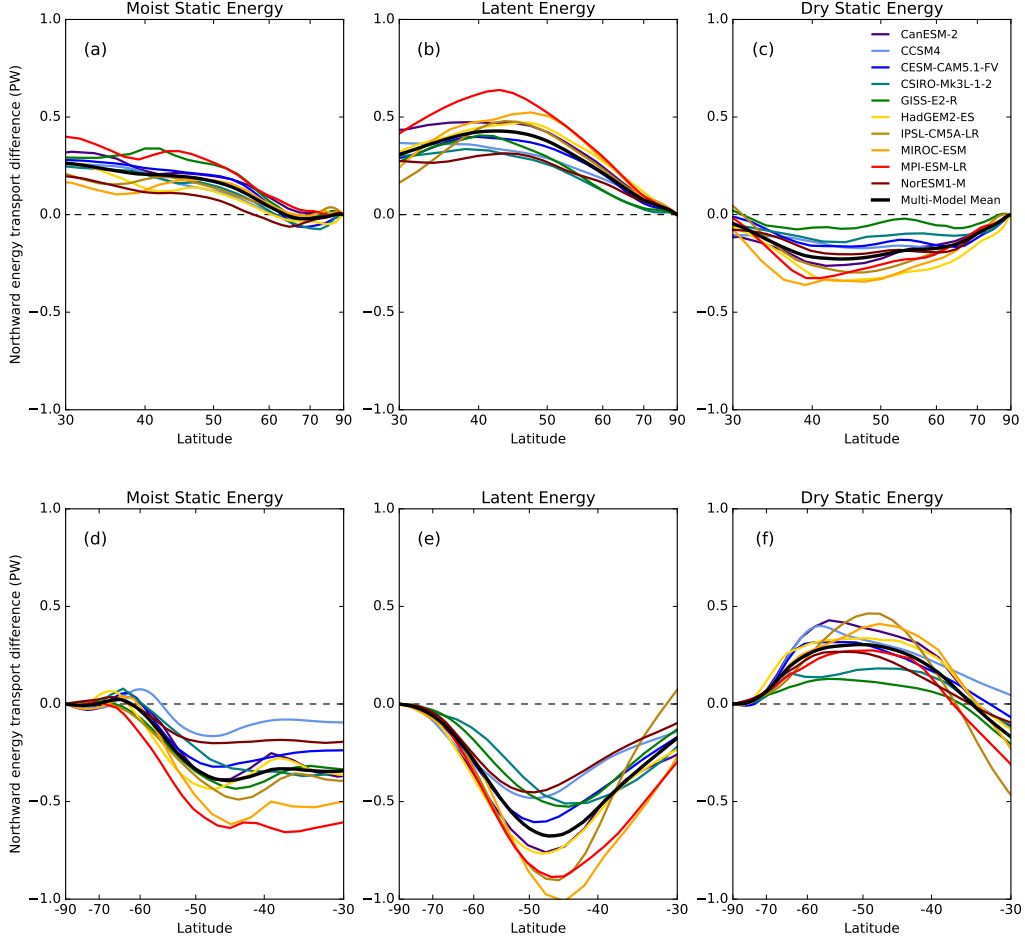


Figure 2.2: As in Figure 2.1 but for abrupt4xCO₂ minus piControl.

equation (e.g. Hartmann, 2016, eq. 1.11):

$$e_s = (6.11 \text{ hPa}) \exp \left\{ \frac{L_v}{R_v} \left(\frac{1}{273} - \frac{1}{T} \right) \right\} \quad (2.4)$$

where L_v is the latent heat of vaporization of water, R_v is the gas constant for water vapor, and T is the temperature in K. In abrupt4xCO₂ (Figure 2.3d), e_s increases more in the tropics than it does near the poles because e_s is approximately exponential with respect to temperature. A slight warming in the tropics leads to a larger increase in e_s because the tropics were initially warmer than the poles. In G1, however (Figure 2.3c), the tropics cool and the poles warm, so

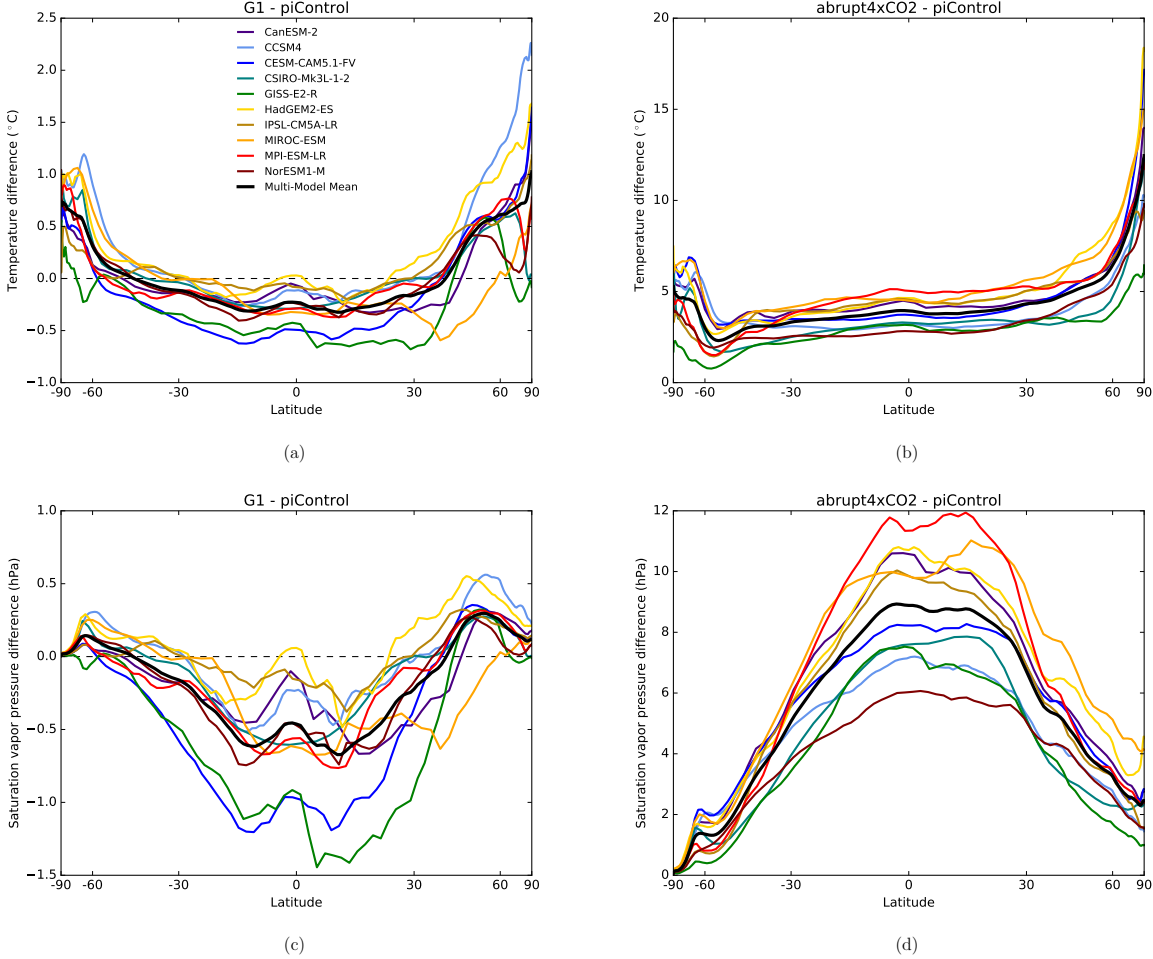


Figure 2.3: Zonal mean temperature changes relative to piControl for G1 (a) and abrupt4xCO2 (b), and analogous zonal mean saturation vapor pressure changes (c,d), in various GeoMIP models and multi-model mean. (a) and (b) are similar to panels of Figure 1 of Kravitz *et al.* (2013a), but I show only the models analyzed here, and I use a *y*-axis scaling that shows more detail for G1 - piControl.

saturation vapor pressure, like temperature, decreases in the tropics and increases (to a lesser extent) at high latitudes relative to piControl. Assuming the moisture content in the atmosphere scales with Clausius-Clapeyron, and the meridional winds are roughly the same, poleward moisture transport increases in abrupt4xCO2 and decreases in G1 because the equator-

to-pole moisture gradient has strengthened in abrupt4xCO₂ and weakened in G1.

A decrease in poleward energy transport has been previously reported in a single-model study running the G1 setup (*Schaller et al.*, 2014). In addition to a G1 experiment, that study also included runs which included only the CO₂ increase or solar constant decrease. The decrease in poleward energy transport in their G1 run is not equal to the sum of the increase in the “CO₂₊” run and the decrease in the “solar-” run in either hemisphere (see their Table 3). Also, the changes in poleward energy transport are not symmetrical in their solar increase and solar decrease runs. This indicates that the response of meridional MSE transport to various climate forcings is nonlinear, and we cannot simply add and subtract the responses to individual climate forcings to predict the responses to combined forcings. The nonlinearity of the Clausius-Clapeyron equation is a likely source of these nonlinear responses.

In G1, poleward MSE transport decreases, but the poles are still warmed relative to the tropics. This implies that the residual polar amplification in G1 must be due to the differing spatial patterns of the opposing solar and CO₂ forcings, with the solar forcing being greater in absolute magnitude in the tropics, where there is more sunlight to reduce. Local radiative feedbacks such as the ice-albedo feedback cannot be responsible for the residual polar amplification because these can only amplify or dampen a temperature change, but cannot reverse its sign. Another possible explanation would be an increase in ocean heat transport; I have not calculated this explicitly, but *Hong et al.* (2017) found that the Atlantic Meridional Overturning Circulation, which transports heat to the Arctic, slightly weakens in G1. While they only looked at heat transport in the Atlantic, there is a net decrease in energy flux into the ocean in the tropics (see Figure 2.8f and their Figure 4b), so there is no reason to expect an increase in poleward ocean heat transport. In addition, the poleward energy transport by the oceans is much less than that by the atmosphere at high latitudes (e.g. *Hawcroft et al.*, 2017, Figure 6), so small changes to it would not be expected to significantly affect the polar warming. This leaves the differing spatial patterns of the forcings as the only possible explanation for the polar warming and tropical cooling in G1.

The decrease in poleward MSE transport likely diminishes the polar warming in G1, rela-

tive to what would happen if forcings and feedbacks were allowed to operate locally but energy transport was fixed at piControl levels. It would be a useful avenue for future research to quantify the effect of reduced energy transport, as well as local feedbacks, on the polar warming in G1, similar to the study of Arctic amplification under global warming by *Pithan and Mauritsen* (2014). The reduction in poleward moisture transport may help explain the reduction in mid-latitude precipitation seen in *Tilmes et al.* (2013); quantifying this effect would also be a useful research direction.

2.1.3 Cross-equatorial energy transport and ITCZ shifts

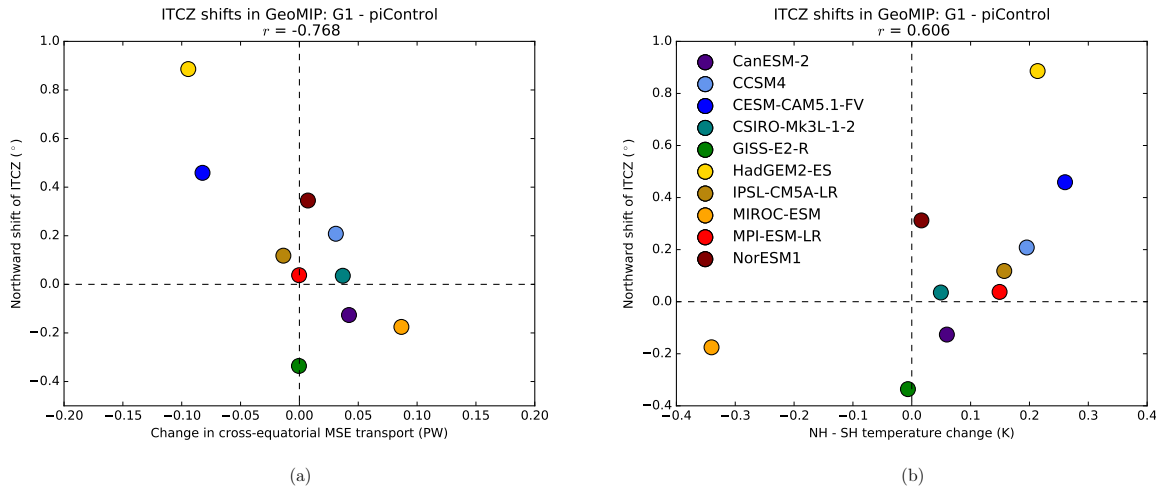


Figure 2.4: Shift in the ITCZ in GeoMIP models for G1 minus piControl, plotted against change in northward MSE transport across the equator (a) and northern hemisphere mean surface temperature change minus southern hemisphere mean temperature change (b). The quantity r is the correlation coefficient.

Figure 2.4a shows the relationship between shifts in the ITCZ in G1 relative to piControl and changes in the transport of moist static energy across the equator. For the ITCZ position, I use the latitude where half of the zonally integrated rainfall between 15°S and 15°N lies to the south

and half lies to the north, following *Hwang and Frierson* (2010). In the multi-model mean, the ITCZ shifts northward by 0.14 degrees, but there is significant inter-model spread, ranging from -0.33 to 0.89 degrees. A multi-model mean northward ITCZ shift is consistent with the result of *Viale and Merlis* (2017) that the ITCZ shifts northward by a greater amount for a CO₂ increase than for a solar constant increase in slab ocean aquaplanet GCM runs with a prescribed northward ocean heat transport that keeps the ITCZ in the northern hemisphere. However, caution must be taken in assuming that the results from CO₂ and solar forcing runs can be added linearly, for reasons discussed above. The ITCZ shifts in G1 are moderately anticorrelated with the change in cross-equatorial energy transport (correlation coefficient $r = -0.77$). Anticorrelation between these quantities is consistent with previous work (e.g. *Frierson and Hwang*, 2012; *Hwang et al.*, 2013), and is expected because the Hadley cell transports energy primarily in its upper branch but moisture primarily in its lower branch. The anticorrelation implies that understanding the causes of changes in cross-equatorial energy transport in G1 will also be helpful for understanding the reasons for the inter-model spread in ITCZ shifts therein.

For abrupt4xCO₂, there is no correlation between shifts in the precipitation-median ITCZ and cross-equatorial energy transport ($r = 0.07$; not shown). There are several possible reasons for this, and for the fact that some models have close to zero change in cross-equatorial energy flux but nonzero ITCZ shifts in Figure 2.4a. First, the ITCZ is more closely connected to the “energy flux equator”, or the latitude at which the meridional transport of energy by the atmosphere is zero, than it is to the cross-equatorial energy flux. *Bischoff and Schneider* (2014) developed a theory for the relationship between cross-equatorial energy transport and the energy flux equator, assuming the latter was correlated with the ITCZ position, and argued that while the energy flux equator is proportional to the cross-equatorial energy flux, the constant of proportionality is governed by the net energy input into the tropical atmosphere, which can allow the energy flux equator to move while cross-equatorial energy transport does not change. We might expect this effect to occur when the atmosphere is suddenly thrown far out of energy balance, as happens when CO₂ is abruptly quadrupled. Furthermore, the ITCZ, when defined as the precipitation median or maximum, does not necessarily always follow the energy flux

equator, because the gross moist stability, or the efficiency with which the Hadley circulation exports energy, can change (*Seo et al.*, 2017).

Figure 2.4b shows the ITCZ shifts in G1 plotted against the warming of the northern hemisphere relative to the southern hemisphere. This is similar to Figure 7 of *Smyth et al.* (2017), but for the specific set of models analyzed here. In Figure 2.4b, there is a positive correlation ($r = 0.61$), slightly weaker than that for cross-equatorial MSE transport. While *Haywood et al.* (2013) found ITCZ shifts away from the cooled hemisphere in the extreme case of aerosol injections in only one hemisphere, the ITCZ shifts in Figure 2.4b imply that solar reductions applied equally in both hemispheres could still cause regional shifts in precipitation based on factors like the base state albedo and local radiative feedbacks that might warm one hemisphere relative to the other.

2.2 Attribution of changes using a moist energy balance model

In order to investigate the causes of robust changes in meridional energy transport in the G1 experiment and the largest sources of inter-model spread, I ran attribution experiments in which I perturbed different forcing and feedback terms one at a time.³ These experiments involved the moist energy balance model (EBM) first used by *Hwang and Frierson* (2010). I used the GCM output to calculate the magnitude of various forcings and feedbacks, including the greenhouse and solar forcings and cloud, surface albedo and non-cloud atmosphere feedbacks, and I used the EBM to understand how atmospheric energy transport would respond to each forcing or feedback in isolation. The advantage of using a moist EBM over directly integrating the energy fluxes associated with each forcing or feedback is that it allows for a coupled response between the energy transport, local temperature, and longwave radiative cooling.

The EBM takes as input the zonal mean surface and TOA energy fluxes and the LW cloud radiative effect from each GCM, and calculates the outgoing longwave radiation (OLR) as a

³In Chapter 3 I note that, for G1, the term “feedback” is not strictly accurate for describing the responses of TOA radiation to changes in properties like clouds because it implies a response to a global mean temperature change, which is absent in G1. I refer to “radiative adjustments” in that chapter instead. However, in this chapter I use the term “feedback” for both G1 and abrupt4xCO₂ for convenience.

function of surface temperature based on a linear fit of the clear-sky OLR and surface temperature output from each GCM. Eight GCMs are included in this section; the CSIRO-Mk3L-1-2 and GISS-E2-R models are excluded because the necessary outputs for calculating some of the feedback terms were not correctly archived. The net atmospheric energy flux input term is perturbed to account for the influence of various individual forcings and feedbacks, while the intercept of the clear-sky OLR-surface temperature relationship is re-fit in the perturbation climates (G1 and abrupt4xCO₂) to account for the enhanced greenhouse effect. Net vertical energy flux convergences at each latitude are balanced by meridional diffusion of MSE. I obtained a meridional energy transport estimate from the EBM by meridionally integrating this diffusion term. Several limitations of the EBM experiments must be noted. The approach of prescribing energy perturbations associated with feedbacks that are static in time does not take into account the interactions of different feedbacks with each other (analyzed by *Feldl et al.* (2017)) or changes in the feedbacks that arise from the changing energy transport (*Merlis*, 2014; *Rose et al.*, 2014; *Rose and Rayborn*, 2016). Also, changing the intercept of the OLR-temperature fit does not account for the nonuniformity of the CO₂ radiative forcing with latitude (*Huang and Zhang*, 2014).

The EBM was originally run in an effectively dry configuration, by accident due to a unit conversion error. Appendix A contains results from this configuration of the EBM and discusses implications for the role of moisture transport in atmospheric energy transport adjustments to local changes in the energy budget.

2.2.1 EBM description

Here I describe how the model works, with an emphasis on aspects of the model not described in detail in previous papers, and new changes made for the solar geoengineering experiments.

The core equation of the model, as in other energy balance models (e.g. *North*, 1975), is a heat diffusion equation:

$$\frac{\partial T_s}{\partial t} = C \left(EI - OLR + \frac{p_s}{g} D \nabla^2 MSE \right) \quad (2.5)$$

or

$$\frac{\partial T_s}{\partial t} = C \left(EI - OLR + \frac{p_s}{g} \frac{D}{r^2} \frac{\partial}{\partial x} \left[(1 - x^2) \frac{\partial MSE}{\partial x} \right] \right), \quad (2.6)$$

where MSE is the moist static energy, T_s is surface temperature, C is an arbitrary surface heat capacity, OLR is the outgoing longwave radiation at the top of the atmosphere, EI (“energy input”) is the net surface and TOA energy flux into the atmospheric column excluding OLR, D is a diffusivity coefficient for MSE, p_s is the surface pressure, g is the acceleration due to gravity, r is the radius of the earth, and $x = \sin(\theta)$ where θ is the latitude. I have explicitly written out the r^2 that comes from the Laplacian operator in Equation 2.6 rather than absorbing it into D as is often done (e.g. North, 1975). Noting that $dx = \cos(\theta)d\theta$, Equation 2.6 can also be written in terms of latitude, which is more convenient in terms of specifying inputs for EI as functions of latitude without converting to sine latitude first:

$$\frac{\partial T_s}{\partial t} = C \left(EI - OLR + \frac{p_s}{g} \frac{D}{r^2 \cos(\theta)} \frac{\partial}{\partial \theta} \left[\cos(\theta) \frac{\partial MSE}{\partial \theta} \right] \right). \quad (2.7)$$

A value of $1.06 \times 10^6 \text{ m}^2 \text{ s}^{-1}$ for D , following *Hwang and Frierson* (2010), and a flat topography is assumed with $g = 9.8 \text{ m s}^{-2}$ and $p_s = 980 \text{ hPa}$. The model steps forward with a relative time step of $\frac{dt}{C} = 1 \times 10^{-4}$. The model is considered to have converged when T_s differs by less than .001 K everywhere in the domain between successive time steps.

The moist static energy is calculated according to:

$$MSE = C_p T_s + L_v q \quad (2.8)$$

where C_p is the heat capacity of air at constant pressure, L_v is the latent heat of vaporization of water, and q is the specific humidity. I calculate q as a function of T_s using Equation 2.4, assuming a relative humidity of 80%.

The OLR is treated as a linear function of temperature:

$$OLR = aT_s - b \quad (2.9)$$

where the coefficients a and b are calculated as linear least-squares fits from the monthly surface air temperature and clear-sky OLR output in each of the GCMs over the first 40 years of

Table 2.2: Values of fit coefficients for clear-sky OLR as a function of temperature for use in moist EBM analysis.

Model	a ($\text{W m}^{-2} \text{K}^{-1}$)	b (W m^{-2})	b' (G1)	b' (abrupt4xCO2)
CanESM-2	2.0667	326.83	334.99	335.00
CCSM4	2.1604	350.06	358.31	360.35
CESM-CAM5.1-FV	2.0724	328.98	337.74	341.62
HadGEM2-ES	2.1531	349.37	357.38	358.99
IPSL-CM5A-LR	2.2149	363.39	370.58	370.46
MIROC-ESM	2.0512	327.40	336.37	336.18
MPI-ESM-LR	2.0157	315.55	324.47	324.34
NorESM1	2.1403	346.36	354.38	354.68

piControl.⁴ To consider the enhanced greenhouse effect in “perturbation” climates (G1 and abrupt4xCO2), I fit new coefficients b' , maintaining the original value of a (following *Hwang and Frierson*, 2010), based on the surface temperature and clear-sky OLR output in those experiments. To illustrate this process, scatter plots showing the fit of a and b for each model are shown in Figure 2.5. Table 2.2 shows the values of a , b , and b' calculated for each of the GCMs.

To run the EBM, I input the a and b coefficients shown in Table 2.2, and an EI term calculated differently for the different attribution experiments. For the EBM runs representing piControl conditions, the EI term is calculated using the following terms from the zonal mean output of each GCM:

$$\text{EI}_{\text{piControl}} = S - L_C + F_s \quad (2.10)$$

where S is the net downward SW radiation at the TOA, L_C is the LW cloud radiative effect (clear-

⁴For the CESM-CAM5.1-FV and NorESM-1 models, the linear fit was poorly conditioned, likely due to a nearly singular matrix from similar points being grouped together. To work around this, I took a random sample of 10^6 monthly means (about 1/6 of the total), and did the fit for that subset. I redid this several times to confirm that the fit coefficients did not significantly change with varying subsets.

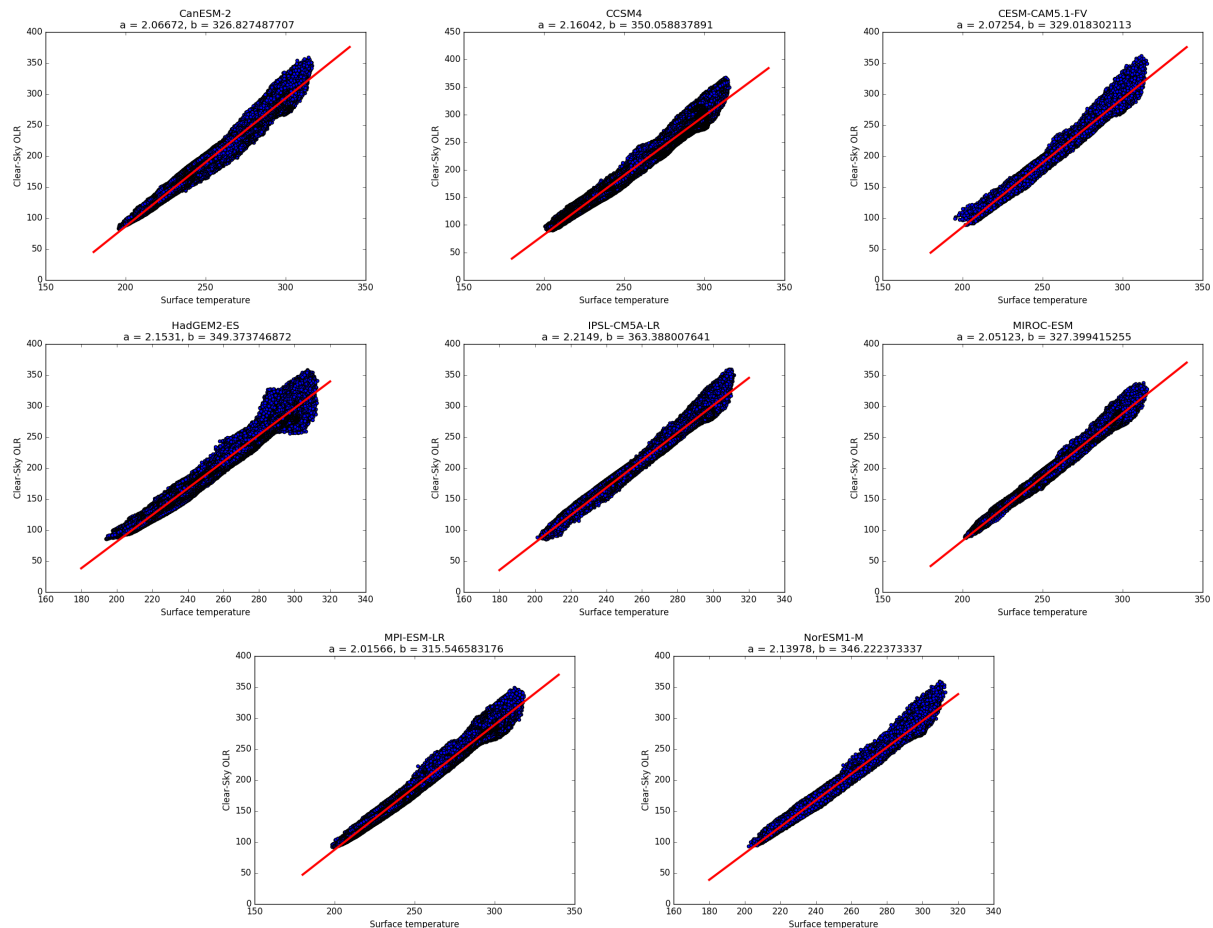


Figure 2.5: Scatter plots of surface air temperature vs. clear-sky outgoing longwave radiation in piControl (monthly means, years 1-40) for each of the 8 models included in the EBM analysis. Shown is linear fit line used to fit the coefficients a and b .

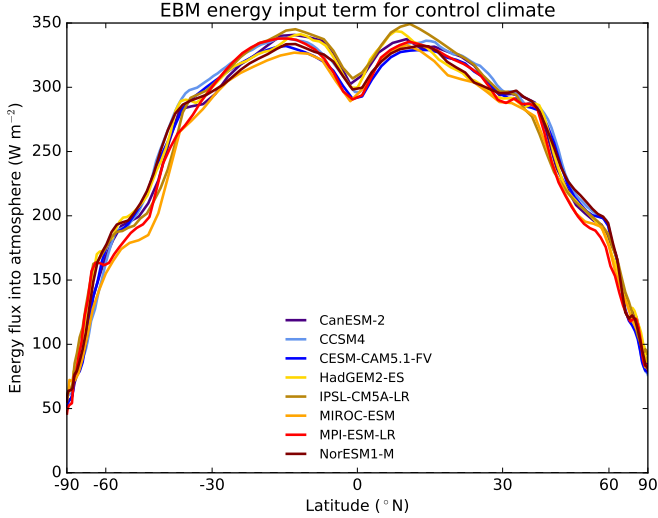


Figure 2.6: Energy flux into atmosphere input into moist EBM, calculated from the GCM piControl output (years 1-40) using Equation 2.10.

sky OLR minus all-sky OLR), and F_s is the net upward surface flux, including SW and LW radiation, sensible heat flux and latent heat flux. Figure 2.6 shows the EBM EI term derived from each GCM for the piControl experiment.

To obtain an estimate of the northward energy transport from the EBM output, I take the cumulative meridional integration of the MSE diffusion term in Eq. (2.6) after the EBM is run to equilibrium. The discretization of the diffusion equation for numerical solving inevitably results in some loss of energy, so after integrating, I apply a correction for residual northward transport at the North Pole for the EBM results, using Equation 2.3.

2.2.2 Comparison of EBM and GCM-derived energy transport

In order to be helpful in understanding the causes of the GCM behaviors, the EBM needs to predict changes in GCM-derived energy fluxes reasonably well when all forcing and feedback terms are considered. Figure 2.7 shows the meridional MSE transport across specific latitudes calculated by the EBM versus the same quantities diagnosed directly from the output of each

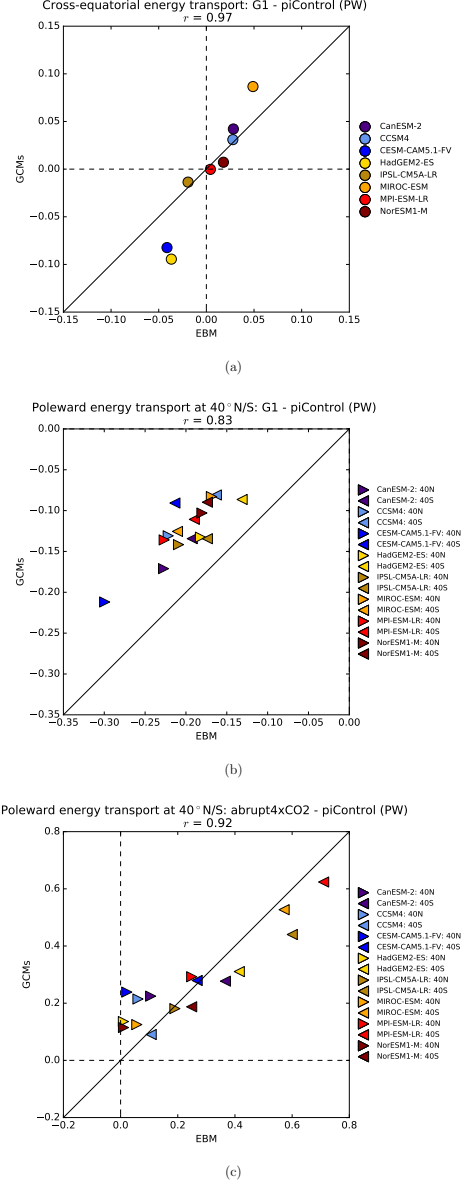


Figure 2.7: Meridional energy transport changes calculated by moist EBM (x -axis) versus those diagnosed from the GCM output (y -axis). (a): northward energy transport across the equator, for G1 minus piControl; (b): poleward energy transport changes across 40° N and S, for G1 minus piControl; (c): as in (b) but for abrupt $4\times\text{CO}_2$ minus piControl.

Table 2.3: Summary of attribution experiments run with moist energy balance model.

Name	Effects considered	OLR fit from
APRPcloud	SW radiative response at TOA due to cloud changes	piControl
APRPnoncloud	SW radiative response at TOA due to non-cloud atmosphere changes	piControl
APRPsurface	SW radiative response at TOA due to surface albedo changes	piControl
solarForcing	solar constant change (for G1), or nonlinear SW feedbacks (for abrupt4xCO ₂)	piControl
surfaceFlux	net SW, LW, sensible and latent heat flux changes at surface; <i>i.e.</i> surface energy storage	piControl
LWCRE	difference in net TOA LW radiation between clear-sky and all-sky conditions	piControl
greenhouse	enhanced greenhouse effect	G1 or abrupt4xCO ₂
all_G1	sum of effects listed in first 7 rows	G1
all_4xCO ₂	sum of effects listed in first 7 rows	abrupt4xCO ₂

The “OLR fit” refers to the fitting of coefficients for a linearized greenhouse effect based on surface air temperature and clear-sky OLR output from the GCMs; shown in the table is the GCM experiment from which these fits were drawn. Table 2.2 shows the actual fit coefficients.

GCM, for cross-equatorial transport in G1 minus piControl (Figure 2.7a), for poleward transport across 40°N/S in G1 minus piControl (Figure 2.7b), and for the same comparison in abrupt4xCO₂ minus piControl (Figure 2.7c). There are generally strong correlations in each of these cases. Cross-equatorial energy transport changes in abrupt4xCO₂ minus piControl are not examined because these did not correlate well with ITCZ shifts. Note that, for G1 minus piControl, the cross-equatorial energy transport appears to change more easily in the GCMs than in the EBM, while the poleward energy transport across 40° N/S changes more in the EBM than in the GCMs. Also, for abrupt4xCO₂ - piControl, the EBM tends to underestimate poleward energy transport changes in the Northern Hemisphere and overestimate them in the Southern Hemisphere. With these cautions in mind regarding the exact magnitude of the changes, the EBM predicts changes in GCM-derived energy fluxes well enough to proceed to the attribution experiments.

2.2.3 EBM attribution experiments

The attribution experiments are summarized in Table 2.3. Two experiments, “all_G1” and “all_4xCO₂”, consider all of the forcing and feedback terms for the two perturbation climates. There are three experiments that perturb shortwave feedbacks, based on the Approximate Par-

tial Radiation Perturbation (APRP) method (*Taylor et al.*, 2007). APRP uses a single-layer radiative transfer model to estimate the TOA radiative responses to changes in clouds, non-cloud atmospheric scattering and absorption, and surface albedo, based on monthly mean GCM cloud fraction output and SW radiative flux output at the surface and TOA.⁵ I refer to the SW feedback attribution experiments as the “APRPcloud”, “APRPnoncloud”, and “APRPsurface” experiments, which consider cloud, non-cloud atmosphere, and surface albedo feedbacks, respectively. The “solarForcing” experiment considers the change in insolation at the TOA due to the solar constant change. The “surfaceFlux” experiment considers the change in the net downward energy flux at the surface, which represents energy storage and transport by the ocean. The “LWCRC” experiment considers changes in the LW cloud radiative effect, or the difference between clear-sky and all-sky net TOA LW fluxes. Finally, the “greenhouse” experiment considers the enhanced clear-sky greenhouse effect, which includes the CO₂ forcing and the water vapor, Planck and lapse rate feedbacks.

The input terms for the EBM are calculated as follows. For the all_G1 and all_4xCO₂ cases, I use b' instead of b for the OLR calculation, and the EI term is:

$$\text{EI}_{\text{perturb}} = \text{EI}_{\text{piControl}} + C_S + A_s + I + \Delta L_C + O + \Delta S \quad (2.11)$$

where C_S , A_s and I are the change in the net downward TOA SW radiation associated with cloud, non-cloud atmosphere, and surface albedo feedbacks, respectively, calculated using APRP; ΔL_C is the change in the LW cloud radiative effect in the GCM output; O is the change in the net surface flux in the GCM output; and ΔS is the solar forcing. I calculate ΔS by taking the change in net TOA SW radiation between the control and perturbation climates, and subtracting C_S , A_s , and I to get the change in solar radiation that is not due to any of the three feedback terms. In G1 this represents the effect of changing the solar constant; in abrupt4xCO₂ this represents a residual feedback not accounted for by a linear sum of the other 3 feedbacks. For the individual

⁵To obtain these radiative responses in units of W m⁻², I multiply the change in the planetary albedo calculated using Equation 16 of *Taylor et al.* (2007) by the downward solar radiation at the TOA. Since the solar constant has changed in G1, I multiply by the “new” value of the insolation, so that the radiative responses calculated from APRP will not include a portion of the solar forcing itself.

attribution experiments (except “greenhouse”), I use b in the OLR calculation, and the EI terms are calculated as follows (experiment labels following Table 2.3):

$$\text{EI}_{\text{APRPcloud}} = \text{EI}_{\text{piControl}} + C_S \quad (2.12)$$

$$\text{EI}_{\text{APRPNoncloud}} = \text{EI}_{\text{piControl}} + A_s \quad (2.13)$$

$$\text{EI}_{\text{APRPsurface}} = \text{EI}_{\text{piControl}} + I \quad (2.14)$$

$$\text{EI}_{\text{solarForcing}} = \text{EI}_{\text{piControl}} + \Delta S \quad (2.15)$$

$$\text{EI}_{\text{surfaceFlux}} = \text{EI}_{\text{piControl}} + O \quad (2.16)$$

$$\text{EI}_{\text{LWC}} = \text{EI}_{\text{piControl}} + \Delta L_C \quad (2.17)$$

For the “greenhouse” experiment, I use the control value of EI, but use b' instead of b for the OLR calculation. Figures 2.8 and 2.9 show the various EI terms, minus that for piControl, for each model in each of the experiments (except the greenhouse experiment, which uses the pi-Control EI); these figures were not in the published version of this chapter but help illustrate the latitudinal distribution of the various perturbation terms.

2.2.4 Attribution of cross-equatorial energy transport changes

Figure 2.10 shows the changes in northward energy transport across the equator for G1 minus piControl in each of the experiments listed in Table 2.3. The “all_G1” results are the same as those plotted on the x -axis on Figure 2.7a and show that there is considerable inter-model spread in the value of the cross-equatorial energy transport changes. None of the experiments shown in Figure 2.10 moves cross-equatorial energy transport in the same direction in all 8 models (although the APRPcloud and greenhouse experiments come close), so we cannot say with much confidence that any one forcing or feedback is likely to push the ITCZ one way or the other under a solar geoengineering scenario. However, it is useful to examine the inter-model spread in each experiment in order to determine which terms cause the most uncertainty in the response of the ITCZ to solar geoengineering.

The two attribution experiments with the largest inter-model spread are the APRPcloud and

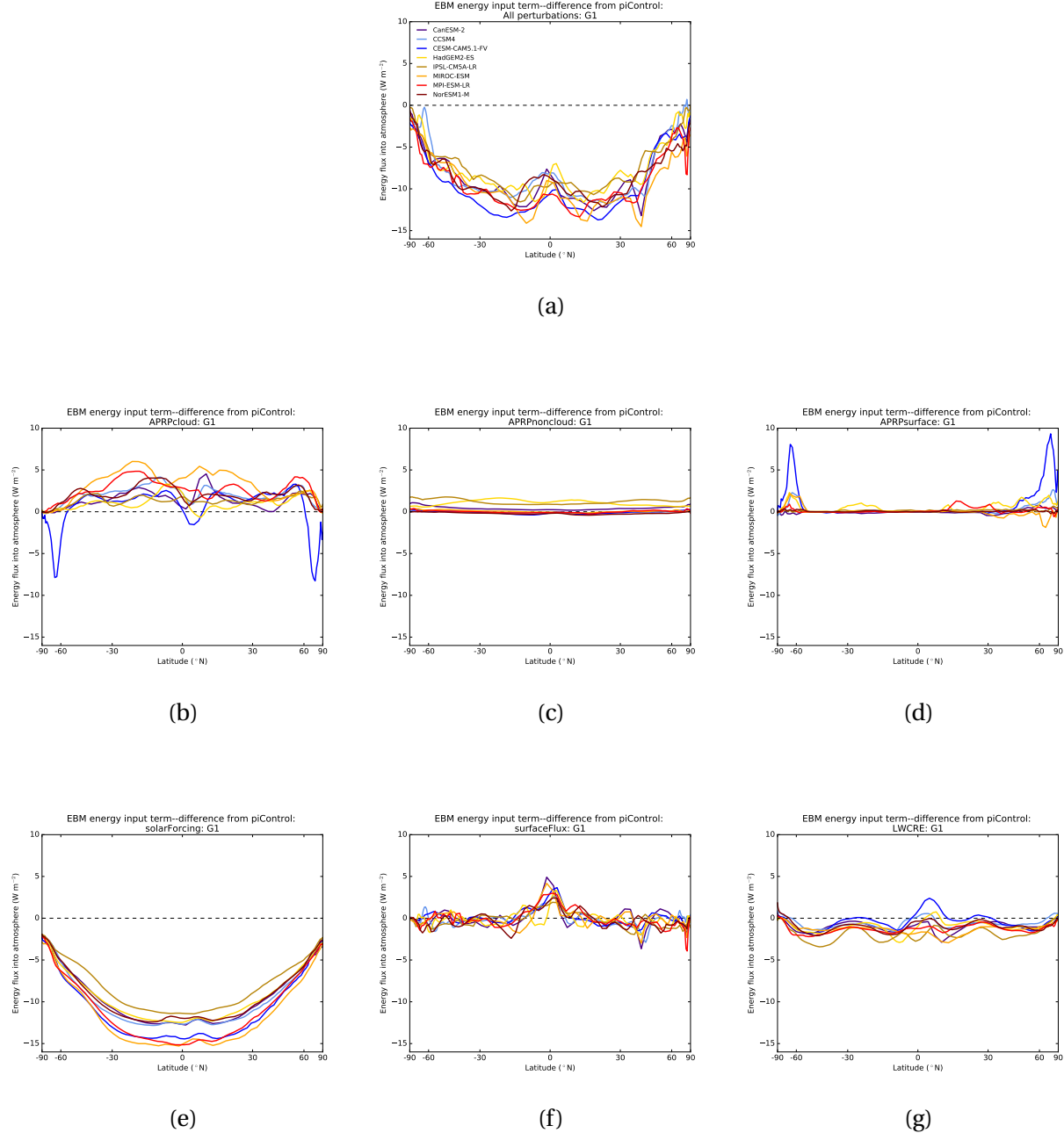


Figure 2.8: EBM energy input terms, minus the piControl EI, for the all_G1 experiment (a) and six attribution experiments in the G1 - piControl case (b-g), calculated using Equations 2.11 through 2.17. Experiment names following Table 2.3. Multi-model mean maps of the perturbations calculated using APRP (panels b-d) are shown in Figure 3.8.

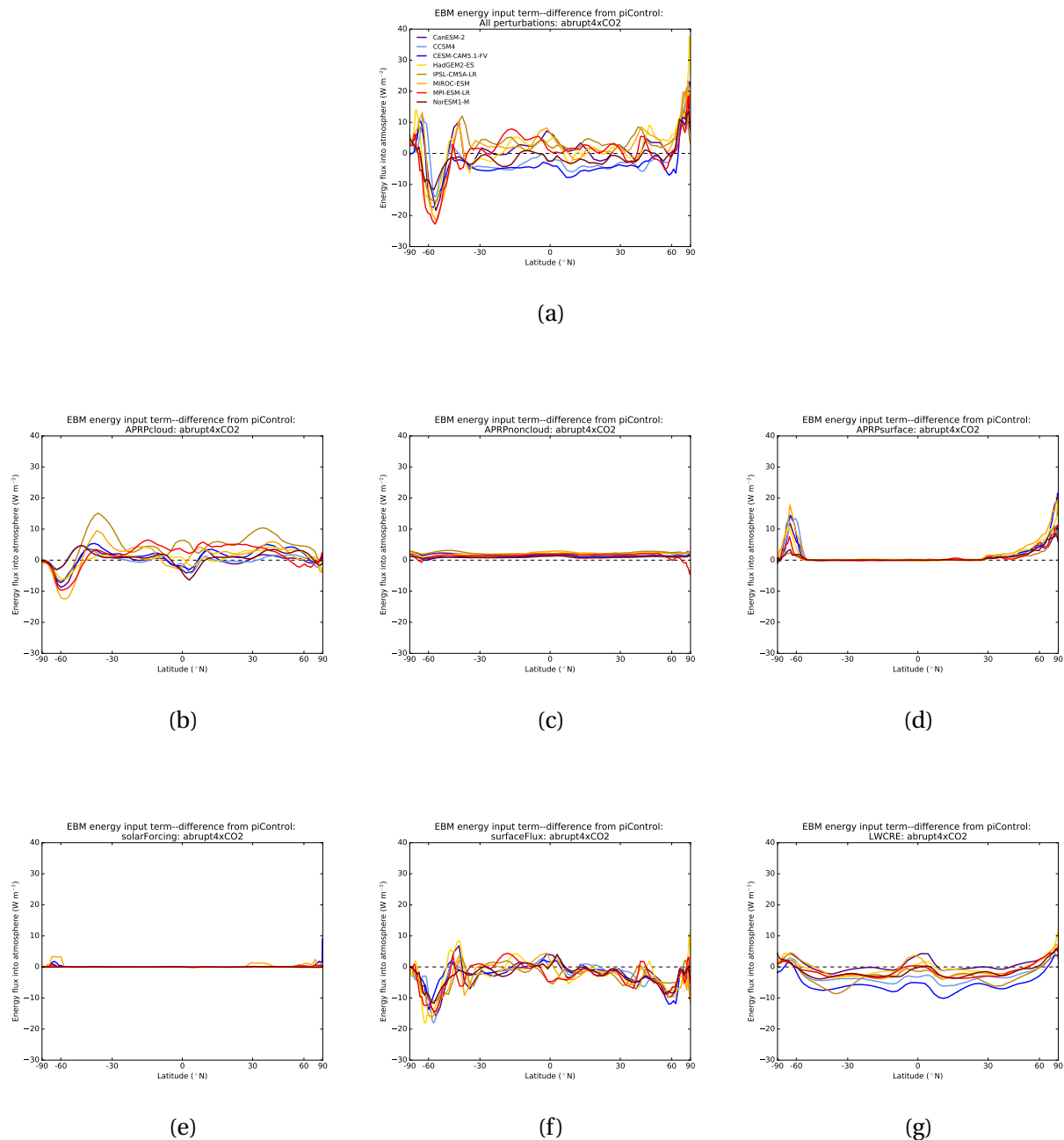


Figure 2.9: As in Figure 2.8 but for abrupt4xCO₂ minus piControl.

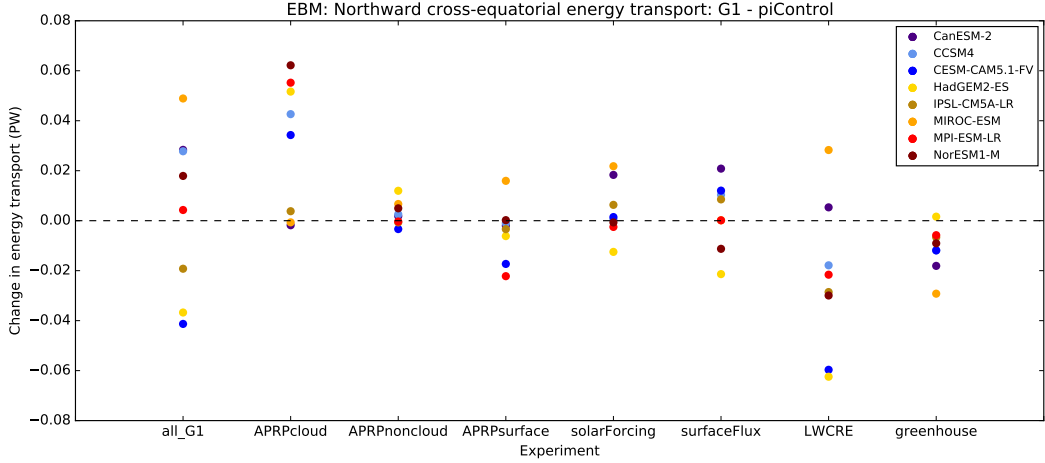


Figure 2.10: Changes in northward cross-equatorial energy transport calculated by moist EBM for G1 minus piControl in various attribution experiments.

LWCRE experiments, which correspond to SW and LW cloud feedbacks, respectively. This indicates that changes in clouds are the largest source of uncertainty regarding how cross-equatorial energy transport and, therefore, the ITCZ would respond to a hemispherically symmetric solar geoengineering scenario. This is similar to the finding of *Frierson and Hwang* (2012) that cloud feedbacks are the largest source of uncertainty for cross-equatorial energy transport changes in slab ocean simulations of CO₂-induced warming.

The APRPsurface, solarForcing, surfaceFlux, and greenhouse experiments have smaller inter-model spread than the two cloud experiments but are similar to each other. The spread in the surfaceFlux experiment indicates different responses of the atmosphere in different models to changes in either heat storage or cross-equatorial energy transport by the ocean. The appreciable inter-model spread in the solarForcing experiment suggests that the base state inter-hemispheric albedo difference is an important factor in the ITCZ response to solar geoengineering and solar forcings in general. This is interesting in the light of the result of *Haywood et al.* (2016) that tropical precipitation in the HadGEM2-ES is highly sensitive to the difference in the mean albedo between the hemispheres, and that equalizing them can improve GCM tropical

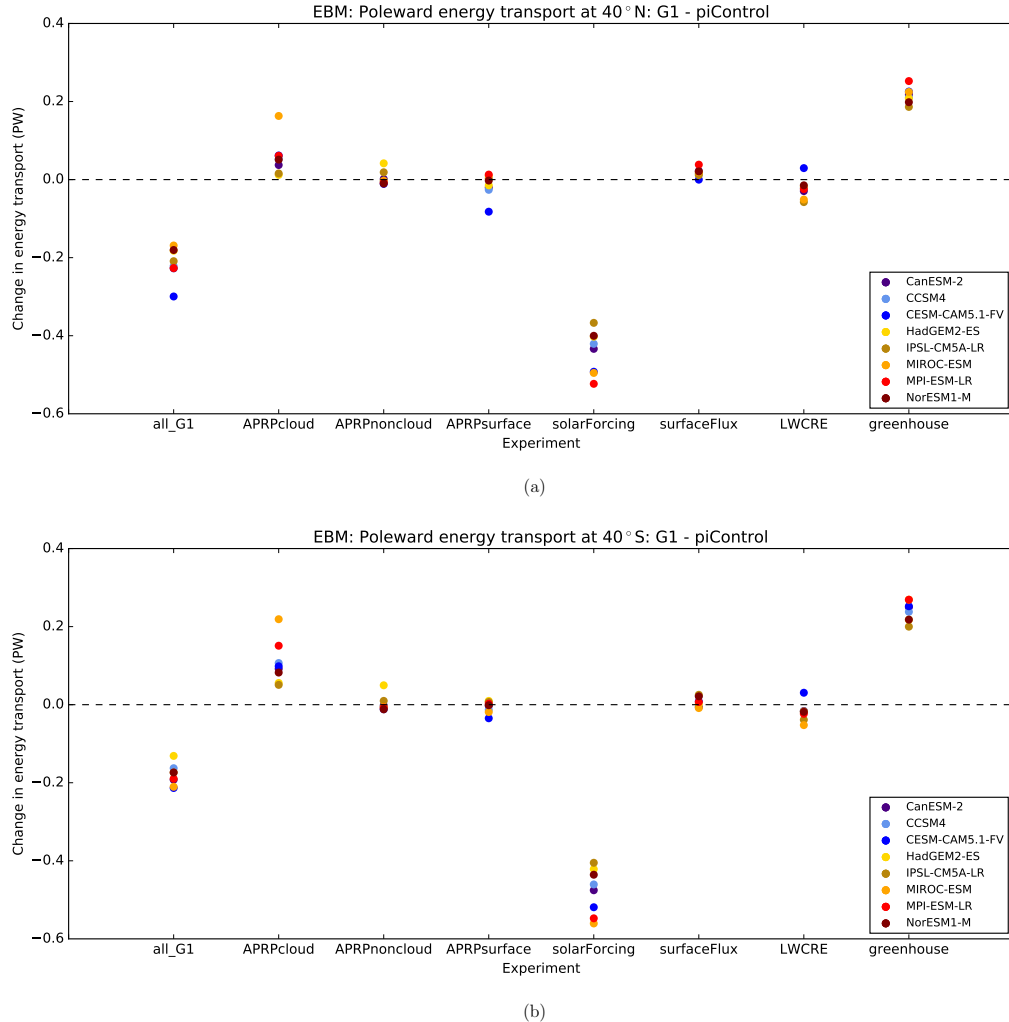


Figure 2.11: As in Figure 2.10 but for changes in poleward atmospheric energy transport across 40° N (a) and 40° S (b), for G1 minus piControl.

precipitation biases.

2.2.5 Attribution of poleward energy transport changes

Figure 2.11 shows the results of the same attribution experiments shown in Figure 2.10, but for poleward energy transport at 40° N (Figure 2.11a) and 40° S (Figure 2.11b). In the all_G1

experiment, poleward energy transport decreases at this latitude in both hemispheres. Poleward energy transport decreases in the solarForcing experiment for each model, and increases in the greenhouse experiment, but not by enough to compensate. The increase in poleward transport in the greenhouse experiment can be understood in terms of the increasing moisture transport argument discussed in Section 2.1 for the abrupt4xCO₂ experiment. The CO₂ radiative forcing in the EBM is spatially uniform since OLR, in the initial perturbation, is reduced by the same amount everywhere, but atmospheric moisture increases more in the tropics than at the poles because the atmosphere was warmer in the tropics to begin with. The reduction in tropical moisture in the solarForcing case is greater than the increase in the greenhouse case because there is more sunlight to reduce in the tropics, causing a greater temperature perturbation there for solar reductions than for greenhouse gas increases. One caveat to this point is that in the actual atmosphere the CO₂ radiative forcing is stronger in the tropics than at the poles (although by as much as the solar forcing), which contributes to stronger poleward energy transport (*Huang and Zhang, 2014*); this mechanism for increased energy transport under greenhouse gas forcings is not captured by the EBM.

The APRPcloud experiment exhibits an increase in poleward energy transport in both hemispheres in all models, which is consistent with a decrease in low cloud cover causing heating in the tropics. *Schmidt et al. (2012)* noted that low cloud cover decreased in four GCMs running G1. Chapter 3 contains a more detailed investigation of the cloud changes in the full G1 ensemble. None of the other feedback experiments have a consistent effect on poleward energy transport across 40° N/S, but the different feedback terms appear to rearrange the models in the all_G1 experiment, and contribute to the inter-model spread, with SW cloud feedbacks being the largest contributor. Models with a greater negative change in the solarForcing experiment (e.g. MPI-ESM-LR) also tend to have a greater positive change in the greenhouse experiment,⁶ and the compensation between these effects tends to reduce the inter-model spread. This implies that the remaining inter-model spread comes from the feedback terms. The fact that the

⁶The reason for this is that models with a greater CO₂ radiative forcing require a greater solar constant reduction to achieve energy balance in G1, as shown in Figure 3.1b.

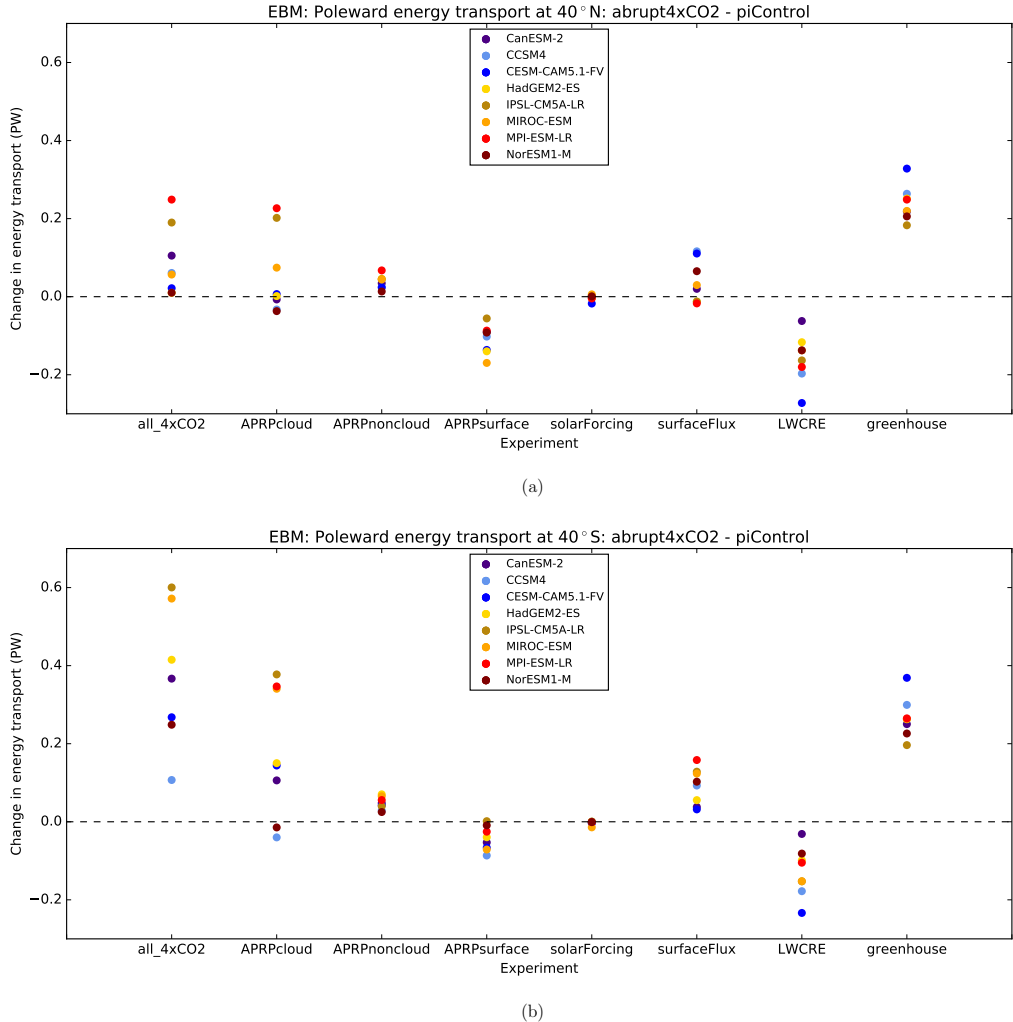


Figure 2.12: As in Figure 2.11 but for abrupt4xCO2 minus piControl.

solar forcing is the only term contributing to the reduction of poleward energy transport in G1 in all models implies that it is the imperfect compensation between SW and LW forcings, not local feedbacks, that causes this reduction.

Figure 2.12 is the equivalent of Figure 2.11, but for abrupt4xCO2 minus piControl. For abrupt4xCO2, the greenhouse attribution experiment results in an increase in poleward energy transport, similar to the same experiment for G1. SW cloud feedbacks (APRPcloud experiment)

are the largest contributor to the inter-model spread, followed by LW cloud feedbacks. Surface albedo feedbacks (APRPsurface) also contribute to the inter-model spread, but generally reduce poleward energy transport. (The increase in moisture due to tropical warming that results in greater poleward energy transport in the all_4xCO₂ experiment does not show up when only surface albedo is perturbed.) This feedback term is mainly due to ice melt at high latitudes, which would be expected to reduce the equator-to-pole temperature gradient and therefore also reduce poleward energy transport. The LWCRE experiment also reduces poleward energy transport for abrupt4xCO₂, because the LW cloud feedback is positive at high latitudes due to an increase in the optical depth of high clouds (*Zelinka et al.*, 2012a). As with G1, non-cloud atmosphere SW feedbacks have small effects on the poleward energy transport for abrupt4xCO₂, but there is a consistent increase in this case, presumably due to increases in SW absorption by water vapor. The solarForcing experiment in this case represents the residual between the total TOA net shortwave radiation changes and the individual feedback terms calculated using APRP; these effects are minor.

The surfaceFlux experiment has a much greater impact on poleward energy transport for abrupt4xCO₂ than for G1, or for the 20th and 21st century CMIP3 runs analyzed by *Hwang and Frierson* (2010). This is because, while the TOA was kept approximately in energy balance in G1, and the imbalance is relatively small in 20th and 21st century runs, the abrupt4xCO₂ case represents a response to an impulse that throws the climate system far out of equilibrium, with much energy being stored in the ocean over time. The energy loss from the atmosphere to the ocean is strongest in high latitudes, leading to a compensating increase in poleward atmospheric energy transport in the abrupt4xCO₂ surfaceFlux experiment.

2.3 Chapter conclusions

My analysis of the GeoMIP G1 ensemble shows that, when CO₂ concentrations are increased and the solar constant is reduced to compensate, poleward atmospheric energy transport decreases (Figures 2.1a,d). This is because of an increase in polar temperatures and decrease in tropical temperatures, or “residual polar amplification”, that results from the different spatial

patterns of the opposing solar and CO₂ forcings. The polar warming and tropical cooling cause a decrease in both dry static energy transport, which depends on the equator-to-pole temperature gradient, and latent heat transport, which depends on the meridional gradient of saturation vapor pressure. Residual polar amplification cannot be due to increases in poleward atmospheric energy transport, as might have been thought, because poleward energy transport actually decreases. It cannot be due to local feedbacks such as the ice-albedo feedback because these feedbacks cannot reverse the sign of an initial temperature change. Poleward energy transport by the ocean in the North Atlantic decreases (*Hong et al.*, 2017), and there is no reason to expect an increase in poleward energy transport by the ocean overall given the decrease in net energy flux into the ocean in the tropics. Instead, the spatial distribution of the combined CO₂ and solar forcing causes this pattern of temperature change, while the decrease in poleward energy transport then acts as a negative feedback that limits the polar warming in G1.

The reduction of poleward energy transport helps explain why the difference in temperature change in the poles and the tropics is not nearly as much in G1 as it is in abrupt4xCO₂, or in other words, why solar geoengineering in the form of a uniform solar constant reduction manages to eliminate most (but not all) of the polar amplification of CO₂-induced warming. The role of moisture transport is critical here. When CO₂ is increased by itself, poleward latent heat transport increases because of the large increase in moisture in the tropics, and this amplifies polar warming. In the G1 scenario, by contrast, the cooling of the tropics reduces the amount of moisture in the air, lessening the energy transport to the poles. This indicates that tropical moisture content is a very important control on the meridional temperature gradient. Geoengineering schemes have been designed that, in GCMs, avoid the problem of over-cooling the tropics by preferentially reducing sunlight in high latitudes (*Ban-Weiss and Caldeira*, 2010; *Kravitz et al.*, 2016). It would be useful to analyze the changes in atmospheric energy transport in these scenarios in order to better understand the role moisture transport would play in attempting to regulate temperatures at various latitudes.

The EBM attribution experiments illustrate the specific forcings and feedbacks responsi-

ble for the changes in meridional energy transport in G1. The solar forcing causes a reduction in poleward energy transport in mid-latitudes; the enhanced greenhouse effect only partially counteracts this. Cloud feedbacks are generally the largest contributors to the inter-model spread in both mid-latitude poleward energy transport changes and cross-equatorial energy transport changes, which are a predictor of ITCZ shifts. The large uncertainty in these quantities associated with clouds implies that an improved physical understanding of the changes in clouds in G1 would help our understanding of how regional precipitation and temperature changes would play out under a solar geoengineering scenario. Cloud changes in G1 are explored in detail in Chapter 3.

The finding that poleward atmospheric energy transport decreases in the G1 experiment relative to piControl is relevant for understanding why polar amplification of warming happens under increased CO₂. In warmer climates, the increased poleward energy transport contributes to the amount of polar amplification that occurs, as evidenced by model studies in which surface albedo is held constant (*Alexeev et al.*, 2005; *Graversen and Wang*, 2009). However, the analysis of G1 presented here shows that increases in poleward atmospheric energy transport are not necessary in order to have a decrease in the equator-to-pole temperature gradient. These results are particularly interesting in the light of the finding by *Hwang et al.* (2011) that polar amplification is negatively correlated with changes in atmospheric energy transport into the polar regions in CMIP3 global warming simulations. These results reinforce the conclusion of *Hwang et al.* (2011) that changes in energy transport alone cannot predict changes in the meridional temperature gradient, which is actually governed by the coupling between energy transport and local feedbacks. It is useful to remember as well that radiative forcings are not spatially uniform, and the structure of the CO₂ forcing can affect atmospheric circulations in warming simulations (e.g. *Huang and Zhang*, 2014; *Merlis*, 2015). The spatial structure of radiative forcing is part of the set of processes, including local feedbacks and energy transport by the atmosphere and ocean, that interactively determine the Earth's meridional temperature pattern. Due to the complexity of these interactions, changes in the temperature gradient cannot be quantitatively predicted without a general circulation model. To better understand these

interactions, it would be useful to do further analysis to quantify the contributions of different local feedbacks to the amount of polar warming in the G1 experiment.

Chapter 3

CHANGES IN CLOUDS AND ATMOSPHERIC PHYSICAL PROPERTIES AND IMPLICATIONS FOR REQUIRED SOLAR REDUCTION

An interesting question related to G1 is the amount of solar constant reduction $|\Delta S_0|$ required to compensate for the CO₂ increase, which has implications for the scale of the solar geoengineering intervention that would be required. This varies between about 3%-5% depending on the model (Table 1.2). (For convenience, I hereafter drop the absolute value symbol and use ΔS_0 to refer to the solar constant reduction, keeping in mind that the sign of the change is always negative in this context.) One might intuitively expect that ΔS_0 would be greater in models with greater equilibrium climate sensitivity (ECS), which is the amount of global mean temperature change that occurs after CO₂ is doubled and the climate adjusts to restore top of atmosphere energy balance. However, a scatter plot of ΔS_0 versus ECS for each model (Figure 3.1a) shows that there is actually no correlation (correlation coefficient $r = 0.02$) between these quantities. This makes sense if climate sensitivity is mainly determined by feedbacks on global mean temperature change, as has been found in CMIP5 models (*Vial et al.*, 2013), since the feedbacks will, at least to a first order, work just as well to reverse a warming effect when an equal and opposite radiative forcing is applied.

A more accurate prediction of the value of ΔS_0 in G1 is provided by a simple formula based on matching the reduction in outgoing LW radiation (OLR) from the CO₂ increase with a reduction in the absorbed SW radiation:

$$\Delta S_0 = 4 \times \frac{F_{4xCO2,eff}}{1 - \alpha} \quad (3.1)$$

or, in percentage terms,

$$\Delta S_0(\%) = \left(4 \times \frac{F_{4xCO2,eff}}{1 - \alpha} \right) \times \frac{100\%}{1361 \text{ W m}^{-2}} \quad (3.2)$$

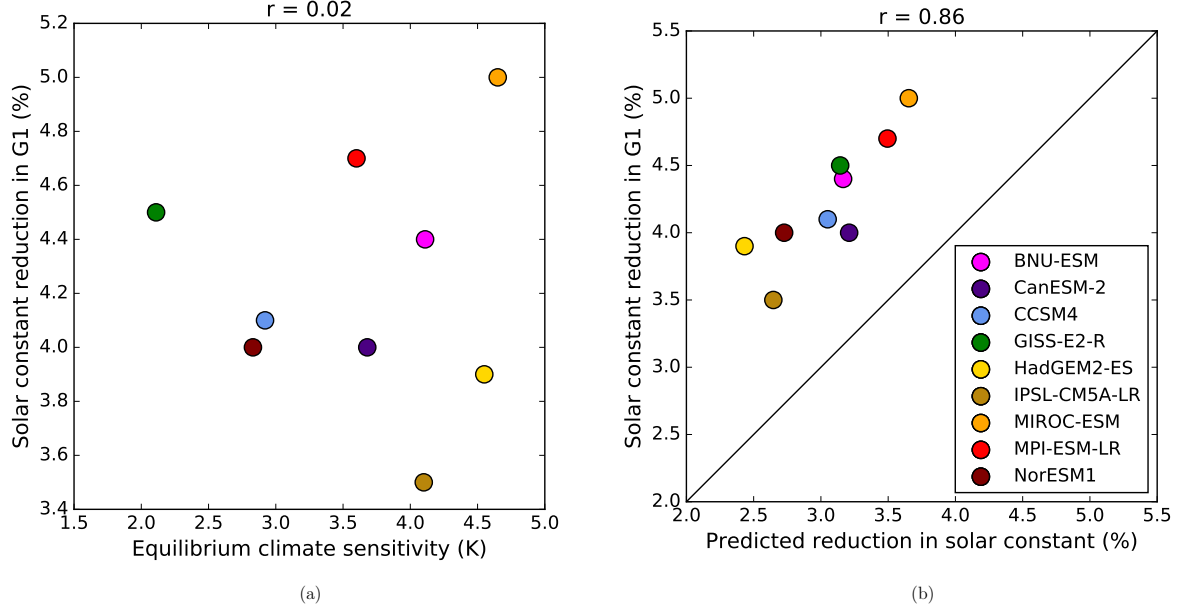


Figure 3.1: Percent solar constant reduction for models running the G1 experiment, versus (a) equilibrium climate sensitivity in the models, from *Sherwood et al. (2014)*, and (b) solar constant reduction predicted by Equation 3.2, based on effective radiative forcing values from *Sherwood et al. (2014)* and piControl planetary albedo values from *Kravitz et al. (2013a)*. CESM-CAM5.1-FV and CSIRO-Mk3L-1-2 are excluded from this figure because these models were not included in *Sherwood et al. (2014)*.

where $F_{4xCO_2,eff}$ is the effective radiative forcing from a CO₂ quadrupling and α is the planetary albedo, with $F_{4xCO_2,eff}$ and α both being model-dependent. This equation was used by the modeling groups to create an initial guess for ΔS_0 , later tuned using successive 10-year GCM runs to obtain net TOA radiation of less than 0.1 W m^{-2} . This achieved a global mean temperature within 0.3 K of that in the piControl experiment in all the models analyzed in this thesis (Table 1.2). The technical specifications for G1 (*Kravitz et al., 2011b*) actually say to use the “steady state net radiation (TOA) difference” between abrupt4xCO₂ and piControl as the radiative forcing in Equation 3.1, but this does not make sense because at steady state net TOA radiation is zero. *Schmidt et al. (2012)*, describing the process for G1, state that effective radiative forc-

ing, calculated by regressing net TOA radiative flux against global mean temperature change in abrupt4xCO₂ and taking the intercept (*Gregory et al.*, 2004; *Gregory and Webb*, 2008), was used for the initial guess in Equation 3.1. The effective radiative forcing incorporates rapid adjustments of the atmosphere's temperature and humidity profiles, cloud properties, and surface albedo to the CO₂ increase, but does not include temperature-dependent feedbacks. Strictly speaking, Equation 3.1 calculates the solar constant reduction that would balance the instantaneous CO₂ increase if atmospheric properties were allowed to adjust to the CO₂ increase but not to the solar constant reduction. Therefore, using it to predict ΔS_0 amounts to assuming that the solar forcing does not cause its own rapid adjustments.

Figure 3.1b compares the solar constant reduction predicted by Equation 3.1 to the reduction that actually achieved TOA energy balance under increased CO₂ after tuning. The correlation, $r = 0.86$, is much better than for ECS, and indicates that CO₂ forcing and planetary albedo determine ΔS_0 to a first order. However, for every model, the actual ΔS_0 is greater than the predicted value using Equation 3.1, as has been noted by *Schmidt et al.* (2012) for a subset of four models. This indicates that atmospheric and surface adjustments in response to the combined CO₂ and solar instantaneous forcings have a greater net warming effect on the climate than such adjustments to the CO₂ forcing alone, requiring a greater reduction in the solar constant to restore the global mean temperature to preindustrial.

To resolve this discrepancy, I propose using the *instantaneous* radiative forcing from the CO₂ increase, which is the change in OLR from the CO₂ increase when all atmospheric and surface properties are held constant, and explicitly accounting for the rapid adjustments to the *combined* CO₂ forcing and solar reduction, as expressed in the following equation:

$$\Delta S_0 = 4 \times \frac{F_{4xCO_2,inst} + \sum \Delta R_X}{1 - \alpha} \quad (3.3)$$

where $F_{4xCO_2,inst}$ is the instantaneous radiative forcing from the CO₂ quadrupling and ΔR_X represents the change in net downward TOA radiation associated with adjustments of various atmospheric and surface physical properties X to the combined forcings, following the notation of *Zhang and Huang* (2014). The various ΔR_X can be calculated using existing tools developed

for diagnosing radiative adjustments and feedbacks. Since there is no global mean temperature change in G1 by design (and approximately none in practice), it is appropriate to continue to refer to the changes in TOA radiative balance resulting from changes in various physical properties of the atmosphere and surface as “adjustments” and not “feedbacks” even though the time scale is no longer rapid after 50 years. *Kravitz et al.* (2013c) plotted time series of changes in the components of the surface energy budget in G1 (their Figure 1) and found that the fluxes change little after the first year, so the time scale of the adjustment is not important for our purposes. This is also demonstrated in plots showing the time series of the SW radiative responses to the G1 scenario in Appendix B.

This chapter examines changes in atmospheric temperature, specific humidity, cloud fraction, and surface albedo in G1, and quantifies the radiative effects of these changes in order to test the hypothesis that the solar constant reduction can be predicted using Equation 3.3 and understand why the required ΔS_0 is greater than that predicted using effective CO₂ forcing. I also explore the physical reasons for the changes in atmospheric properties, particularly cloud properties, which, as shown in Chapter 2, strongly affect meridional energy transport changes in G1, with implications for regional temperature and precipitation responses. The changes in the atmospheric profiles of temperature and humidity are plotted and discussed in Section 3.1. Changes in cloud fraction are shown in Section 3.2, and changes in variables that might help explain cloud fraction changes are discussed in Section 3.3. Section 3.4 quantifies the radiative effects of these surface and atmospheric adjustments to the G1 forcing. Section 3.5 examines the global means of these radiative adjustments to see which are most important and investigates how well Equation 3.3 predicts the required solar forcing in G1. Section 3.6 summarizes the results of this chapter.

3.1 Temperature and humidity profiles

To understand the physical basis for the radiative adjustments calculated in later sections, in this section I show changes in atmospheric temperature and specific humidity that occur in the G1 experiment relative to preindustrial conditions. As in the previous chapter, quantities are

averaged over 40 year time periods: years 11-50 of the G1 simulation, to avoid incorporating transient effects that occur in the first ten years into averages, and years 1-40 of the piControl simulation, except where otherwise noted.

Figure 3.2 shows the zonal mean temperature change for G1 minus piControl in each of the CMIP5 models listed in Table 1.2. Several features common to all models are apparent. At the surface, we can see the pattern of tropical cooling and polar warming explored in depth in Chapter 2. However, cooling dominates when considering the atmosphere as a whole. The tropical mid-to-upper troposphere cools more than the surface does, because the tropical temperature profile tends to follow a moist adiabat (e.g. *Wetherald and Manabe*, 1975), so that slight cooling at the surface leads to greater cooling aloft. The cooling of the tropical upper troposphere mirrors the effect that happens under global warming, where the upper troposphere warms more than the surface and emits more LW radiation, leading to a negative climate feedback known as the lapse rate feedback. In the case of G1, reduced LW emission from the atmospheric cooling has a warming effect on the planet; I quantify this effect using radiative kernels in Section 3.4.2.

Most models have an area of reduced cooling or even warming in the tropics near 100 hPa. This corresponds to the location of the tropical tropopause layer (TTL), an area in the tropics between about 70 and 150 hPa with properties of both the troposphere and stratosphere (*Fueglistaler et al.*, 2009). The detailed vertical structure of temperature changes here may have to do with complex interactions between local temperature, humidity, and cloud properties. Another notable feature of the temperature change is the cooling of the stratosphere. An increase in carbon dioxide concentration cools the stratosphere, due to increased emission of LW radiation to space (*Manabe and Wetherald*, 1975), and a decrease in the solar constant also cools the stratosphere because it reduces the amount of ultraviolet radiation absorbed by ozone. The stratospheric cooling effect from the solar constant reduction is about an order of magnitude smaller than that from the CO₂ quadrupling (*Govindasamy et al.*, 2003).

Figure 3.3 shows the change in the log of specific humidity between G1 and piControl in each model. I use a log scale because it makes it easier to visualize changes in specific humidity

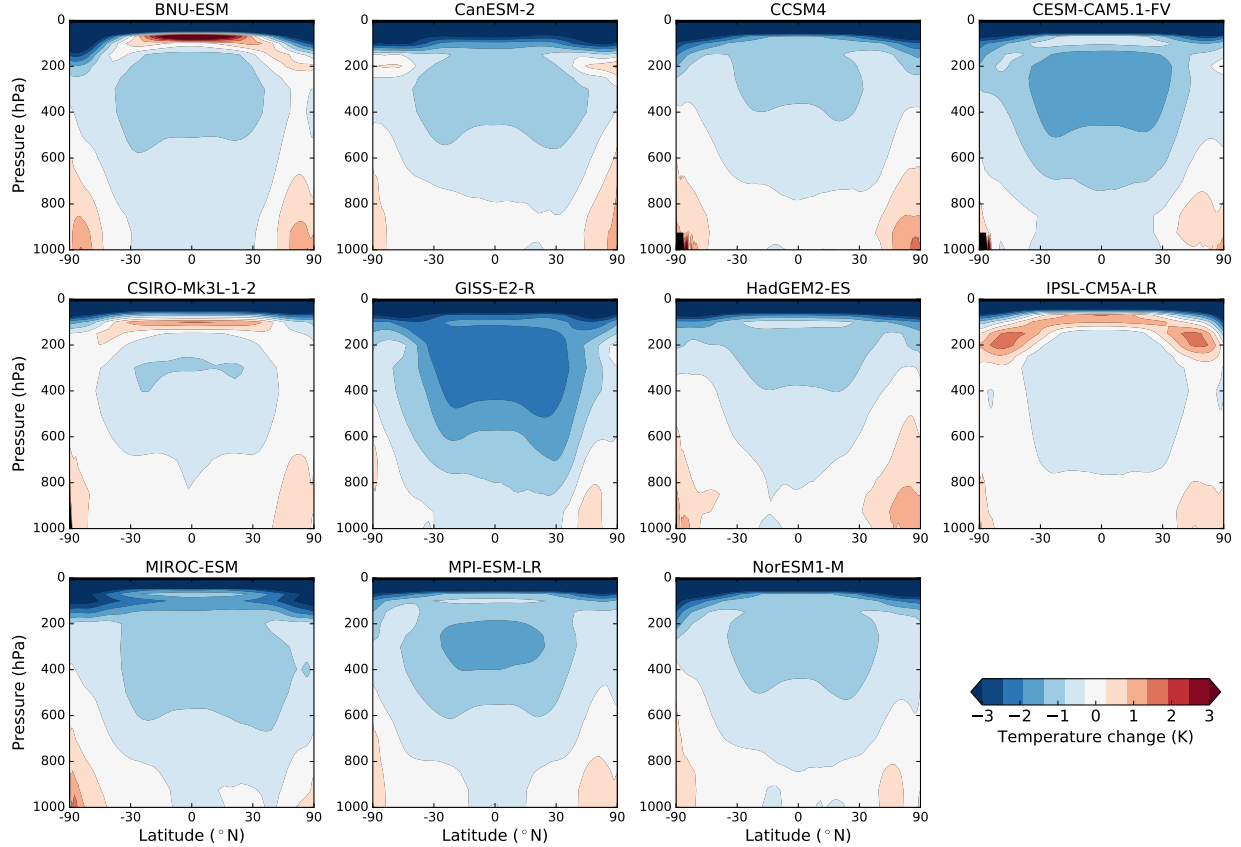


Figure 3.2: Zonal mean temperature change for G1 minus piControl in each model as a function of pressure.

that occur over multiple orders of magnitude, and because log humidity changes are used in the water vapor radiative kernel calculations described in Section 3.4.2. Most of the troposphere becomes drier in G1 in all models, consistent with the large-scale cooling absent significant changes in relative humidity. Since water vapor is a strong greenhouse gas, this drying has a cooling effect on the planet, which I quantify in Section 3.4.2. Most models show moistening in the polar regions at low altitudes, consistent with the warming there, although the moistening is typically confined to smaller areas than the warming, indicative of a slight decrease in relative humidity at the poles (*cf.* Figure 5 of *Smyth et al.*, 2017). Interestingly, stratospheric water vapor

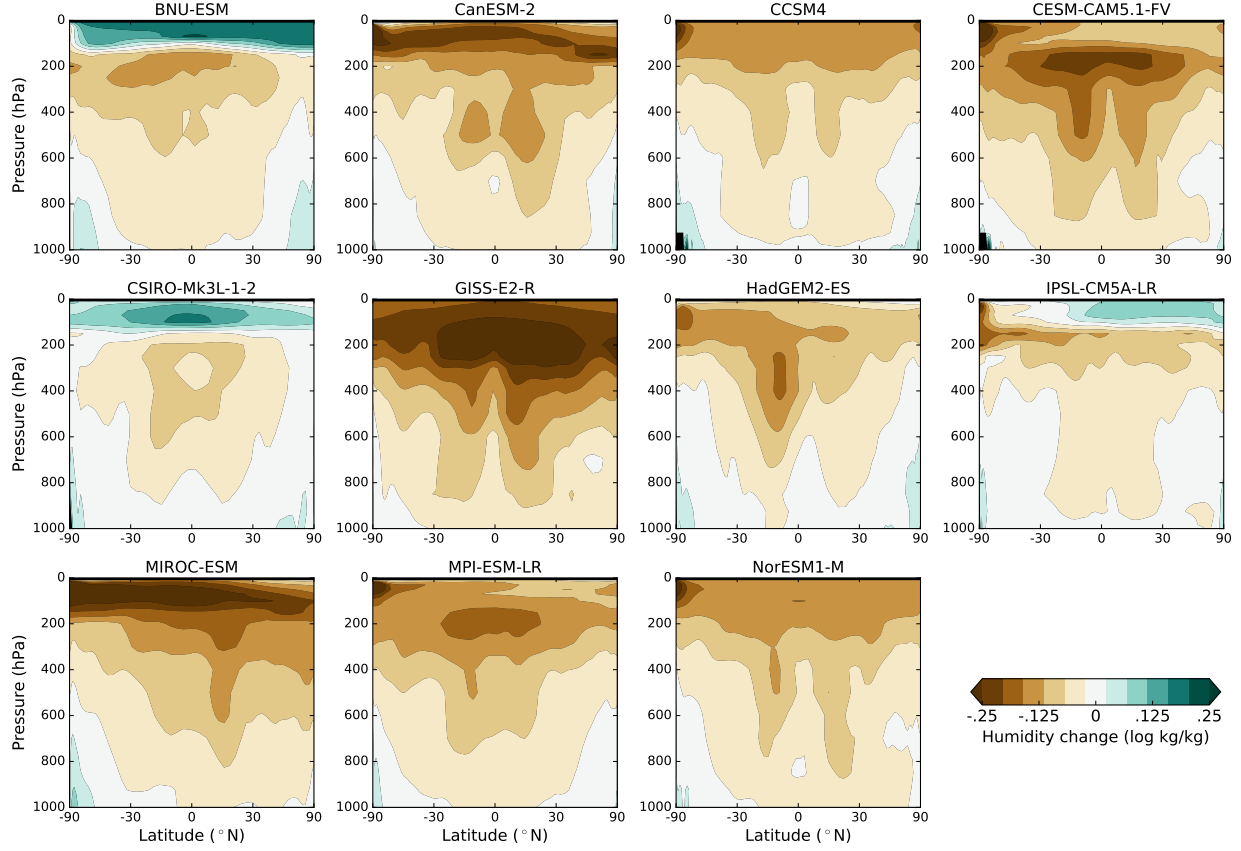


Figure 3.3: Zonal mean change in the natural log of specific humidity for G1 minus piControl in each model as a function of pressure.

decreases in most models, but it increases in the three models, BNU-ESM, CSIRO-Mk3L-1-2, and IPSL-CM5A-LR, that have warming in the TTL (albeit this moistening is mostly confined to the northern hemisphere in the IPSL model). This is consistent with stratospheric humidity being set by temperatures in the TTL, through which air travels to reach the stratosphere as part of the Brewer-Dobson Circulation (e.g. *Brewer, 1949; Newell and Gould-Stewart, 1981*).

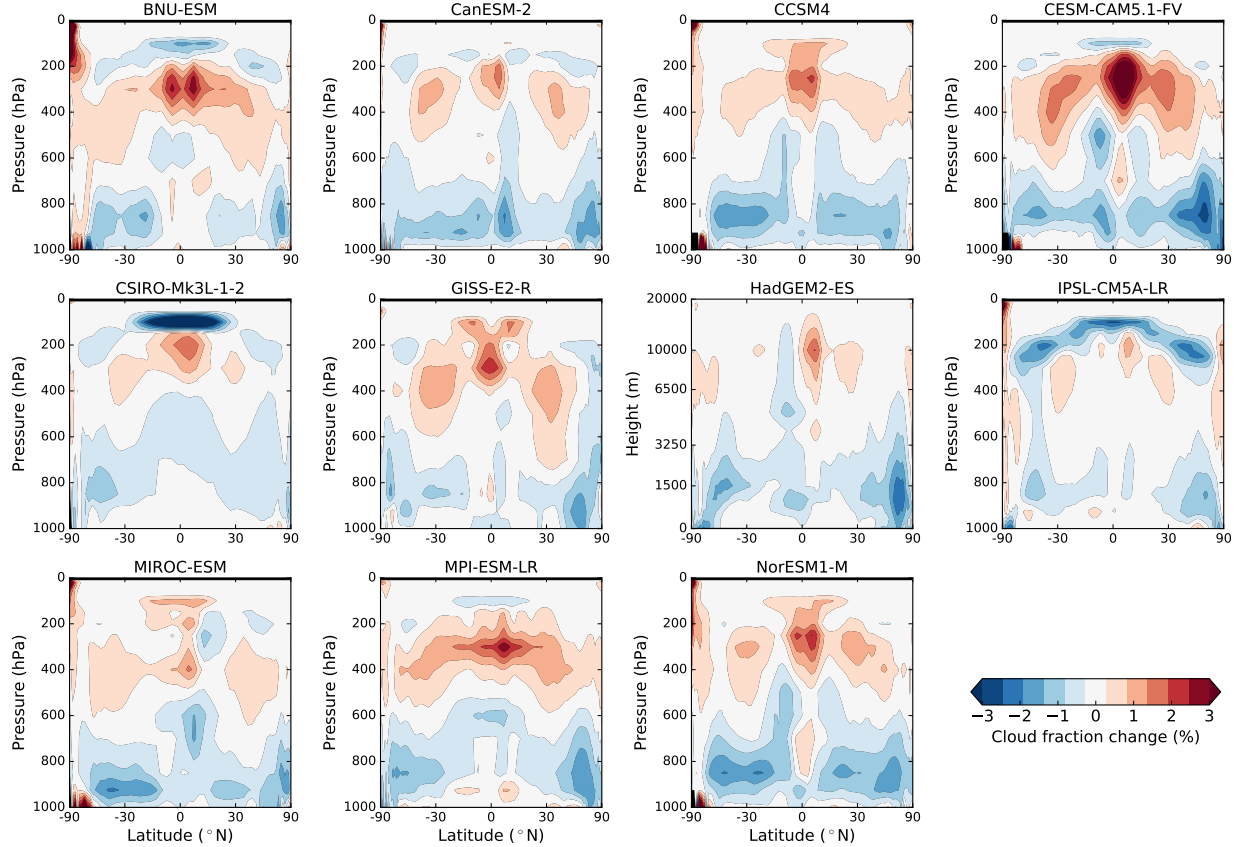


Figure 3.4: Zonal mean change in cloud fraction for G1 minus piControl in each model as a function of pressure, or height for HadGEM2-ES. To help comparisons with other models, the vertical axis for HadGEM2-ES is scaled according to $e^{-z/8000}$ m (where z is height), which is approximately proportional to pressure.

3.2 Cloud fraction profiles and maps

Figure 3.4 shows the zonal mean changes in cloud fraction in each of the models for G1 - piControl, and Figure 3.5 shows this quantity in the multi-model mean. Unlike atmospheric temperature and humidity, cloud fraction model output in CMIP5 and GeoMIP was archived on the native model vertical grid instead of a set of standardized pressure levels. Most of the GeoMIP models use hybrid sigma pressure coordinates, with the exceptions of GISS-E2-R, which

uses pressure coordinates, and HadGEM2-ES, which uses hybrid sigma height coordinates. To enable direct comparisons with the temperature and humidity changes and radiative kernel calculations, I have regridded the cloud fraction output to the standard CMIP5 pressure levels, or to a fixed height grid for HadGEM2-ES. Conversion from hybrid sigma to pressure or height coordinates was done using a Python function based on the algorithm used in the “convert_sigma_to_pres” Matlab function by *Vimont* (accessed 2018). Since surface pressure output (required for the hybrid sigma pressure regridding) was only available for the last 50 years of the piControl simulation for CSIRO-Mk3L-1-2, I have used the last 40 years of this simulation as the control case for cloud fraction for this model, instead of the first 40 years.

In their study of four models running G1, *Schmidt et al.* (2012) noted that all four had a reduction in low cloud fraction, while high clouds had an inconsistent change. Figure 3.4 shows that an overall reduction of low cloud fraction occurs in all 11 models analyzed here. For high clouds, I also find some inter-model inconsistencies, but overall high cloud fraction increases in most models, and there is a broad region of high cloud increase agreed upon by at least 8 models (Figure 3.5). Some models, especially those in which the TTL warms (Figure 3.2), have a decrease in high cloud fraction in the TTL, and two of them, CSIRO-Mk3L-1-2 and IPSL-CM5A-LR, have an overall decrease in high cloud fraction. Since low clouds primarily have a cooling effect on the climate due to their strong SW reflection, a reduction in low clouds would result in a warming effect that would partially counteract the cooling from solar geoengineering. An increase in high cloud fraction would also be expected to have a warming effect on the planet by reducing LW emission to space, although other variables, such as cloud height, are more important to the LW effect of cloud changes in global warming simulations (*Zelinka et al.*, 2012a). High clouds also interact with local temperature and humidity profiles in complex ways; for example, the reduced high cloud fraction in the IPSL model appears to warm the atmosphere immediately above, due to a reduction in LW emission from the cloud tops. I quantify the TOA SW and LW effects of the changes in cloud properties in Sections 3.4.1 and 3.4.2, respectively. In many models there is an increase in clouds in the stratosphere over Antarctica, likely due to the stratospheric cooling. Two models, HadGEM2-ES and MIROC-ESM, have a dipole in cloud

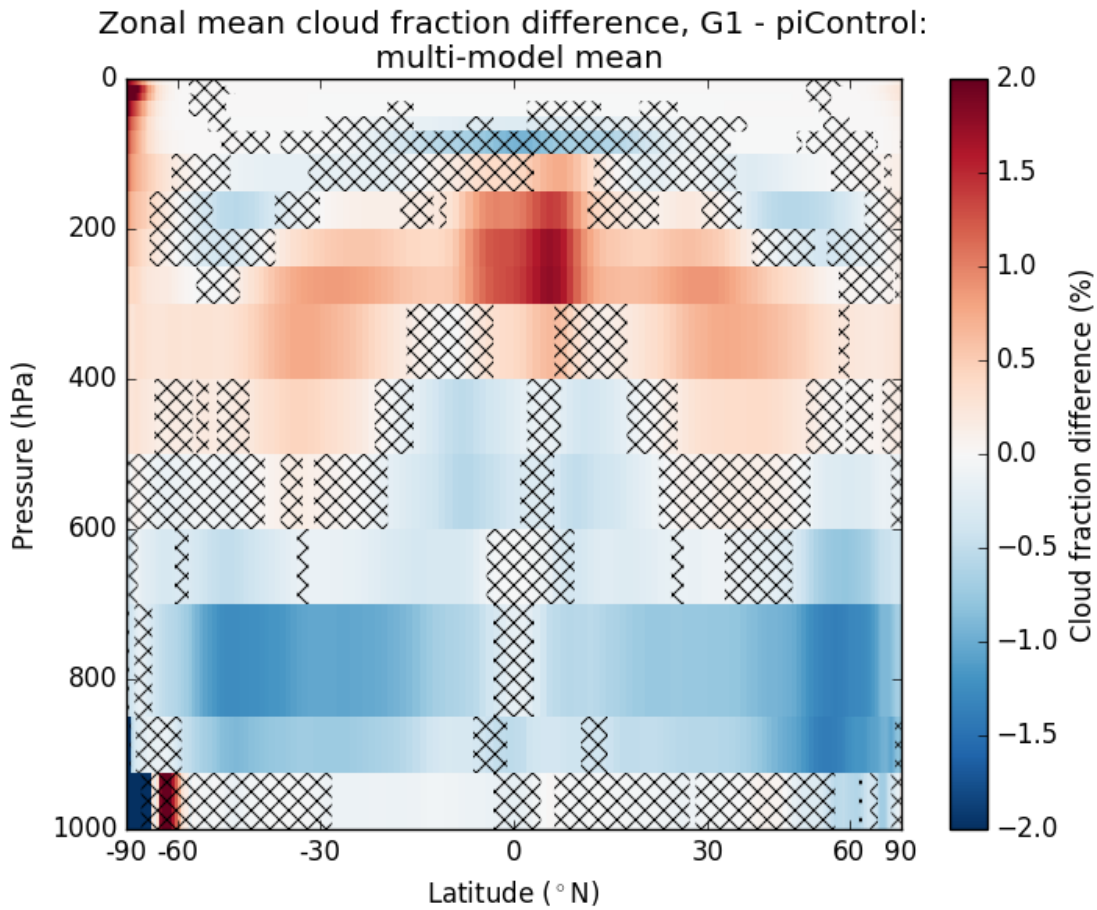


Figure 3.5: Multi-model mean, zonal mean change in cloud fraction for G1 minus piControl. HadGEM2-ES excluded because of different coordinate system. Hatching indicates areas where fewer than 8 of 10 models agree on sign of change. Plotted layers correspond to values archived at the pressure level at the bottom of each layer.

fraction changes in the upper troposphere, corresponding to northward and southward shifts, respectively, of the ITCZ in these models (Figure 2.4).

To get a sense of the zonally asymmetric spatial patterns of cloud fraction changes and to better understand areas of inter-model consensus and disagreement, Figure 3.6 shows maps of the multi-model mean changes in low, middle, and high cloud fraction for G1 - piControl.

Within the ranges for low, middle, and high clouds, I assume random overlap between adjacent layers of the common pressure grid. I use 680 hPa as the boundary between low and middle clouds and 440 hPa as the boundary between middle and high clouds, following the standards for the International Satellite Cloud Climatology Project (ISCCP; see Figure 2 of *Rossow and Schiffer*, 1999), or 3250 m and 6500 m in the case of HadGEM2-ES, which roughly correspond to these pressure levels in the 1976 U.S. Standard Atmosphere (NOAA, 1976). These plots, and all subsequent multi-model mean maps, show stippling where fewer than all but 2 of the included models agree on the sign of the change, so that unstippled areas indicate robust changes. Since this agreement could happen by chance in isolated areas, I focus on areas with apparent spatial structure or a physical reason why we might expect a change. For all multi-model mean maps, corresponding maps for each of the individual models are available in the Supplemental Information to the submitted paper. Global mean cloud fraction changes for the individual models are shown in Table 3.1.

The reduction in low cloud fraction (Figure 3.6a) is widespread, occurring over most ocean areas except for regions close to the equator and poles, and over most non-desert land areas. Middle clouds (Figure 3.6b) have fewer areas with robust changes, but there is a reduction in the cloud fraction on either side of the equator over the Atlantic and Pacific and over the equatorial Indian ocean. This may be related to a narrowing of the annual mean tropical precipitation maximum (see Fig. 5 of *Tilmes et al.*, 2013), which may be due in part to a reduction in the seasonal migration of the ITCZ (*Smyth et al.*, 2017). For high clouds (Figure 3.6c), there are few areas with robust changes, but there is a notable increase in high clouds over the equator, in some subtropical regions (around 30° N and S), and over the poles, particularly Antarctica. Figure 3.4 shows that the high cloud increases over the poles are mostly in the stratosphere.

3.3 Predictors of low cloud changes

Without additional experiments varying potential drivers of cloud changes, it is difficult to prove definitively the causes for the changes in cloud fraction. However, it is possible to gain some insight into the reasons for changes in low cloud fraction over the ocean by plotting sev-

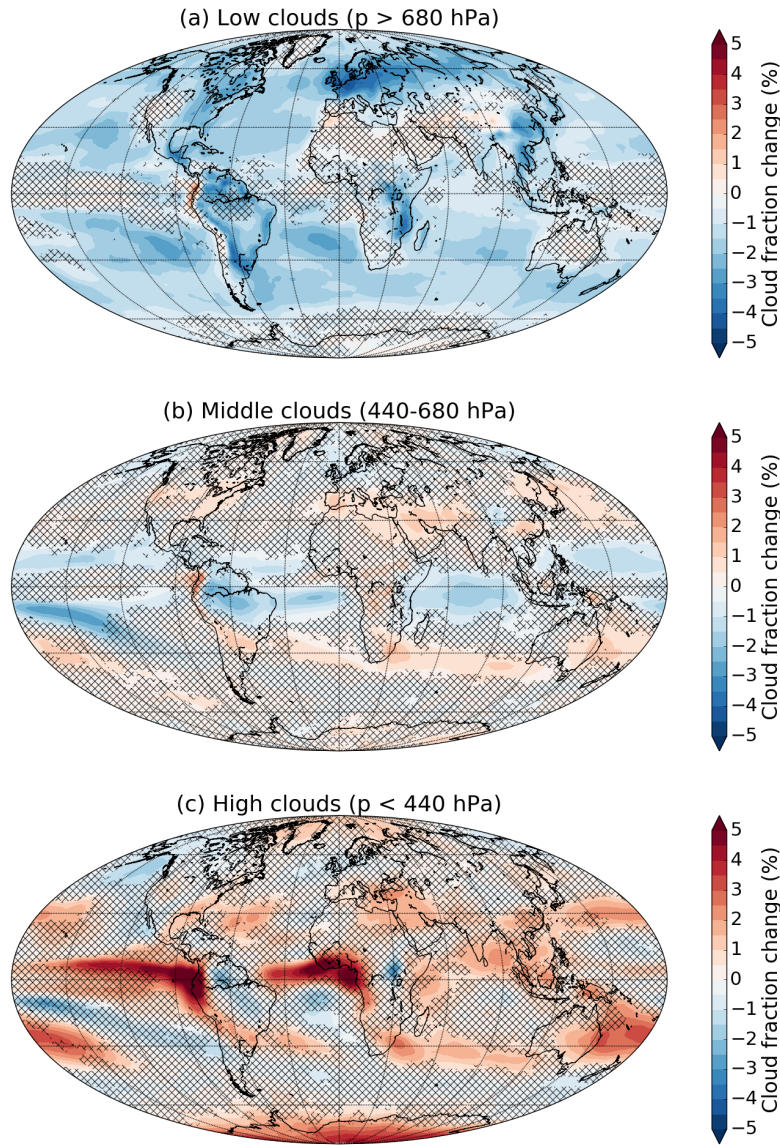


Figure 3.6: Multi-model mean changes in low (a), middle (b), and high (c) cloud fraction for G1 - pi-Control. Hatching indicates areas where fewer than 9 of the 11 models agree on the sign of the change.

eral variables that are correlated with low cloud fraction in observations. These include lower-tropospheric stability (LTS), defined as the difference in potential temperature between 700 hPa

Table 3.1: Global mean changes in low, middle and high cloud fraction in G1 minus piControl.

Model	Cloud fraction change (%)		
	low	middle	high
BNU-ESM	-0.60	0.26	0.91
CanESM-2	-1.59	-0.14	0.69
CCSM4	-1.54	-0.15	1.19
CESM-CAM5.1-FV	-1.51	0.03	1.38
CSIRO-Mk3L-1-2	-0.71	-0.51	-0.57
GISS-E2-R	-1.04	0.13	1.34
HadGEM2-ES	-1.38	-0.19	0.44
IPSL-CM5A-LR	-0.74	0.03	-1.12
MIROC-ESM	-1.60	-0.02	0.76
MPI-ESM-LR	-1.03	-0.05	1.31
NorESM1	-1.63	-0.22	1.12

and the surface (*Klein and Hartmann*, 1993), and estimated inversion strength (EIS), a metric of the temperature inversion at the top of the marine boundary layer. EIS is defined as (*Wood and Bretherton*, 2006, Eq. 4):

$$\text{EIS} = \text{LTS} - \Gamma_m^{850} (z_{700} - \text{LCL}) \quad (3.4)$$

where Γ_m^{850} is the moist adiabatic lapse rate at 850 hPa, z_{700} is the height of the 700 hPa surface, and LCL is the lifting condensation level. The calculations of LTS and EIS are described in more detail in Section 3.3.1.

Figure 3.7 shows the changes in EIS (a) and LTS (b) for G1 - piControl. Both of these quantities generally decrease across most of the ocean, except for some regions centered near 15° N and S. The reduction in EIS is generally smaller than the reduction in LTS (due to the correction for the moist adiabatic temperature profile), but is still widespread. A reduction of the strength

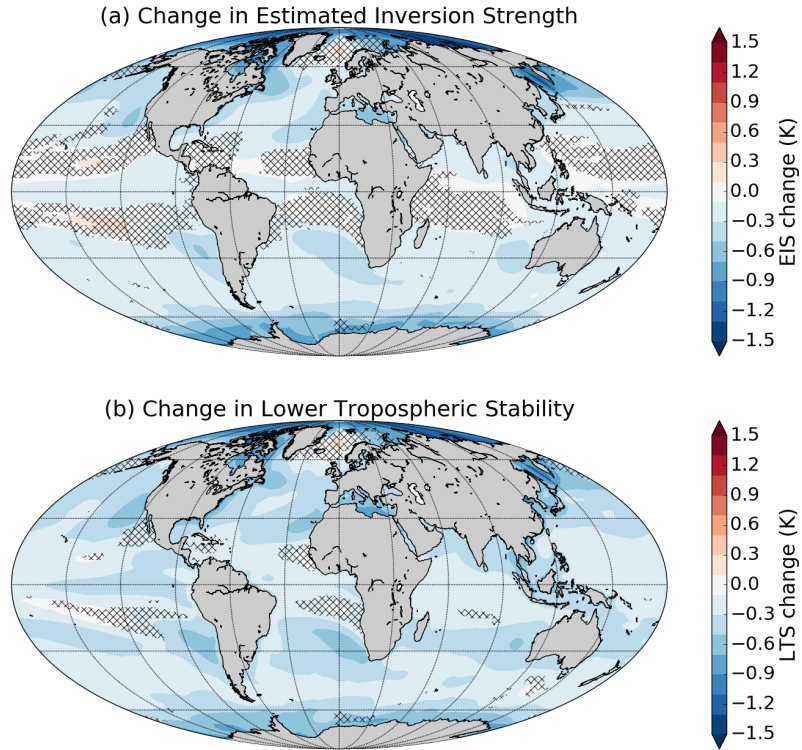


Figure 3.7: Multi-model mean changes in EIS (a) and LTS (b) for G1 - piControl. Hatching indicates areas where fewer than 7 of 9 models agree on the sign of the change. CSIRO-Mk3L-1-2 and MPI-ESM-LR models are excluded from this plot because near-surface specific humidity output, which is required to calculate EIS, was not available.

of the inversion at the top of the boundary layer would be expected to reduce low cloud fraction by encouraging mixing of dry air into the boundary layer, so the reduction in EIS over the ocean is a likely explanation for the reduction in low cloud fraction there. Stability metrics are included in low cloud fraction schemes in many models, and those that use the *Slingo* (1987) scheme, such as CCSM4 and NorESM1-M, have an explicit dependence of low cloud fraction on a stability metric very similar to LTS.¹ However, the robustness of the reduction in low cloud

¹This explicit dependence, involving the lapse rate below 750 hPa, is listed in Equation 8 of the Slingo paper.

fraction in G1 indicates that it is not the result of the idiosyncrasies of any one cloud fraction scheme.

Besides changes in stability metrics, other factors that have been suggested as explaining changes in marine stratocumulus cloud fraction under global warming conditions in large-eddy simulation models include reduced LW radiative cooling from cloud tops due to increased CO₂ and H₂O concentrations; decreased subsidence above the boundary layer; and increased sea surface temperatures (*Bretherton*, 2015). *Qu et al.* (2014) analyzed changes in marine stratiform cloud fraction in CMIP3 and CMIP5 global warming experiments, and found a reduced low cloud fraction in most models, which they attributed to an increase in sea surface temperature (SST). While EIS increased, which would promote increased cloud fraction, this was not enough to compensate for the SST increase in the global warming scenarios. In G1, SST changes little (and in fact decreases slightly in the tropics and subtropics (*Hong et al.*, 2017, Fig. 1)), leaving EIS to dominate changes in low cloud fraction over the ocean. It does not appear that cloud top radiation or subsidence could be responsible for the widespread low cloud reduction. The mechanism of reduced radiative cooling from cloud tops would be much weaker for G1 than for global warming if at all present because, while CO₂ concentrations have increased, water vapor concentrations have decreased. I have not tried to quantify how these fluxes have changed in G1 since LW radiative fluxes at the top of the boundary layer were not included in the Ge-oMIP model output archive. Meridional stream function anomaly plots for G1 minus piControl (*Smyth et al.*, 2017; *Guo et al.*, 2018) show that while some areas have anomalous subsidence, others have anomalous rising motion, and these regions are not consistent between models.

Qu et al. (2014) attribute the increase in EIS in global warming experiments to greater surface warming over the continents and the tropical western Pacific warm pool relative to the rest of the ocean; the warmed air is then advected over the tops of the marine stratocumulus fields. However, a reverse version of this mechanism does not seem to be at work in G1 because cooling is more robust over the ocean than over land (*Kravitz et al.*, 2013a, Figure 2). It is also important to keep in mind that there are different metrics of stability that are useful for different parts of the atmosphere and for different types of clouds. *Kravitz et al.* (2013c) argued that any

cloud cover changes in G1 would be due in part to increases in atmospheric stability, but here it appears to be a decrease in stability that is most relevant to the low cloud reduction. Another metric of stability, the rate of increase of equivalent potential temperature with height, does in fact increase in G1 relative to piControl, as shown in Figure 8 of *Kravitz et al.* (2013a). So, even as the atmosphere has gotten less stable in G1 with respect to boundary layer turbulence, it has gotten more stable with respect to deep convection. To better understand the reasons for the changes in clouds, it would be useful to further investigate the effects of CO₂ and solar forcings on potential and equivalent potential temperature profiles.

Over land, existing research suggests that the reduction in low cloud fraction in G1 is a result of the physiological responses of plants to increased CO₂, as represented in the models' dynamic vegetation schemes. *Cao et al.* (2010) ran GCM simulations in which the CO₂ concentrations experienced by plants were doubled while the radiative fluxes were held constant, and found that low cloud fraction decreased in many vegetated land areas (see their Figure 1, central panel). The low cloud fraction decrease in the Cao et al. study is strongest in South America, eastern North America, southeast Asia, southeast Africa, and western Europe, which are the same areas of reduced low cloud cover in G1. The mechanism is that, when CO₂ concentrations are higher, plants' stomata do not need to open as much to take in the same amount of CO₂, leading to less transpiration of water from the plants (*Field et al.*, 1995). This causes a reduction in near-surface relative humidity over land, seen in both *Cao et al.* (2010, Figure 2) and G1 (*Smyth et al.*, 2017, Figure 5), which reduces the cloud fraction. In addition to plant physiology, it is possible that some of the reduction in relative humidity and cloud fraction over land in G1 is due to a reduction in evaporation directly caused by the reduction in surface SW radiation. The balance between these two quantities explains the reduction in global mean precipitation in G1 (*Kravitz et al.*, 2013c), since precipitation must balance evaporation, suggesting that a similar mechanism may affect cloud fraction. Over the ocean, however, near-surface relative humidity increases in G1 in most areas, despite the reduction in evaporation (*Smyth et al.*, 2017), implying that evaporation changes are not the reason for the low cloud changes there.

3.3.1 Calculation of LTS and EIS

I calculate LTS in the model output based on the surface pressure, surface air temperature, and the temperature at the model levels immediately above and below 700 hPa (over the ocean). Temperature is interpolated to 700 hPa in log pressure space, and the potential temperature is then calculated at 700 hPa and at the surface using the definitional formula:

$$\theta = T \left(\frac{p_0}{p} \right)^{\frac{R_d}{C_p}} \quad (3.5)$$

where T is the local temperature, p_0 is the reference pressure of 1000 hPa, p is either 700 hPa or the surface pressure, R_d is the gas constant for dry air, and C_p is the heat capacity of air at constant pressure. The values of θ at 700 hPa and the surface are then differenced in order to find the LTS. This calculation is done separately for each grid box and monthly mean before any further spatial or temporal averaging is done.

The calculation of EIS (defined in Equation 3.4) is more complex. In addition to the model output variables used to calculate the LTS, the surface specific humidity is also required. Besides the LTS, calculating the EIS also requires calculation of the LCL, the height of the 700 hPa surface, and the moist adiabatic lapse rate at 850 hPa.

Wood and Bretherton (2006) say there are “standard procedures” for calculating the LCL, not specifying exactly how to do this. I calculate the LCL using the formula given in Equation 6.16 of *Lamb and Verlinde* (2011):

$$\text{LCL} = \frac{T_0 - T_{d,0}}{.008 \text{ K m}^{-1}} \quad (3.6)$$

where T_0 is the surface temperature, $T_{d,0}$ is the surface dew point temperature, and the denominator is a representative value for the dry adiabatic lapse rate. The dew point temperature is calculated using the expression given by *Bolton* (1980, Eq. 11) (here rearranged to a more commonly used form):

$$T_d [\text{°C}] = \frac{243.5 \ln(e/6.112 \text{ hPa})}{17.67 - \ln(e/6.112 \text{ hPa})} \quad (3.7)$$

where e is the partial pressure of water vapor at the surface, in hPa, and the resulting T_d is in units of °C. (This equation was obtained by inverting an approximation of the Clausius-Clapeyron equation, which gives saturation vapor pressure as a function of temperature.) The partial pressure of water vapor is obtained by multiplying the surface specific humidity by the ratio of the molecular mass of dry air to that of water vapor, and then multiplying by the surface pressure.

The height of the 700 hPa surface is calculated assuming a constant scale height (*Wood and Bretherton, 2006*, Eq. 6):

$$z_{700} = (R_d T_0 / g) \ln(p_s / 700 \text{ hPa}) \quad (3.8)$$

where g is the acceleration due to gravity and p_s is the actual surface pressure in hPa.

Finally, the moist adiabatic lapse rate at 850 hPa is calculated using (*Wood and Bretherton, 2006*, Eq. 5):

$$\Gamma_m^{850} = \frac{g}{C_p} \left[1 - \frac{1 + L_v q_{\text{sat},850} / R_d T_{850}}{1 + L_v^2 q_{\text{sat},850} / C_p R_v T_{850}^2} \right] \quad (3.9)$$

where L_v is the latent heat of vaporization of water vapor, R_v is the gas constant of water vapor, T_{850} is the temperature at 850 hPa (approximated by averaging the 700 hPa and surface air temperature), and $q_{\text{sat},850}$ is the saturation mixing ratio at T_{850} . I calculate $q_{\text{sat},850}$ using

$$q_{\text{sat},850} = (e_{\text{sat},850} / 850 \text{ hPa}) \times (18/29) \quad (3.10)$$

where $e_{\text{sat},850}$ is the saturation vapor pressure at 850 hPa, calculated using the following approximate integrated form of the Clausius-Clapeyron equation (*Bolton, 1980*, Eq. 10):

$$e_{\text{sat},850} = (6.112 \text{ hPa}) \exp \left(\frac{17.67 T_{850} [\text{°C}]}{T_{850} [\text{°C}] + 243.5} \right). \quad (3.11)$$

3.4 Radiative effects

3.4.1 SW radiative effects

To calculate the SW radiative effects of changes in clouds and other atmospheric and surface properties, I use the approximate partial radiation perturbation (APRP) method introduced by

Taylor et al. (2007), which is based on a single-layer radiative transfer model of the atmosphere that can be expressed analytically and requires as inputs only the monthly mean surface and TOA radiative fluxes and total column cloud fraction outputs from the GCMs. APRP shows the radiative effects of physical changes in clouds, accounting for cloud masking effects, in which the differences between clear-sky and all-sky fluxes change in response to forcing without changes in the clouds themselves. The APRP calculations shown here are also used as inputs to the EBM energy transport attribution experiments in Chapter 2.

Figure 3.8 shows the multi-model mean change in net downward SW radiative flux at the TOA due to changes in clouds (Figure 3.8a), non-cloud atmospheric scattering and absorption (Figure 3.8b), and surface albedo (Figure 3.8c), calculated using APRP. Global mean radiative adjustments for the individual models in the SW and LW are shown in Table 3.2, which will be referred to in the discussion of the required solar forcing in G1 in Section 3.5. Clouds generally have a robust and widespread warming effect in the SW, in locations that closely correspond to the areas of reduced low cloud fraction shown in Figure 3.6a. The non-cloud atmosphere effects are very weak by comparison in the multi-model mean, but there are several models with appreciable positive values for this adjustment. Maps of this adjustment for the individual models (Figure S7 of the Supplemental Information for *Russotto and Ackerman*, 2018b) show that for HadGEM2-ES, it appears to be related to a reduction in atmospheric dust, since most of the warming effect occurs over and downwind of deserts; in IPSL-CM5A-LR, the effect is relatively spatially uniform but slightly stronger in higher latitudes. For surface albedo, there are warming effects in high latitudes from decreases in sea ice and snow cover associated with the residual polar warming in G1. There are also some warming effects in lower latitudes near desert regions, such as in the Sahel region; this may have to do with vegetation effects. There are several small regions, such as Tibet, with increases in surface albedo, presumably due to increased snow cover as a result of surface cooling there (*cf.* Figure 2 of *Kravitz et al.*, 2013a). Surface albedo effects are strong in some locations, such as the Sea of Okhotsk, but the relatively small area over which surface albedo changes can occur limits their importance in the global mean.

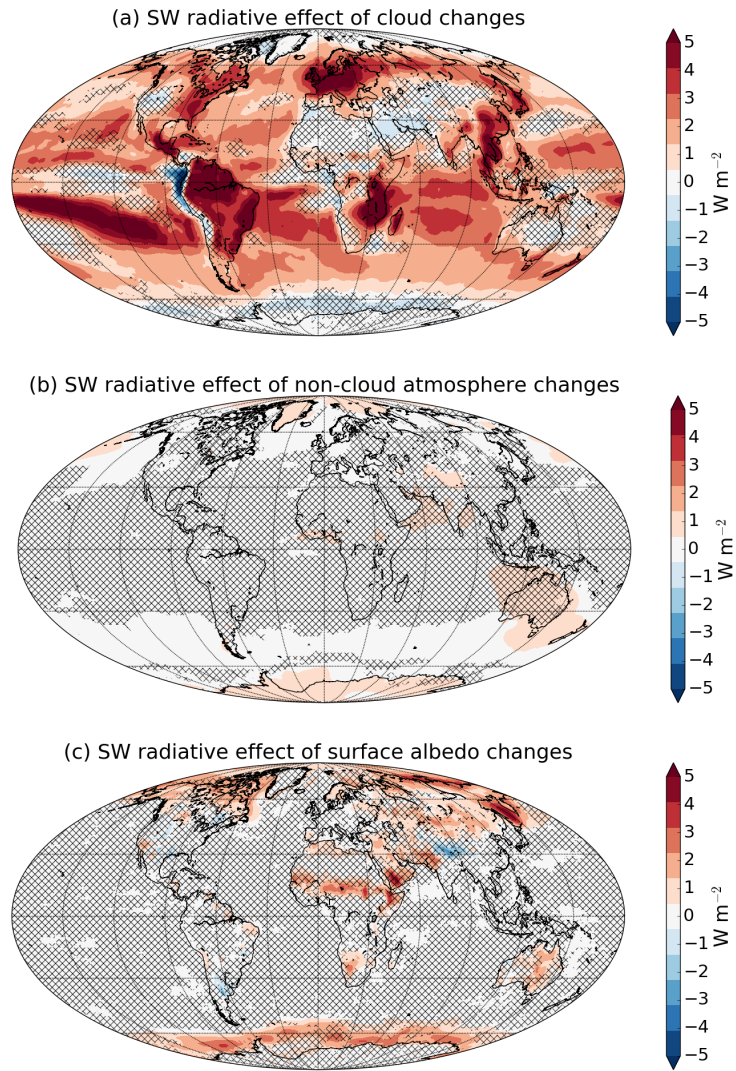


Figure 3.8: Multi-model mean change in net downward SW radiation at the TOA in G1 - piControl due to changes in cloud properties (a), non-cloud atmospheric absorption and scattering (b), and surface albedo (c), calculated using APRP method (*Taylor et al., 2007*). Hatching indicates areas where fewer than 7 of 9 models agree on the sign of the change. CSIRO-Mk3L-1-2 and GISS-E2-R models are excluded because not all fields necessary for APRP were correctly archived.

Table 3.2: Global mean radiative adjustments in G1 minus piControl, and excess and total solar forcing in G1, in W m^{-2} . Positive values indicate a warming effect (increase in absorbed SW radiation or decrease in OLR), except for solar forcing where positive values represent a cooling. SW adjustments correspond to multi-model means plotted in Figure 3.8. LW adjustments correspond to multi-model means plotted in Figures 3.9 and 3.10, with sign flipped for Figure 3.9. “Sum” is the sum of all the SW and LW adjustments. F_{excess} is calculated using Equation 3.13 and represents the actual instantaneous solar forcing (F_{solar}) in G1 minus that predicted based on CO₂ effective or instantaneous forcing. F_{solar} represents the total instantaneous solar forcing calculated from theory (Equation 3.15) or actually used in G1 (Equation 3.16).

Model	SW adjustments			LW adjustments				Sum	F_{excess}		F_{solar}	
	cloud	non-cloud	surface	T_a	T_s	H ₂ O	cloud		Eff.	Inst.	theory	actual
BNU-ESM	1.36	0.05	0.51	2.94	0.08	-0.78	-0.08	4.08	2.95	—	—	10.51
CanESM-2	1.44	0.41	-0.04	3.03	0.07	-1.04	-0.26	3.60	1.90	4.00	9.20	9.60
CCSM4	2.09	-0.05	0.28	2.53	-0.08	-0.84	0.13	4.05	2.55	4.44	9.56	9.95
CESM-CAM5.1-FV	0.71	-0.09	0.87	3.94	0.18	-1.39	0.30	4.52	—	—	—	11.26
CSIRO-Mk3L-1-2	—	—	—	2.16	0.03	-0.52	-0.24	—	—	—	—	—
GISS-E2-R	—	—	—	4.88	0.21	-1.78	-0.07	—	—	—	—	10.79
HadGEM2-ES	1.05	1.07	0.50	2.66	-0.05	-0.87	-0.15	4.21	3.56	3.91	9.76	9.46
IPSL-CM5A-LR	1.32	1.21	0.15	2.08	-0.05	-0.52	-0.86	3.35	2.01	3.85	7.75	8.25
MIROC-ESM	3.29	0.06	0.02	3.44	0.10	-1.11	-0.58	5.22	3.15	—	—	11.69
MPI-ESM-LR	2.63	-0.00	0.17	3.41	0.07	-1.10	-0.54	4.63	2.86	—	—	11.16
NorESM1	2.07	-0.20	0.05	2.88	0.08	-0.97	-0.10	3.82	3.00	3.87	9.34	9.42

3.4.2 LW radiative effects

The technique of radiative kernels (Held and Soden, 2006; Soden *et al.*, 2008; Shell *et al.*, 2008) was developed to quantify LW radiative adjustments and feedbacks using standard monthly mean climate model output. These kernels consist of matrices of the partial derivatives of OLR with respect to changes in surface temperature, atmospheric temperature, specific humidity, and greenhouse gas concentration as a function of latitude, longitude, month and (where applicable) pressure, calculated using offline calculations with a particular GCM’s radiative transfer code. Radiative kernels have been developed based on a variety of GCMs, including GFDL AM2 (Soden *et al.*, 2008), CAM3 (Shell *et al.*, 2008), MPI-ESM-LR (Block and Mauritsen, 2013), and

CESM-CAM5 (*Pendergrass et al.*, 2018).

I have applied the *Shell et al.* (2008) radiative kernels to the G1 ensemble. The choice of model used to generate the kernels has been shown to have little effect on the results (*Soden et al.*, 2008). After regridding the kernels to the latitude and longitude grid of each GCM, I multiplied them by the changes in temperature and the log of specific humidity, normalized by the standard anomaly used to compute the kernels (1 K for the surface and atmospheric temperature kernels, and the change in log specific humidity associated with a 1 K warming at constant relative humidity for the water vapor kernel), in order to compute the change in OLR associated with the changes in each of these quantities for G1 - piControl. I summed the OLR changes from each vertical level in order to get overall radiative adjustments from column temperature and water vapor changes, and I then analyzed the annual mean of these monthly adjustments.

Figure 3.9 shows multi-model mean changes in OLR for G1 - piControl calculated from the atmospheric temperature (a), surface temperature (b), and water vapor (c) kernels. Global means for the individual models are shown in Table 3.2. For the atmospheric temperature kernel, there is a strong decrease in OLR that is widespread across the globe and robust across models. This is associated with the cooling of the atmosphere and reduced longwave emission (*cf.* Figure 3.2). The reduction in OLR is stronger in the tropics than in the polar regions, and is due to some combination of upper tropospheric and stratospheric cooling. I discuss the contribution of the stratospheric component in the next section. Surface temperature changes have little effect on the TOA LW radiation balance, but there is a reduction in OLR in the tropics and subtropics and an increase in the polar regions that is consistent across models, due to the patterns of tropical cooling and polar warming at the surface. The OLR change from the surface temperature kernel is much smaller than that for atmospheric temperature because the atmosphere is not very transparent to LW radiation in most wavelengths, and because temperature changes are smaller at the surface than in the upper troposphere and stratosphere. Changes in water vapor concentration cause a robust cooling effect (increase in OLR) that partially offsets the warming effect from the atmospheric temperature kernel. The water vapor concentration decreases in the upper troposphere (Figure 3.3), which increases LW emission to space by low-

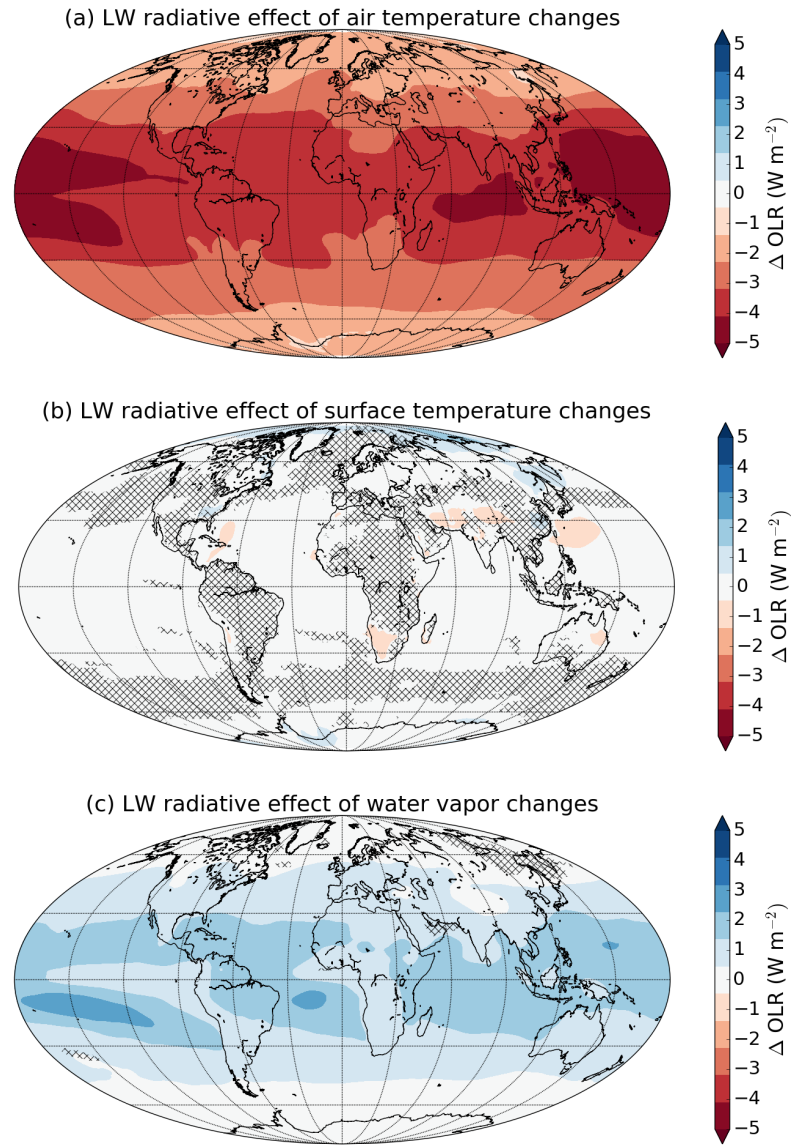


Figure 3.9: Multi-model mean change in OLR in G1 - piControl due to changes in atmospheric temperature (a), surface temperature (b), and specific humidity (c), calculated using radiative kernels (Shell *et al.*, 2008). Hatching indicates areas where fewer than 9 of 11 models agree on the sign of the change.

ering the effective altitude of emission.

In addition to the quantities plotted in Figure 3.9, radiative kernels can also be used to cal-

culate the effect of changes in cloud properties on OLR. This is often measured according to the change in the cloud radiative effect (CRE), which is the difference in OLR in clear-sky minus all-sky averages. However, changes in the cloud radiative effect may include cloud masking effects. We can correct the change in LW CRE for cloud masking using the difference in flux changes calculated according to clear-sky and all-sky kernels, following *Shell et al.* (2008):

$$\begin{aligned}\Delta \text{LWCRE}_{\text{adjusted}} = & \text{LWCRE}_{\text{G1}} - \text{LWCRE}_{\text{piControl}} \\ & + (\Delta \text{OLR}_{k,T} - \Delta \text{OLR}_{k,\text{clear}} + \Delta \text{OLR}_{k,T_s} - \Delta \text{OLR}_{k,T_s,\text{clear}} \\ & + \Delta \text{OLR}_{k,q} - \Delta \text{OLR}_{k,q,\text{clear}} + \Delta \text{OLR}_{k,\text{CO}_2} - \Delta \text{OLR}_{k,\text{CO}_2,\text{clear}})\end{aligned}\quad (3.12)$$

where, in the subscripts, k denotes a change in OLR calculated using a kernel, “clear” denotes quantities calculated using the clear-sky instead of all-sky kernels, T represents the atmospheric temperature kernel, T_s represents the surface temperature kernel, q represents the water vapor kernel, and CO_2 represents the greenhouse gas forcing kernel. Since the *Shell et al.* (2008) greenhouse forcing kernels were for a doubling of CO_2 , I doubled these kernels to obtain the radiative flux changes for a CO_2 quadrupling.²

Figure 3.10 shows the multi-model mean change in LW CRE calculated using Equation 3.12. There is a modest cooling effect in the global, multi-model mean (see also Table 3.2), but there are some places where there is a robust warming effect. The strongest warming effects occur near the eastern equatorial oceans, where the increase in high cloud fraction is greatest, while the strongest cooling effects occur in two belts in the eastern Pacific, which are associated with robust decreases in low and middle cloud fraction (*cf.* Figure 3.6). There are also widespread cooling effects over the mid-latitude oceans, where low cloud fraction decreases. Generally, an increase in high cloud fraction would be expected to result in a warming effect, because high clouds are much cooler than the surface and are more effective at trapping LW radiation. However, in the case of G1, it appears that the LW effect of the decrease in low cloud fraction compensates for this. Besides cloud fraction, LW radiation is also sensitive to changes in cloud

²The need for a CO_2 quadrupling kernel here is the reason I did not use the more recent CAM5 kernels calculated by *Pendergrass et al.* (2018). For that set of kernels, the greenhouse kernel was developed using the IPCC RCP8.5 scenario involving multiple greenhouse gases, which would be difficult to translate into a CO_2 quadrupling.

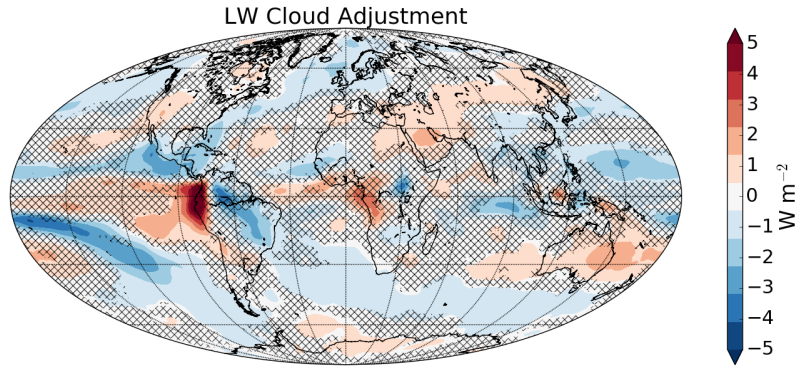


Figure 3.10: Multi-model mean change in LW cloud radiative effect in G1 - piControl, corrected for cloud masking of LW air temperature, surface temperature and water vapor adjustments and CO₂ forcing. Positive values indicate a decrease in OLR, *i.e.* a warming effect. Hatching indicates areas where fewer than 9 of 11 models agree on the sign of the change.

height and cloud optical depth (*Zelinka et al.*, 2012a), and the effect of the global mean increase in high cloud fraction in the multi-model mean on OLR may be limited effect on OLR because many of new clouds being formed are optically thin. We would especially expect this in the case of clouds in the stratosphere. The radiative effects of changes in cloud height and optical thickness are difficult to assess from the GeoMIP output currently available. These effects have been quantified in global warming simulations using cloud radiative kernels (*Zelinka et al.*, 2012b), but the use of these requires cloud fraction statistics binned by optical depth and cloud top height produced by the ISCCP satellite simulator (*Klein and Jakob*, 1999; *Webb et al.*, 2001) that is part of the CFMIP Observation Simulator Package (*Bodas-Salcedo et al.*, 2011). The simulator must be run inline with each GCM, or else requires instantaneous cloud fraction output from the GCMs (rather than monthly means) in order to be run retrospectively. The necessary outputs for cloud radiative kernels were saved in the Cloud Feedback Model Intercomparison Project (CFMIP; *Bony et al.*, 2011) but not in GeoMIP. It would be useful to follow the CFMIP protocols in future GeoMIP experiments in order to allow further quantitative analysis of the changes in clouds that occur under combined SW and LW forcings.

3.5 Theory of required solar reduction

Having quantified the radiative effects of changes in the physical properties of the atmosphere and surface in G1, I now revisit the question of the amount of solar constant reduction required to offset the quadrupling of CO₂. The solar constant reduction predicted based on effective CO₂ radiative forcing (Equation 3.1) systematically underestimated the actual reduction required (Figure 3.1b). In this section I attempt to account for this discrepancy by comparing the amount of extra solar forcing needed with the global means of the radiative adjustments calculated in Section 3.4. This comparison is shown in Figure 3.11 for the 8 models for which effective radiative forcing values from *Sherwood et al.* (2014) were available and all of the radiative adjustments could be calculated. The excess required solar reduction, F_{excess} , shown in black, is calculated according to:

$$F_{\text{excess}} = (\Delta S_0(\%)_{\text{actual}} - \Delta S_0(\%)_{\text{predicted}}) \times \frac{1361 \text{ W m}^{-2}}{100\%} \times \frac{1-\alpha}{4} \quad (3.13)$$

where $\Delta S_0(\%)_{\text{actual}}$ is listed in Table 1.2 and $\Delta S_0(\%)_{\text{predicted}}$ is calculated using Equation 3.2. In terms of radiative forcing, F_{excess} is the difference between the actual solar forcing required in G1 and the effective forcing from the CO₂ quadrupling.

The relative sizes of the bars in Figure 3.11 are fairly similar across models. The strongest warming effect is generally from the LW atmospheric temperature adjustment, followed by the SW cloud adjustment. The only consistent cooling effect comes from the LW water vapor adjustment. Surface albedo effects are generally small, as is the SW clear-sky adjustment, with the exceptions discussed in Section 3.4.1. The LW surface temperature adjustment is practically negligible in all models, while the LW cloud adjustment is also small but has an inter-model range of about 1 W m⁻². The model with the greatest cooling effect from the LW cloud adjustment, IPSL-CM5A-LR, is the model with the greatest global mean decrease in high cloud fraction, whereas most other models have an increase in high cloud fraction (Table 3.1).

Comparing the black and gray bars in Figure 3.11 shows that the sum of all the global mean radiative adjustments more than accounts for the additional solar constant reduction required to balance the CO₂ quadrupling, compared to the amount predicted by Equation 3.1. The fact

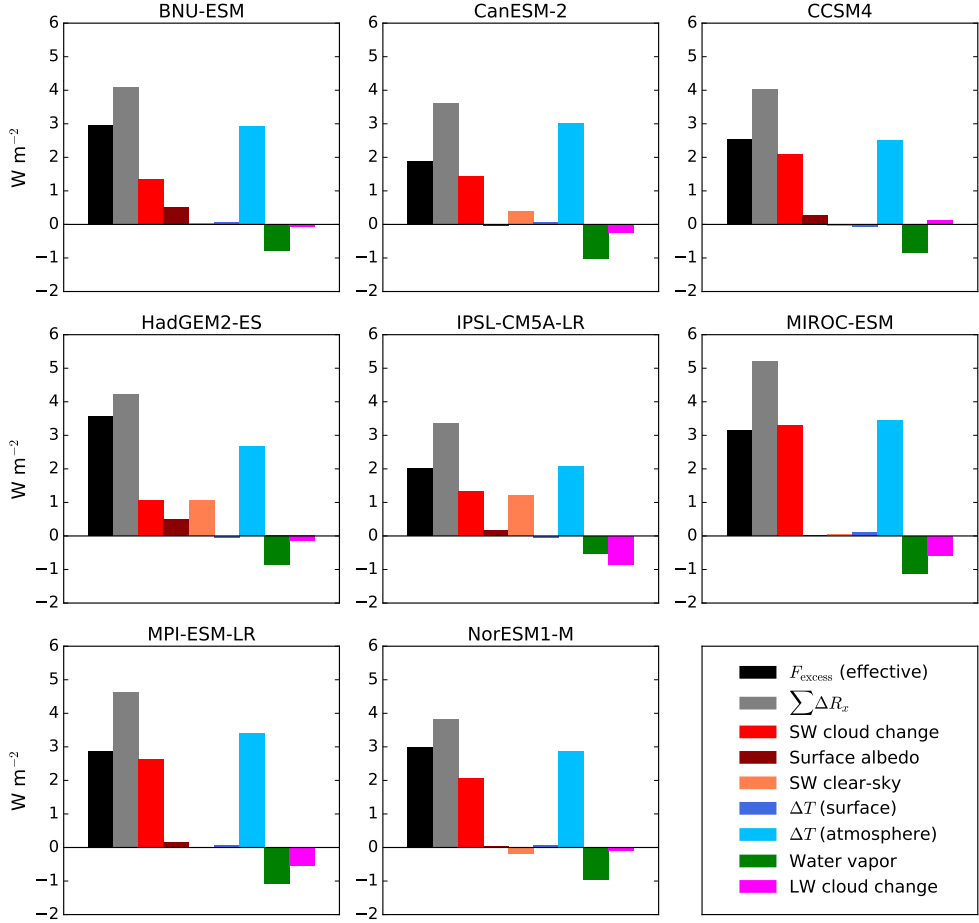


Figure 3.11: Excess required solar radiative forcing in G1 vs. that expected from effective CO₂ forcing (black bar), global mean SW and LW radiative adjustments (colored bars), and sum of all the radiative adjustments (gray bar), in models for which all of these quantities were calculated. For all except F_{excess} , positive values indicate a warming effect (increase in absorbed SW radiation or reduction in OLR). The first three colored bars correspond to the SW radiative adjustments calculated using APRP (multi-model mean maps shown in Figure 3.8). The three blue and green bars correspond to the LW radiative adjustments calculated using radiative kernels (multi-model mean maps shown in Figure 3.9). The magenta bar corresponds to the change in LW cloud radiative effect, corrected for cloud masking effects using radiative kernels (multi-model mean map shown in Figure 3.10).

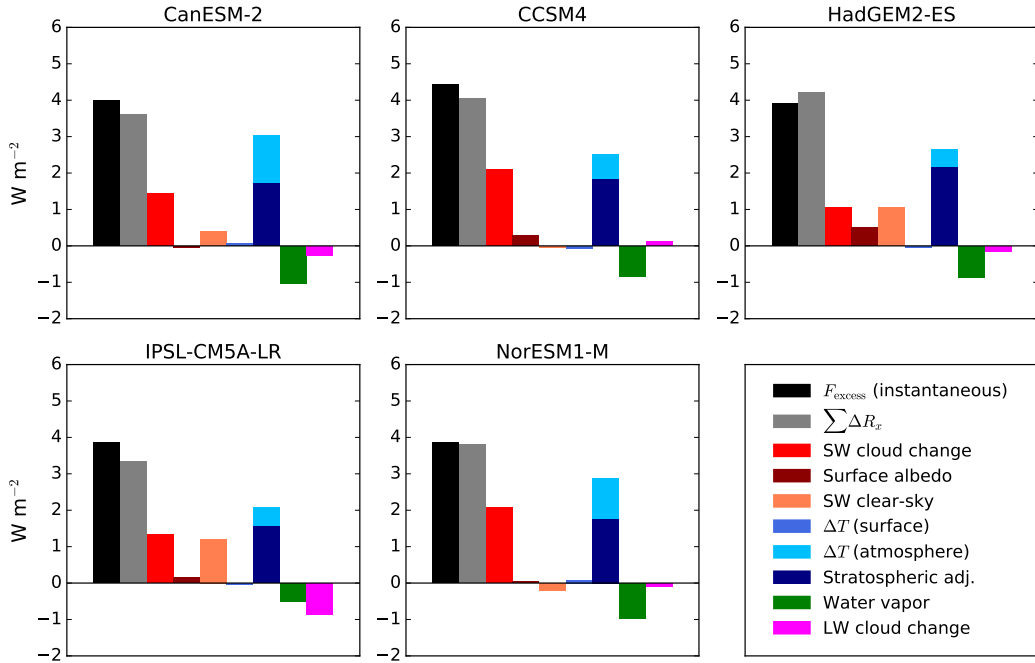


Figure 3.12: As in Figure 3.11 but with excess solar forcing calculated using instantaneous instead of effective CO₂ radiative forcing. Navy blue bar indicates the reduction in OLR due to stratospheric temperature adjustment from CO₂ quadrupling given by *Zhang and Huang* (2014), to illustrate the portion of the atmospheric temperature adjustment to G1 attributable to stratospheric cooling.

that the sum of the radiative adjustments consistently overestimates F_{excess} points to the fact that this is not really a fair comparison. Rapid adjustments to a CO₂ quadrupling by itself, which were included in the calculation of effective CO₂ radiative forcing, are being double-counted, because they also show up in the radiative adjustments to the G1 combined forcing, to the extent that they are not canceled by the solar reduction.

To account for this, I plot in Figure 3.12 the same quantities as in Figure 3.11 but where the black bars are calculated using instantaneous rather than effective CO₂ forcing for the predicted solar constant reduction (*i.e.* using $F_{4x\text{CO}_2,\text{inst}}$ rather than $F_{4x\text{CO}_2,\text{eff}}$ in Equation 3.2 and then substituting into Equation 3.13). By using instantaneous forcing, we can test the hypothesis presented in Equation 3.3, that the solar radiative forcing that balances a CO₂ quadrupling

is equal to the instantaneous CO₂ forcing plus the sum of the radiative adjustments to the combined CO₂ and solar forcings. Expressed mathematically, the comparison done in Figure 3.12 is:

$$\left((\Delta S_0(\%))_{\text{actual}} \times \frac{1361 \text{ W m}^{-2}}{100\%} - 4 \times \frac{F_{4x\text{CO}_2,\text{inst}}}{1-\alpha} \right) \times \frac{1-\alpha}{4} \stackrel{?}{=} \sum \Delta R_X . \quad (3.14)$$

The black bars in Figure 3.12 show the left hand side of the Equation 3.14 while the gray bars show the right hand side. If the two bars are the same size, that means that the actual solar constant reduction will be equal to that predicted by Equation 3.

Instantaneous forcing, unlike effective forcing, cannot be calculated from monthly mean model output through a simple linear regression of TOA flux changes against surface temperature; instead it requires running each GCM's radiative transfer code offline with standard and quadrupled CO₂ concentrations. For this reason, estimates of instantaneous CO₂ forcing are available for fewer models than for effective forcing. I use the “double call” instantaneous forcing estimates from the CMIP5 archive shown in *Chung and Soden* (2015) for the CanESM-2 and IPSL-CM5A-LR models.³ For three other models (CCSM4, HadGEM2-ES, and NorESM1-M), I use estimates of instantaneous CO₂ forcing given by *Zhang and Huang* (2014) based on residuals between total TOA flux changes and radiative responses calculated with radiative kernels.

In Figure 3.12, the black and gray bars match to within about 10%, indicating that the theory expressed in Equation 3.3 works well for explaining the amount of solar constant reduction required to balance a CO₂ increase. The agreement is quite remarkable considering that the methods used to calculate the radiative adjustments are approximate. In evaluating the theory, it is useful to express it in terms of total instantaneous solar forcing rather than solar constant reduction:

$$F_{\text{solar,predicted}} = F_{4x\text{CO}_2,\text{inst}} + \sum \Delta R_X \quad (3.15)$$

and compare it to the actual solar forcing in G1:

$$F_{\text{solar,actual}} = \Delta S_0(\%) \times \frac{1361 \text{ W m}^{-2}}{100\%} \times \frac{1-\alpha}{4} . \quad (3.16)$$

³Eui-Seok Chung provided me with the numbers corresponding to the figures in *Chung and Soden* (2015).

These values are listed in the last two columns of Table 3.2. The errors in the total solar forcing in G1 predicted by Equation 3.15 are all within 0.5 W m^{-2} , or about 6%, of the total, indicating that the instantaneous solar forcing required to balance an abrupt CO₂ increase is well predicted by the sum of the instantaneous CO₂ forcing and the radiative adjustments to the combined forcings.

The two largest radiative adjustments to the G1 forcing scenario are the LW atmospheric temperature adjustment and the SW cloud adjustment. Since the temperature adjustment contains effects of both stratospheric and tropospheric temperature changes, it is worth trying to understand the partitioning between these effects. I have overlaid the OLR reduction due to the stratospheric cooling in abrupt4xCO₂ given by *Zhang and Huang* (2014) onto the ΔT (atmosphere) bar in Figure 3.12. This shows that between about 50% to 75%, depending on the model, of the atmospheric temperature radiative adjustment in G1 is due to cooling of the stratosphere by the increase in CO₂. The rest is due to a combination of the additional cooling of the stratosphere from the reduction in insolation and the cooling of the upper troposphere which arises from the surface cooling in the tropics. The water vapor adjustment roughly compensates for the tropospheric component of the temperature adjustment, and these effects are physically linked because a cooler atmosphere emits less LW radiation but also contains less water vapor to absorb radiation from below. Therefore, the main reasons why the instantaneous solar forcing must be greater than the instantaneous CO₂ forcing in order to maintain energy balance are the failure to undo the stratospheric cooling and the reduction in low cloud fraction.

3.6 Chapter conclusions

Here I summarize the results of this chapter and explain how they may be useful for future Ge-oMIP phases. Implications for future research into solar climate forcings and for the possibility of testing and implementing solar geoengineering are discussed in Sections 5.1 and 5.2, respectively.

The amount of solar constant reduction required to offset an increase in CO₂ concentration in terms of TOA radiative balance and global mean temperature is an interesting question with

implications for assessing the feasibility of solar geoengineering scenarios and for improving our theoretical understanding of the response of Earth's climate to greenhouse gas and solar forcings. This chapter explained why some intuitive predictions of the solar constant reduction are inaccurate, laid out an alternative hypothesis that the solar constant reduction can be explained based on instantaneous CO₂ forcings and radiative adjustments, and quantified various radiative responses to the GeoMIP G1 scenario in order to test this hypothesis.

In the G1 experiment, at the surface, the tropics cool and the poles warm while global mean temperature remains at preindustrial. The upper troposphere experiences cooling at all latitudes, with the tropical upper troposphere cooling more than the surface. The stratosphere cools more than anywhere else in the atmosphere, due primarily to the CO₂ increase (*Govindasamy et al.*, 2003). The tropospheric temperature effect is a reversal of the negative lapse rate feedback that happens in global warming simulations, in which the tropical upper troposphere warms more than the surface; in G1, because the tropics cool and the tropical temperature profile tends to follow a moist adiabat, the upper troposphere also cools, which has a warming effect on the climate by reducing OLR. Atmospheric specific humidity is reduced in the upper troposphere, which makes the atmosphere less opaque to LW radiation and largely offsets the radiative effect of the tropospheric cooling. Low cloud fraction exhibits a widespread decrease over the ocean and vegetated land areas in all models, which I attribute to decreases in boundary layer inversion strength over the ocean and reduced evaporation from plants due to the physiological response to increased CO₂ over land. The low cloud fraction reduction has a strong surface warming effect due to reduced reflection of sunlight by the clouds. High cloud fraction increases in the global mean in most models, but the LW radiative effect of cloud changes in G1 is slightly negative in the global, multi-model mean. When all the global mean radiative adjustments in G1 are added together, the results account, to within 10%, for the difference between the solar constant reduction that would match the instantaneous CO₂ forcing and the tuned solar constant reduction that met the TOA energy balance threshold required by the G1 experiment protocol.

For future model runs of the G1 experiment, such as those being prepared for the next phase

of GeoMIP corresponding to CMIP Phase 6 (*Kravitz et al.*, 2015a), it would be useful to have a better initial guess for the solar constant reduction in order to reduce the necessary amount of tuning. Using Equation 3.3 for this purpose would be tricky because the radiative responses to the combined CO₂ and solar forcings would be unknown before actually running the model. However, one could simply substitute an empirical value of about 4 W m⁻², a typical value for the sum of the radiative adjustments in G1 (Figure 3.11), for $\sum \Delta R_X$ in Equation 3.3. Then, tuning would only need to account for model-specific deviations from this number. If instantaneous CO₂ forcing was not available for a particular model, the modelers could add a correction of about 2.5 to 3 W m⁻², a typical value for the black bars in Figure 3.11, to the effective CO₂ forcing in Equation 3.1.

Chapter 4

CHANGES IN THE SEASONAL CYCLE

The seasons are driven by cyclical changes in insolation that occur as a result of Earth's axial tilt. It seems intuitive that reducing the total amount of insolation, as done in G1, would have impacts on the seasonal cycle. This chapter analyzes changes in the seasonality of precipitation (Section 4.1) and temperature (Section 4.2) under the G1 forcing scenario.

4.1 Changes in the seasonal migration of the ITCZ

Following a meeting at the 6th GeoMIP Workshop in Oslo, Norway, in June 2016, I was asked to contribute a version of Figure 2.4b to a paper written mainly by Jane Smyth and Trude Storelvmo (*Smyth et al.*, 2017). The main focus of the paper was on the relative contributions of thermodynamic and dynamic effects on hydrologic cycle changes in the G1 experiment. One of the reviewers of the paper suggested examining the seasonal cycle of circulation changes. As a result, I analyzed the ITCZ position in different monthly and seasonal averages in addition to the annual mean analysis presented in Chapter 2.

The latitude of the ITCZ migrates between the Northern and Southern Hemispheres every year in a nearly sinusoidal pattern, being furthest north in July, August and September and furthest south in January, February and March. This migration can be seen in satellite observations (*Waliser and Gautier*, 1993). The physics governing this seasonal migration are similar to those governing ITCZ shifts over longer time scales. In the summer hemisphere, there is greater solar energy input into the northern hemisphere, resulting in increased atmospheric energy transport into the winter hemisphere by the Hadley circulation. Net energy transport by the Hadley cell moves in the direction of the upper branch, but moisture is transported by the lower branch,

because the water vapor column is much more heavily weighted closer to the ground. Therefore, there is a transport of water vapor towards the summer hemisphere by the Hadley cell, which results in the ITCZ moving into the summer hemisphere. Strong correlations of the seasonal ITCZ position with the inter-hemispheric temperature contrast, and with cross-equatorial atmospheric energy transport, have been diagnosed from observations (*Donohoe et al.*, 2013).

Solar constant reductions would be expected to preferentially cool the summer hemisphere, because there is more sunlight in that hemisphere; CO₂, meanwhile, preferentially warms the winter hemisphere (to see this, compare the DJF and JJA temperature anomaly plots for abrupt4xCO₂ - piControl in Figure 2 of *Kravitz et al.*, 2013a). Together, these effects imply a warming of the winter hemisphere relative to the summer hemisphere in the G1 experiment, which would be expected to result in a dampening of the seasonal ITCZ migration. I have made several plots that show that this effect does, indeed, occur.

Figure 4.1a shows the multi-model mean ITCZ positions in each month in piControl (years 1-40) and G1 (years 11-50). To separate the effect of the movement of the ITCZ from any changes in the annual mean ITCZ position, I subtracted out the annual mean position for each model before doing further calculations. Both curves show a roughly sinusoidal migration in the ITCZ position, with the southernmost position occurring in February and the northernmost position occurring in August. There is no phase shift apparent, but the ITCZ does not reach as far southward February or as far northward in August in G1 compared with piControl. This indicates that the seasonal migration of the ITCZ is weakened in G1.

To see if this effect is robust across different models, I have plotted in Figure 4.1b the difference in the deviation of the monthly ITCZ position from the annual mean between G1 and piControl, or in other words, the reduction in the ITCZ seasonal migration in each model as a result of the G1 radiative forcing scenario. This plot shows that in 10 out of 11 models, the ITCZ is further south relative to its annual mean position in the boreal summer months and further north relative to its annual mean position in the boreal winter months. (The exception model, CanESM-2, has little change overall in the ITCZ migration.) The effect is modest, amounting to a reduction in the seasonal ITCZ migration of about half a degree latitude, or about 55 km,

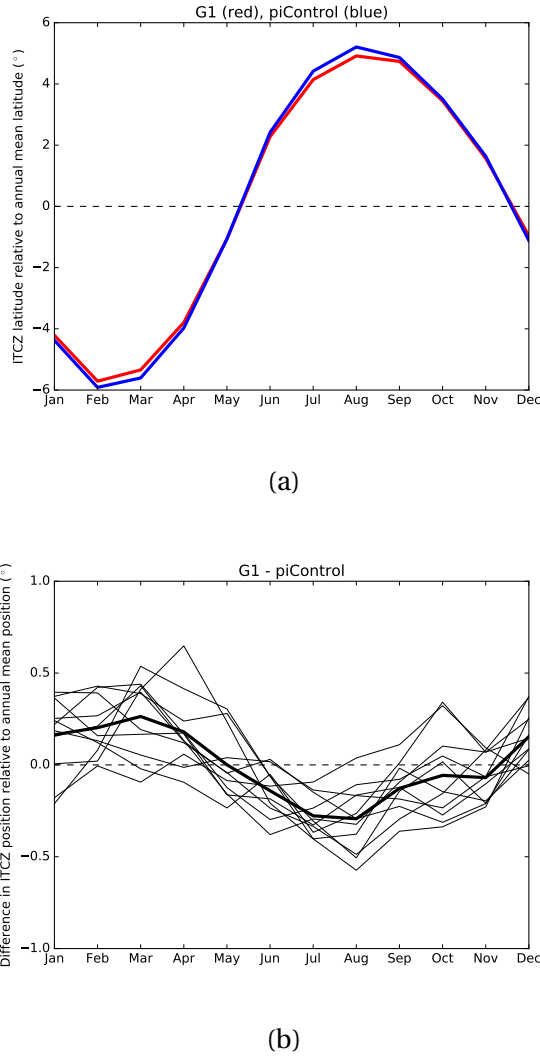


Figure 4.1: (a): Monthly ITCZ deviation from annual mean position in multi-model mean, in G1 (years 11-50) and piControl (years 1-40). (b): Difference between G1 and piControl ITCZ deviation from annual mean in each month, in each of 11 GeoMIP models. Thick line is the multi-model mean difference. The mean of the 12 monthly means was subtracted from each month's position before multi-model mean calculations or difference between runs were taken. 11 GeoMIP models were included in this calculation (all models listed in Table 1.2 except CSIRO-Mk3L-1-2).

in the multi-model mean. But the robustness across models implies that this is a real physical response to the imposition of a simultaneous CO₂ increase and solar constant reduction.

Another way of looking at this is to examine the ITCZ position in seasonal means, as shown in Figure 4.2. The figure shows JFM (January, February and March), JAS (July, August and September), and annual mean ITCZ latitudes in each model in piControl and G1 along a horizontal axis.¹ The length of the line between the JFM and JAS position can be thought of as the extent of the ITCZ seasonal migration. In this plot, the ITCZ seasonal migration is weakened in all 11 models included.²

To better understand the connection between these plots and the differential temperature response in the different hemispheres, Figure 4.3 shows the correlations between the ITCZ shift and the change in the inter-hemispheric temperature contrast from piControl to G1 in the annual (a), JAS (b) and JFM (c) means. There is a positive correlation between the ITCZ shift and the warming of the northern hemisphere relative to the southern hemisphere in both seasonal means. The correlation is somewhat weaker in the seasonal means than in the annual mean, but it is consistent with the idea that solar reduction preferentially cools the summer hemisphere while CO₂ increase preferentially warms the winter hemisphere,³ dampening the ITCZ seasonal migration. In the boreal winter, the amount by which the summer hemisphere is warmer than the winter hemisphere is reduced in G1 compared to piControl in all 11 models included in this analysis (Figure 4.3c). In the boreal summer (Figure 4.3b), the same effect occurs in all but 3 models. These 3 models all have a northward ITCZ shift in the annual mean.

The physical connection between summer hemisphere cooling and a weakened ITCZ seasonal migration is bolstered by examining the difference in the Hadley circulation stream func-

¹I used JFM and JAS means instead of the more common DJF and JJA for consistency with other plots made by Jane Smyth that were in the paper. The use of these months makes sense here because the extreme positions of the climatological ITCZ position occur in February and August.

²Seasonal and annual means in this figure were calculated by first taking the average precipitation across 40 years of monthly model output in either the summer, winter or all months (weighting each month by the number of days in the month output), then taking a zonal mean and calculating the latitude of median precipitation in the tropics. This gives slightly different annual means from the method used in Figure 4.1.)

³I do not know the relative importance of these two effects. Experiments that imposed only a solar or CO₂ forcing would be subjected to confounding effects from large global warming or cooling.

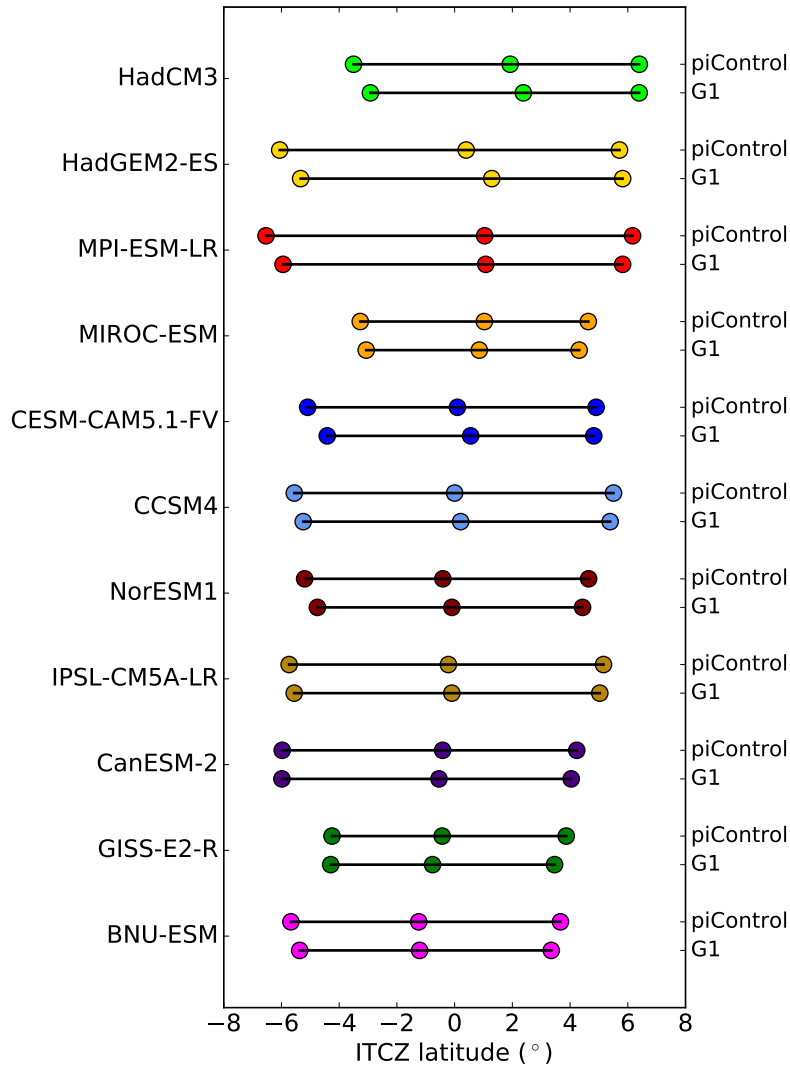


Figure 4.2: ITCZ position in each model in piControl (years 1-40) and G1 (years 11-50). For each model, there are two rows of three dots, one for piControl and one for G1. In each row, the left dot is the JFM (January, February and March) average position, the middle dot is the annual mean position, and the right dot is the JAS (July, August and September) position. The length of the horizontal line connecting the dots shows the extent of the ITCZ seasonal migration; this migration is dampened in every model in G1 compared with piControl. This figure was contributed to *Smyth et al.* (2017) (Figure 10).

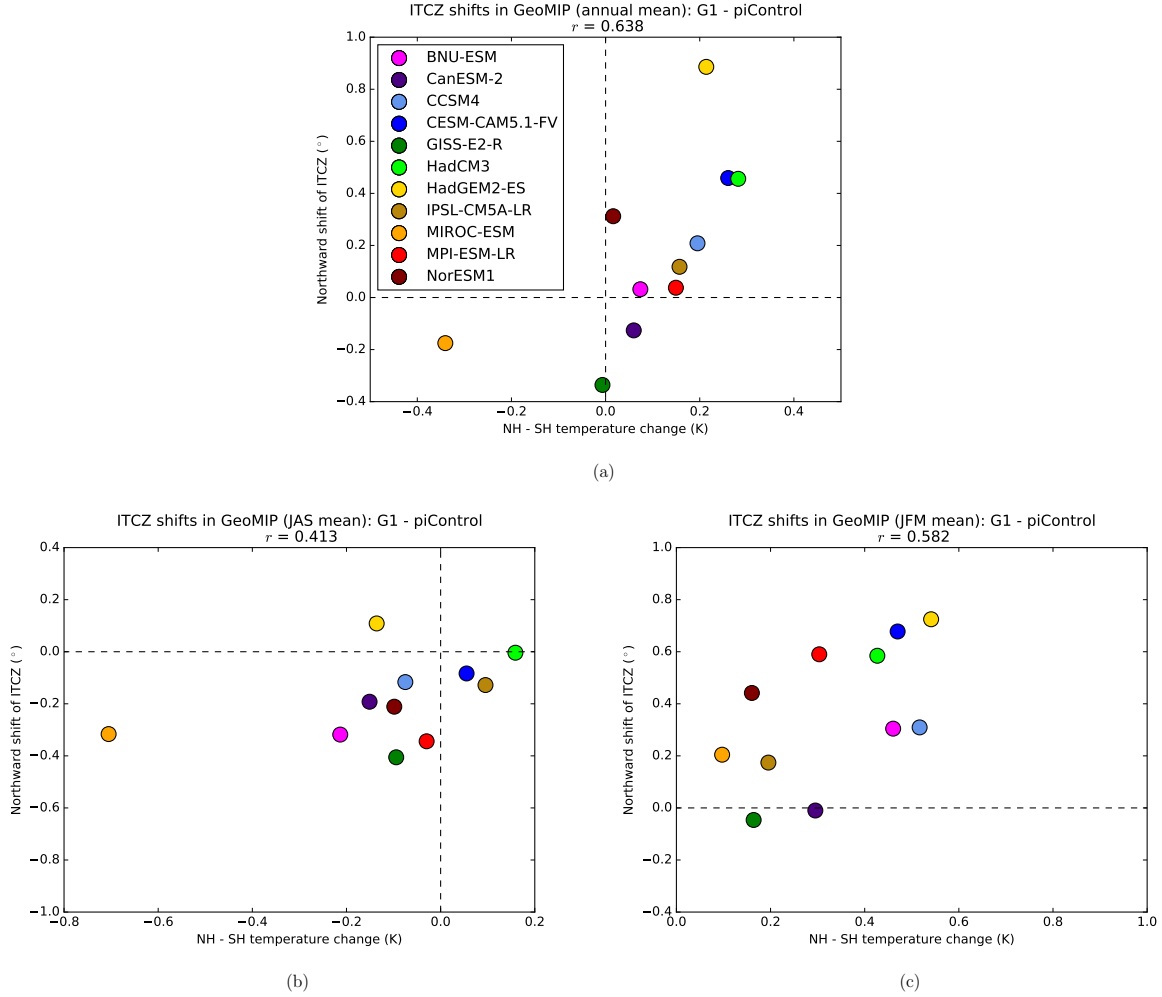


Figure 4.3: ITCZ shift in G1 minus piControl scattered against northern hemisphere warming relative to southern hemisphere in (a) annual mean, (b) boreal summer (JAS) mean, and (c) boreal winter (JFM) mean. Panel (a) is the same as Figure 2.4b except that a slightly different set of models is used here. This figure was contributed to *Smyth et al. (2017)* (Figure 9).

tion between G1 and piControl. Jane Smyth made plots of these stream function differences in the JAS and JFM means, which show a weakening of the Hadley cell that transports energy from the summer to the winter hemisphere in most models. These plots appear as Figures 7 and 8 of *Smyth et al. (2017)*.

A logical question to ask would be whether similar changes in ITCZ seasonal migration occur under increased CO₂ without offsetting solar reductions. There is some evidence in the literature for changes in the ITCZ seasonal cycle under global warming conditions, but more research in this area would be helpful. Under GCM simulations of warming caused by greenhouse gas increases, the seasonal cycle of monsoon precipitation over the Sahel (the regional manifestation of ITCZ migration over Africa) is delayed (*Biasutti and Sobel*, 2009), and empirical orthogonal function (EOF) analyses of tropical precipitation have found a phase delay in the ITCZ seasonal migration (*Biasutti and Sobel*, 2009; *Dwyer et al.*, 2014). *Dwyer et al.* (2014) also found an increase in the amplitude of the seasonal cycle of the EOF associated with ITCZ migration, but this could reflect increases in the intensity of precipitation in the ITCZ rather than changes in the extreme positions reached. A monthly analysis of the median precipitation location similar to what I did in the G1 experiment would be useful here. The abrupt4xCO₂ experiment may not be the most appropriate for this analysis, because the abrupt quadrupling of CO₂ without offsetting solar reductions throws the Earth system far out of energy balance.

4.2 Changes in the amplitude of the seasonal temperature cycle

After I gave a department seminar on the work described in Chapter 2 and Section 4.1, Aaron Donohoe suggested that I investigate the seasonal cycle more deeply, using annual harmonic methods that he had used in the past (*Donohoe and Battisti*, 2013; *Donohoe et al.*, 2013). *Donohoe and Battisti* (2013) studied the seasonal amplitude of temperature on a latitude-height basis in climatology in both observations and reanalysis products, and in climate model runs for doubled CO₂ concentrations. I have done a similar analysis to see how the seasonal cycle of temperature changes in G1 at various latitudes and heights in the atmosphere.

Aaron Donohoe provided me with a simple Matlab script for calculating the annual harmonic, which I adapted into a Python function for this analysis. This methodology is very versatile, being applicable to any climatological averages with monthly or daily temporal resolution on any spatial scale. For my analysis, following *Donohoe and Battisti* (2013), I calculated 40-year means in each month of zonal mean temperature at each latitude and pressure level in

each model and then applied the annual harmonic code to these climatologies.

The annual harmonic is calculated by projecting the 12-element vector \vec{A} of multi-year monthly means onto unit cosine and sine vectors \vec{C} and \vec{S} with a 12-month period:

$$A_{\cos} = \overline{2\vec{A} \cdot \vec{C}} \quad (4.1)$$

$$A_{\sin} = \overline{2\vec{A} \cdot \vec{S}} \quad (4.2)$$

where the overbar denotes a mean over the 12 months and the multiplication by 2 accounts for the fact that the average of the square of the cosine function is 1/2, so that for a pure cosine function A_{\cos} would be equal to 1. The overall amplitude of the seasonal variation can be found by adding A_{\cos} and A_{\sin} in quadrature, and the phase of the peak of the temperature cycle can be calculated from A_{\cos} and A_{\sin} using the arctangent function.

Figures 4.4a and b show the climatological amplitude and phase, respectively, of zonal mean temperature in an example model, CCSM4.⁴ Plots for the other models (not shown) are very similar. Comparing Figure 4.4a to Figure 4 of *Donohoe and Battisti* (2013), which was based on observations, indicates that the CMIP5 models are able to reproduce the observed seasonal amplitude of temperature. Multi-model mean changes in amplitude are shown in Figure 4.4c, for G1 - piControl, and Figure 4.4d, for abrupt4xCO2 - piControl. Figure 4.4d is similar to Figure 10 of *Donohoe and Battisti* (2013), generally showing an increase in temperature amplitude throughout the troposphere near 40°N and S; an increase aloft and a decrease near the surface in the Arctic; and a decrease near the surface in the Antarctic, without much of an increase aloft there. *Donohoe and Battisti* (2013) attribute the areas of increased temperature amplitude to increases in the absorption of SW radiation by water vapor, which is what drives the climatological seasonality of atmospheric temperature. They attribute the decreases in temperature amplitude near the surface to reductions in sea ice cover, which reduces the exchange of heat between the surface and the lower atmosphere due to the open ocean's high heat capacity.

⁴Unlike the other zonal mean plots, those in Figure 4.4 have latitude instead of sine latitude on the x-axis, because in this case the behavior in the tropics is not important and using sine latitude would emphasize the tropics too much.

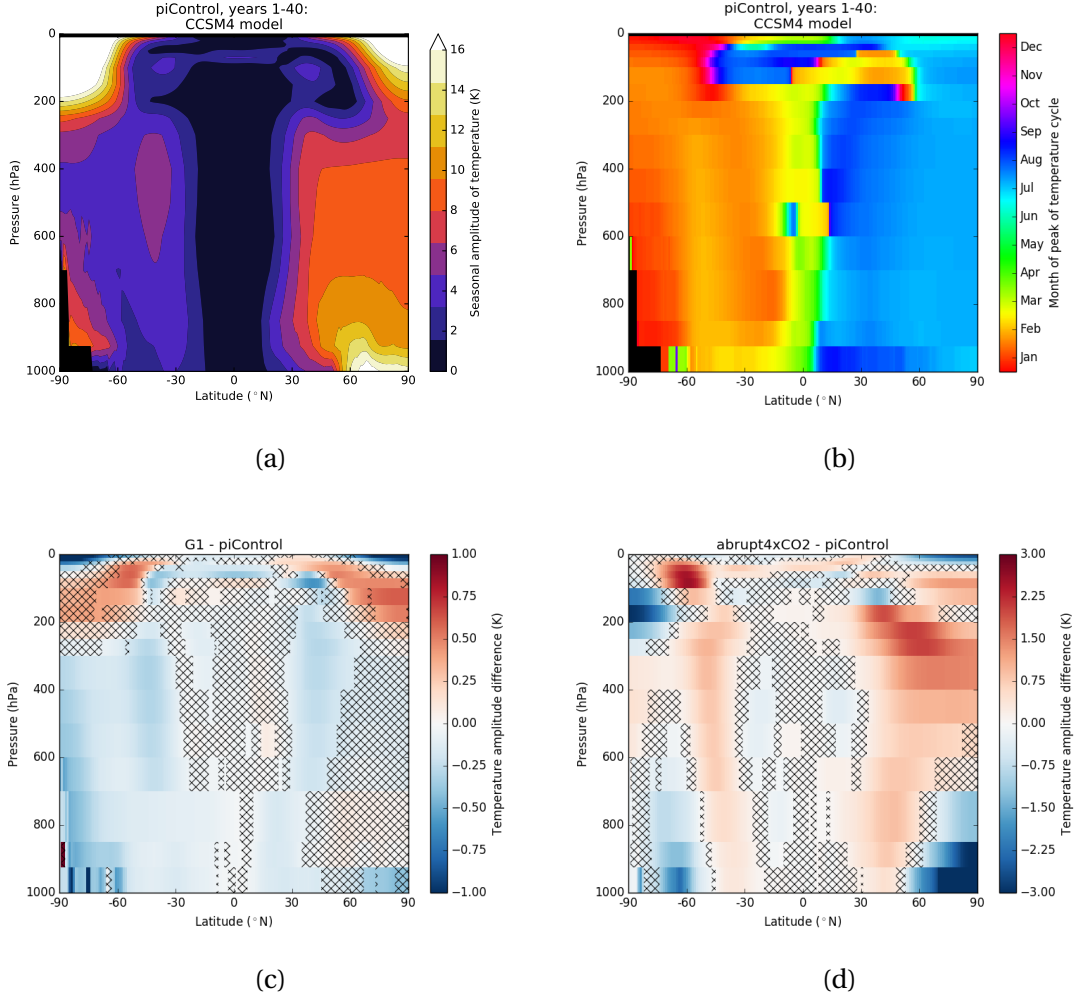


Figure 4.4: Amplitude (a) and phase (b) of the seasonal cycle of zonal mean temperature in an example model, CCSM4, and multi-model mean change in amplitude in G1 - piControl (c) and abrupt4xCO2 (d). For (c) and (d), stippling indicates where fewer than 9 of 11 models agree on the sign of the change.

For G1 - piControl (Figure 4.4c), there is a decrease in the seasonal temperature amplitude throughout the troposphere in the mid-latitudes and the Antarctic. This is not surprising, since by reducing the solar constant we are reducing the seasonal cycle of SW absorption by water vapor even if water vapor concentrations do not change. However, there is also less water vapor in most of the troposphere (Figure 3.3), which would also reduce SW absorption. I have

not attempted to partition these effects; to do so would require analyzing changes in the seasonal cycle of various components of the atmospheric energy budget, as done by *Donohoe and Battisti* (2013).

Donohoe and Battisti (2013) did not analyze changes in the seasonal temperature amplitude above the 200 hPa level, roughly corresponding to the stratosphere. My plots show that there are some robust changes here with intricate spatial structure. For abrupt4xCO₂ - piControl, the areas where this occurs seem almost random, so it might be tempting to ascribe these to chance, but considering the complexity of interactions between chemistry, radiation, dynamics, and thermodynamics in the stratosphere, there might be a physical explanation that could be worked out. For G1 - piControl at these altitudes, there are three concentric “shells” of changes of different signs. There is a reduced amplitude of temperature in the tropics, with structure corresponding to the climatological amplitude; a region of increased amplitude above and poleward of this; and reduced amplitude above about 30 hPa in high latitudes. Since the stratosphere is heated by absorption of ultraviolet radiation, it is not surprising that a reduction in insolation would reduce the seasonal amplitude of temperature in some areas. But an increased seasonal amplitude of temperature would not be expected to result from a decrease in insolation anywhere—unless the phase of the cycle was reversed such that the climatological temperature was maximized when insolation was minimized, but the only place where this is the case (see Figure 4.4b) is a region where the amplitude decreases. This suggests that the area of temperature amplitude increase in G1 is due to the CO₂ increase, an idea which is bolstered by there being an increase in amplitude in a similar area in abrupt4xCO₂. But there are other possible explanations. The Brewer-Dobson circulation injects air from the tropical troposphere primarily into the winter hemisphere, so changes in the properties of tropical upper tropospheric air could affect stratospheric seasonality. Also, changes in the quasi-biennial oscillation under solar geoengineering (*Aquila et al.*, 2014) could project onto the amplitude of temperature; however, the QBO is not well represented in most GCMs, and its period is model-dependent, so this would not be expected to explain the robust behavior. Not being an expert on stratospheric dynamics, I could be missing something in the literature, but I think there

needs to be more investigation of how the seasonal amplitude of temperature in the stratosphere changes under both CO₂ and solar forcings.

Similar methods to those used here could be used to revisit changes in the seasonal cycle of precipitation. The annual harmonic code could be applied to the time series of the location of the ITCZ, using similar methods to *Donohoe et al.* (2013), but is also versatile in that it could be used to study changes in the seasonal cycle of precipitation in G1 in a variety of locations, both tropical and extratropical. This could help understand how much of an apparent narrowing of the annual mean ITCZ in G1 (*Tilmes et al.*, 2013, Figure 5) is due to the reduction in the seasonal migration and how much is an instantaneous change in structure. It could also be used to better understand the relationships between precipitation and changes in the column energy budget and meridional energy transport on seasonal time scales.

Chapter 5

CONCLUSIONS AND IMPLICATIONS

Revisiting the research questions enumerated in Section 1.1, the major conclusions of my dissertation are as follows: In the GeoMIP G1 experiment, in which the solar constant is reduced to compensate for an abrupt quadrupling of CO₂,

1. Poleward energy transport is weakened, due to reductions in both latent and dry static energy transport. This implies that the canonical pattern of polar warming and tropical cooling in G1 must be directly due to the imposition of a net negative forcing in the tropics and a net positive forcing at the poles. The reduction in poleward energy transport, versus an increase under global warming, explains why the residual polar amplification in G1 is much less than the polar amplification in CO₂ quadrupling simulations. Changes in cross-equatorial energy transport are anticorrelated with annual mean shifts in the ITCZ across models. Changes in SW and LW cloud radiative effects are the largest contributor to inter-model spread in both cross-equatorial and mid-latitude atmospheric energy transport.
2. Low cloud fraction is reduced in all models while high cloud fraction is increased in most models. Most of the troposphere is cooled, with corresponding reductions in specific humidity; tropospheric cooling is greater aloft than at the surface. The stratosphere is cooled mostly due to the increase in CO₂. Reductions in overall cloud albedo and the tropospheric and stratospheric cooling have large warming effects at the top of atmosphere, while the reduction in water vapor roughly offsets the tropospheric cooling. The amount of solar forcing required to balance the CO₂ quadrupling is well explained by the sum of the instantaneous CO₂ forcing and the various TOA radiative adjustments to the com-

bined forcing. The formula used by the modeling groups based on effective CO₂ radiative forcing underestimates the required solar reduction because it does not consider rapid adjustments to the reduction in insolation.

3. The seasonal cycle of the ITCZ migration is dampened due to preferential cooling of the summer hemisphere. The amplitude of the seasonal temperature cycle is reduced in much of the troposphere due to reductions in insolation and water vapor concentrations. There is an increase in seasonal temperature amplitude in parts of the stratosphere.

The rest of this chapter discusses broader implications of my work and suggestions for future research directions.

5.1 Implications for future modeling work into CO₂ and solar forcings

The analysis in Chapter 3 provides some insights into how the climate responds differently to CO₂ and solar forcings, but more work is necessary to better understand this question. The sums of the radiative adjustments in G1 (gray bars of Figure 3.12) are about 2 W m⁻² larger than the difference between effective and instantaneous forcing in abrupt4xCO₂ (e.g. Table 1 of *Zhang and Huang, 2014*). This must be due to some combination of the solar forcing enhancing or imperfectly canceling CO₂-induced radiative adjustments that warm the planet (such as the stratospheric cooling), and the solar forcing overcompensating for adjustments that cool the planet (such as the tropospheric lapse rate adjustment). Beyond showing the stratospheric adjustment from abrupt4xCO₂ in Figure 3.12, separating the contributions of the CO₂ and solar forcings to the radiative adjustments in G1 would be nontrivial. Regressing the APRP- and kernel-derived radiative responses in the abrupt4xCO₂ experiment against global mean temperature change to obtain the rapid adjustments to the CO₂ quadrupling would run into issues with accuracy due to nonlinearity of feedbacks with temperature increases that would skew the location of the intercept (*Armour et al., 2013*), so an analysis of GCM runs with increased CO₂ and fixed SSTs would be necessary. Furthermore, it may not be the case that the rapid adjustments to the two forcings add together linearly. While some variables, such as global mean

temperature, respond linearly to different combinations of CO₂ and solar forcings (*Kravitz et al.*, 2015b), other aspects of the climate system are inherently nonlinear. LW emission goes with the fourth power of temperature, and specific humidity rises exponentially with temperature, a relationship that affects atmospheric energy transport and the meridional temperature gradient, as explored in Chapter 2 and by *Hwang et al.* (2011). The interactions between the exponential dependence of specific humidity and the 4th power dependence of LW emission on temperature may affect the extent to which the water vapor and tropospheric temperature adjustments compensate for each other, as they seem to roughly cancel in G1 but the water vapor feedback exceeds the lapse rate feedback in global warming simulations (*Soden and Held*, 2006; *Soden et al.*, 2008; *Vial et al.*, 2013). The water vapor and lapse rate adjustments are dependent on the pattern of tropical cooling and polar warming which might not occur if a latitudinal distribution of solar reflection was targeted to cool the poles more (*Ban-Weiss and Caldeira*, 2010; *Kravitz et al.*, 2016).

It would be very interesting to study how cloud rapid adjustments and feedbacks differ under solar versus CO₂ forcing in a model intercomparison framework. The cloud fraction changes in G1 imply that rapid cloud responses to CO₂ and solar forcings are different, but this requires further study with GCM runs that perturb only the solar constant and not CO₂. Since the global mean temperature does not change, the G1 experiment tells us very little about cloud feedbacks, which are temperature dependent. Some studies have included solar-only GCM runs (e.g. *Wetherald and Manabe*, 1975; *Lambert and Faull*, 2007; *Bala et al.*, 2008; *Schaller et al.*, 2013, 2014; *Cao et al.*, 2015; *Modak et al.*, 2016), but these have included only one or two models, and while some, such as *Modak et al.* (2016), have looked at cloud radiative effects and cloud fraction, none have used methods that account for cloud masking to isolate the radiative effects of physical cloud changes. There is no solar equivalent of abrupt4xCO₂ in CMIP5 or any of its associated projects; the closest analogue is probably the aerosol-forcing-only historical runs from the CMIP5 “historicalMisc” collection, analyzed, e.g., by *Salzmann* (2016). The Precipitation Driver and Response Model Intercomparison Project (*Myhre et al.*, 2017) includes a solar constant increase experiment and may be a good avenue to explore cloud changes under

solar forcings.

An attempt was made by *Huneeus et al.* (2014) to study cloud rapid adjustments and feedbacks under solar forcings by subtracting the G1 experiment from the abrupt4xCO₂ experiment. Since these two runs differ only in the solar constant, the difference between these runs can be construed as a representation of a strong, abrupt, positive solar forcing, albeit in a world in which CO₂ is at quadruple its preindustrial value. *Huneeus et al.* calculated effective radiative forcings and feedback parameters in the SW and LW in clear- and cloudy-sky conditions for abrupt4xCO₂ - piControl (the “4xCO₂” case) and for abrupt4xCO₂ - G1 (the “solar” case) using regressions of TOA fluxes against changes in global mean surface temperature. Since this method does not account for cloud masking effects when studying cloud feedbacks, I decided to try to get a better estimate of SW cloud rapid adjustments and feedbacks under solar versus CO₂ forcings, as well as those associated with surface albedo and non-cloud atmospheric changes, using APRP. This was originally going to be a short thesis chapter, but it did not work for the reasons discussed below.

I ran APRP for the model output in each year of abrupt4xCO₂, rather than for a 40-year mean, and then regressed the cloud, non-cloud atmosphere and surface albedo radiative adjustments in each year onto the global mean surface temperature change versus the piControl or G1 baselines. When I made scatter plots (not shown) of the yearly APRP results against the global mean surface temperature change, I found that they were exactly the same in the 4xCO₂ and solar cases, except for horizontal and vertical offsets. In retrospect, this was an obvious result of subtracting different baselines from the same perturbation run (abrupt4xCO₂). I would have gotten slightly different slopes for the 4xCO₂ and solar cases if I had taken a year-by-year temperature difference instead of taking the difference between the abrupt4xCO₂ temperature and a 40-year mean from piControl or G1, but since both piControl and G1 have no global mean temperature change by design, any differences would have been due to statistical noise. This casts doubt on the conclusion by *Huneeus et al.* that, while rapid adjustments differ, temperature-dependent feedbacks are nearly identical for solar versus CO₂ forcings. That conclusion is an artifact of trying to use abrupt4xCO₂ minus G1 as a representation of a solar

forcing. This implies that we will not really be able to say anything about rapid adjustments and feedbacks under solar forcings without GCM runs that actually impose an abrupt change in the solar constant by itself. I hope in the future to be able to study these issues in a model intercomparison project that includes a solar-forcing-only run.

5.2 Implications for the possibility of solar geoengineering

If we were thinking about actually doing solar geoengineering, using Equation 3.3 to predict the necessary solar reflection would be hampered by the fact that we would not know the radiative responses to the intervention *a priori*. Estimates of these adjustments from models would be subject to uncertainty (note the inter-model spread of 2 W m^{-2} in the gray bars of Figure 3.11), and various aspects of the current anthropogenic radiative forcing, particularly aerosol forcing, also have large uncertainty (*Myhre et al.*, 2013). If solar geoengineering was to be done using stratospheric aerosols, then an additional layer of uncertainty regarding microphysical and chemical effects would impact the amount of aerosol injection required to achieve the desired forcing, as summarized by *Visioni et al.* (2017). Observing the climate response to a smaller-scale geoengineering test that would impose a measurable change in the global mean radiation balance (e.g. *Keith et al.*, 2014) would be necessary to constrain these uncertainties.

Such a test would pose ethical questions similar to those for a full deployment, issues explored in an interdisciplinary paper by *Lenferna et al.* (2017). My work on this paper mainly consisted of reviewing the scientific literature related to geoengineering tests, and creating schematics illustrating different types of tests. To summarize what different types of tests might look like, there would be small-scale process studies which would attempt to study issues like aerosol injection and dispersal without actually changing the climate; an example is the planned SCOPEX experiment (*Dykema et al.*, 2014). There are also larger tests that would impose a measurable change in Earth's climate, which in the paper we broke down into albedo response tests (ARTs) and climate response tests (CRTs). ARTs would attempt to measurably affect Earth's albedo, while CRTs would affect global mean or regional temperature or precipitation. For stratospheric aerosol injection, an ART or CRT would involve a shorter-duration, lower-radiative-forcing re-

gional or global injection compared to deployment. *MacMynowski et al.* (2011) suggest that the necessary scale of a CRT could be shrunk by imposing a sinusoidally varying forcing with a period of some integer number of years and then analyzing the results using spectral methods, but the feasibility of actually imposing such a forcing using aerosols has yet to be demonstrated in models, and would be difficult given the seasonal asymmetries and complexity of the stratospheric circulation. By some metrics such as area coverage, particularly for stratospheric aerosol injection where it would be impossible to keep the injected particles confined to a limited area, a CRT or ART would be indistinguishable from a full deployment. However, the test would need to be much smaller in terms of radiative forcing and much shorter in duration than a deployment to be relevant for planning a deployment. Tests intended to measure regional-scale changes in temperature and precipitation would take too long to pass this criterion, even using the spectral methods suggested by *MacMynowski et al.* (2011).

While regional impacts would be impossible to measure from a relevant test, they are still possible; the ITCZ shifts explored in Chapter 2 suggest that even a test with a hemispherically symmetric structure (such as space mirrors) could cause changes in regional precipitation that would create “winners and losers” in terms of rainfall. The extent to which inducing a change that could not be measured would raise ethical questions tended to divide the scientists and philosophers when writing the paper. The specific ethical issues related to ARTs and CRTs were examined in depth by UW philosophy grad student Alex Lenferna, and the question of how much confidence about the risk of undesirable regional impacts would be needed to allow a test to proceed is one such issue. Other questions examined in the paper relate to issues of distributive justice, informed consent, compensation, whether subjecting the planet to an experiment displays hubris, and whether the difference in intent between a test and a deployment is morally relevant.

The fact that the required solar amount of solar geoengineering depends on rapid responses to the solar forcing reinforces that a CRT, or at least an ART, which would be needed to measure these rapid responses, would likely be necessary before deploying solar geoengineering. If such a test could not be ethically justified, then we could not even think about deployment. On the

other hand, the fact that the required solar forcing to compensate a given CO₂ increase seems to depend on rapid adjustments and not temperature-dependent feedbacks suggests that the test need not be very long, only enough to measure the forcing and the rapid radiative responses from satellites, which the study of *Seidel et al.* (2014) suggests could be done within a few years. An alternative to having a separate test would be to actively control the global mean temperature by adjusting the amount of solar reflection every year in response to observations (*Kravitz et al.*, 2014). This approach would still raise ethical questions because it would involve subjecting the planet to a large-scale experiment without first defining exactly how large the experiment would be.

If solar geoengineering was attempting to actually cool the planet instead of simply preventing future warming under increasing CO₂, then temperature-dependent feedbacks on the solar forcing, which are not captured by the G1 experiment, would occur. Assuming that these feedbacks operated at the same strength during the cooling period as they did during the CO₂-induced warming period, it might be possible make a decent guess as to the required amount of geoengineering using the theory described in Chapter 3 and scaling down from a CO₂ quadrupling based on the amount of CO₂ added since the Earth was last at the desired baseline temperature. However, time-dependent effects arising from the inertia of ocean temperature changes would be a confounding factor that would add to the uncertainty regarding the required amount of solar reduction. Analysis of other GeoMIP experiments, such as G4, that impose a global mean temperature change from the solar forcing, could help illustrate these issues.

Besides their effects on the required solar forcing, the changes in atmospheric physical properties that occur in G1 are interesting in their own right, and may have policy implications if they translated to a real geoengineering deployment. If low cloud fraction were actually reduced by solar geoengineering, it could result in increased solar energy production, and could enhance vegetation growth in sunlight-limited regimes like the Amazon (*Nemani et al.*, 2003). On the other hand, a reduction in low clouds over the ocean would make it more difficult to do marine cloud brightening at the same time as other forms of solar geoengineering. Changes

in cirrus clouds are also relevant in the context of research on the effects of sedimentation of injected stratospheric aerosols on high clouds (*Kuebbeler et al.*, 2012; *Visioni et al.*, 2018) and proposals to intentionally thin cirrus clouds with nucleation-inducing aerosols in order to cool the earth by increased LW emission (*Mitchell and Finnegan*, 2009). The increase in high clouds in most models in G1 indicates that thermodynamic and radiative adjustments to the forcing scenario can have effects on high clouds that may counteract unintentional or intentional microphysical effects. My analysis of G1 also suggests that stratospheric ozone could be affected by changes in stratospheric water vapor resulting from TTL temperature changes. In model runs with actual injection of sulfate aerosols, LW absorption of these particles warms the tropical tropopause and increases stratospheric water vapor, which results in decreased ozone concentrations (*Heckendorn et al.*, 2009). *Keith et al.* (2016) suggest that this risk could be mitigated by instead injecting calcite aerosols, which would absorb much less LW radiation than sulfates, but the inconsistency between models in stratospheric water vapor responses to the G1 experiment, which includes no aerosol injection in G1, shows that much uncertainty remains in this area. Taken together, these issues emphasize the importance of continuing to perform and analyze geoengineering simulations, both in highly idealized scenarios like G1 and more realistic ones like G4 or G4SSA, in order to better understand the climate responses to geoengineering schemes and the different roles played by thermodynamics, radiation, microphysics and chemistry in these responses.

BIBLIOGRAPHY

- Alexeev, V. A., P. L. Langen, and J. R. Bates (2005), Polar amplification of surface warming on an aquaplanet in “ghost forcing” experiments without sea ice feedbacks, *Climate Dynamics*, 24(7), 655–666, doi:10.1007/s00382-005-0018-3.
- Andrews, T., and P. M. Forster (2010), The transient response of global-mean precipitation to increasing carbon dioxide levels, *Environmental Research Letters*, 5, 025212.
- Aquila, V., C. I. Garfinkel, P. Newman, L. Oman, and D. Waugh (2014), Modifications of the quasi-biennial oscillation by a geoengineering perturbation of the stratospheric aerosol layer, *Geophysical Research Letters*, 41(5), 1738–1744, doi:10.1002/2013GL058818.
- Armour, K. C., C. M. Bitz, and G. H. Roe (2013), Time-varying climate sensitivity from regional feedbacks, *Journal of Climate*, 26, 4518–4534, doi:10.1175/JCLI-D-12-00544.1.
- Arora, V. K., J. F. Scinocca, G. J. Boer, J. R. Christian, K. L. Denman, G. M. Flato, V. V. Kharin, W. G. Lee, and W. J. Merryfield (2011), Carbon emission limits required to satisfy future representative concentration pathways of greenhouse gases, *Geophysical Research Letters*, 38(5), L05805, doi:10.1029/2010GL046270.
- Bala, G., P. Duffy, and K. Taylor (2008), Impact of geoengineering schemes on the global hydrological cycle, *Proceedings of the National Academy of Sciences*, 105(22), 7664–7669.
- Ban-Weiss, G., and K. Caldeira (2010), Geoengineering as an optimization problem, *Environmental Research Letters*, 5, 034009, doi:10.1088/1748-9326/5/3/034009.
- Bekryaev, R. V., I. V. Polyakov, and V. A. Alexeev (2010), Role of polar amplification in long-term surface air temperature variations and modern arctic warming, *Journal of Climate*, 23(14), 3888–3906, doi:10.1175/2010JCLI3297.1.

- Bentsen, M., et al. (2013), The Norwegian Earth System Model, NorESM1-M – Part 1: Description and basic evaluation of the physical climate, *Geoscientific Model Development*, 6(3), 687–720, doi:10.5194/gmd-6-687-2013.
- Bewick, R., J. Sanchez, and C. McInnes (2012), The feasibility of using an L1 positioned dust cloud as a method of space-based geoengineering, *Advances in Space Research*, 49(7), 1212 – 1228, doi:10.1016/j.asr.2012.01.010.
- Biasutti, M., and A. H. Sobel (2009), Delayed Sahel rainfall and global seasonal cycle in a warmer climate, *Geophysical Research Letters*, 36(23), L23707, doi:10.1029/2009GL041303.
- Bischoff, T., and T. Schneider (2014), Energetic constraints on the position of the intertropical convergence zone, *Journal of Climate*, 27(13), 4937–4951, doi:10.1175/JCLI-D-13-00650.1.
- Block, K., and T. Mauritsen (2013), Forcing and feedback in the MPI-ESM-LR coupled model under abruptly quadrupled CO₂, *Journal of Advances in Modeling Earth Systems*, 5(4), 676–691, doi:10.1002/jame.20041.
- Bodas-Salcedo, A., et al. (2011), COSP: Satellite simulation software for model assessment, *Bulletin of the American Meteorological Society*, 92(8), 1023–1043, doi:10.1175/2011BAMS2856.1.
- Bolton, D. (1980), The computation of equivalent potential temperature, *Monthly Weather Review*, 108, 1046–1053.
- Bony, S., M. Webb, C. Bretherton, S. Klein, P. Siebesma, G. Tselioudis, and M. Zhang (2011), CFMIP: Towards a better evaluation and understanding of clouds and cloud feedbacks in CMIP5 models, *CLIVAR Exchanges*, 56, 20–24.
- Bretherton, C. S. (2015), Insights into low-latitude cloud feedbacks from high-resolution models, *Philosophical Transactions of the Royal Society of London A: Mathematical, Physical and Engineering Sciences*, 373(2054), doi:10.1098/rsta.2014.0415.

- Brewer, A. (1949), Evidence for a world circulation provided by the measurement of helium and water vapour distribution in the stratosphere, *Quarterly Journal of the Royal Meteorological Society*, 75, 351–363.
- Broccoli, A. J., K. A. Dahl, and R. J. Stouffer (2006), Response of the ITCZ to northern hemisphere cooling, *Geophysical Research Letters*, 33(1), L01702, doi:10.1029/2005GL024546.
- Cao, L., G. Bala, K. Caldeira, R. Nemani, and G. Ban-Weiss (2010), Importance of carbon dioxide physiological forcing to future climate change, *Proceedings of the National Academy of Sciences*, 107(21), 9513–9518.
- Cao, L., G. Bala, M. Zheng, and K. Caldeira (2015), Fast and slow climate responses to CO₂ and solar forcing: A linear multivariate regression model characterizing transient climate change, *Journal of Geophysical Research: Atmospheres*, 120(23), 12,037–12,053, doi: 10.1002/2015JD023901, 2015JD023901.
- Chiang, J. C. H., and C. M. Bitz (2005), Influence of high latitude ice cover on the marine intertropical convergence zone, *Climate Dynamics*, 25(5), 477–496, doi:10.1007/s00382-005-0040-5.
- Chung, E.-S., and B. J. Soden (2015), An assessment of methods for computing radiative forcing in climate models, *Environmental Research Letters*, 10, 074004, doi:10.1088/1748-9326/10/7/074004.
- Collins, W. J., et al. (2011), Development and evaluation of an Earth-System model - HadGEM2, *Geoscientific Model Development*, 4(4), 1051–1075, doi:10.5194/gmd-4-1051-2011.
- Crutzen, P. J. (2006), Albedo enhancement by stratospheric sulfur injections: A contribution to resolve a policy dilemma?, *Climatic Change*, 77(3), 211–220, doi:10.1007/s10584-006-9101-y.
- Dong, B., J. M. Gregory, and R. Sutton (2009), Understanding land-sea warming contrast in response to increasing greenhouse gases. Part I: Transient adjustment, *Journal of Climate*, 22, 3079–3097.

Donohoe, A., and D. S. Battisti (2013), The seasonal cycle of atmospheric heating and temperature, *Journal of Climate*, 26(14), 4962–4980, doi:10.1175/JCLI-D-12-00713.1.

Donohoe, A., J. Marshall, D. Ferreira, and D. Mcgee (2013), The relationship between ITCZ location and cross-equatorial atmospheric heat transport: From the seasonal cycle to the last glacial maximum, *Journal of Climate*, 26(11), 3597–3618, doi:10.1175/JCLI-D-12-00467.1.

Dufresne, J.-L., et al. (2013), Climate change projections using the IPSL-CM5 Earth System Model: from CMIP3 to CMIP5, *Climate Dynamics*, 40(9), 2123–2165, doi:10.1007/s00382-012-1636-1.

Dwyer, J. G., M. Biasutti, and A. H. Sobel (2014), The effect of greenhouse gas-induced changes in SST on the annual cycle of zonal mean tropical precipitation, *Journal of Climate*, 27(12), 4544–4565, doi:10.1175/JCLI-D-13-00216.1.

Dykema, J. A., D. W. Keith, J. G. Anderson, and D. Weisenstein (2014), Stratospheric controlled perturbation experiment: a small-scale experiment to improve understanding of the risks of solar geoengineering, *Philosophical Transactions of the Royal Society of London A: Mathematical, Physical and Engineering Sciences*, 372(2031), doi:10.1098/rsta.2014.0059.

Feldl, N., S. Bordoni, and T. M. Merlis (2017), Coupled high-latitude climate feedbacks and their impact on atmospheric heat transport, *Journal of Climate*, 30(1), 189–201, doi:10.1175/JCLI-D-16-0324.1.

Ferraro, A. J., and H. G. Griffiths (2016), Quantifying the temperature-independent effect of stratospheric aerosol geoengineering on global-mean precipitation in a multi-model ensemble, *Environmental Research Letters*, 11(3), 034012.

Feulner, G. (2012), The faint young sun problem, *Reviews of Geophysics*, 50, RG2006, doi: 10.1029/2011RG000375.

- Field, C. B., R. B. Jackson, and H. A. Mooney (1995), Stomatal responses to increased CO₂: implications from the plant to the global scale, *Plant, Cell & Environment*, 18(10), 1214–1225, doi:10.1111/j.1365-3040.1995.tb00630.x.
- Frierson, D. M. W., and Y.-T. Hwang (2012), Extratropical influence on ITCZ shifts in slab ocean simulations of global warming, *Journal of Climate*, 25(2), 720–733, doi:10.1175/JCLI-D-11-00116.1.
- Fueglistaler, S., A. E. Dessler, T. J. Dunkerton, I. Folkins, Q. Fu, and P. W. Mote (2009), Tropical tropopause layer, *Reviews of Geophysics*, 47, RG1004.
- Gent, P. R., et al. (2011), The Community Climate System Model Version 4, *Journal of Climate*, 24(19), 4973–4991, doi:10.1175/2011JCLI4083.1.
- Giorgetta, M. A., et al. (2013), Climate and carbon cycle changes from 1850 to 2100 in MPI-ESM simulations for the Coupled Model Intercomparison Project phase 5, *Journal of Advances in Modeling Earth Systems*, 5(3), 572–597, doi:10.1002/jame.20038.
- Gordon, C., C. Cooper, C. A. Senior, H. Banks, J. M. Gregory, T. C. Johns, J. F. B. Mitchell, and R. A. Wood (2000), The simulation of SST, sea ice extents and ocean heat transports in a version of the Hadley Centre coupled model without flux adjustments, *Climate Dynamics*, 16(2), 147–168, doi:10.1007/s003820050010.
- Govindasamy, B., and K. Caldeira (2000), Geoengineering Earth's radiation balance to mitigate CO₂-induced climate change, *Geophysical Research Letters*, 27(14), 2141–2144, doi:10.1029/1999GL006086.
- Govindasamy, B., K. Caldeira, and P. Duffy (2003), Geoengineering earth's radiation balance to mitigate climate change from a quadrupling of CO₂, *Global and Planetary Change*, 37(1-2), 157 – 168, doi:10.1016/S0921-8181(02)00195-9.
- Graversen, R. G., and M. Wang (2009), Polar amplification in a coupled climate model with locked albedo, *Climate Dynamics*, 33(5), 629–643, doi:10.1007/s00382-009-0535-6.

Green, B., and J. Marshall (2017), Coupling of trade winds with ocean circulation damps ITCZ shifts, *Journal of Climate*, 30(12), 4395–4411, doi:10.1175/JCLI-D-16-0818.1.

Gregory, J., and M. Webb (2008), Tropospheric adjustment induces a cloud component in CO₂ forcing, *Journal of Climate*, 21(1), 58–71, doi:10.1175/2007JCLI1834.1.

Gregory, J. M., W. J. Ingram, M. A. Palmer, G. S. Jones, P. A. Stott, R. B. Thorpe, J. A. Lowe, T. C. Johns, and K. D. Williams (2004), A new method for diagnosing radiative forcing and climate sensitivity, *Geophysical Research Letters*, 31(3), L03205, doi:10.1029/2003GL018747.

Guo, A., J. C. Moore, and D. Ji (2018), Tropical atmospheric circulation response to the G1 sunshade geoengineering radiative forcing experiment, *Atmospheric Chemistry and Physics Discussions*, 2018, 1–53, doi:10.5194/acp-2018-141.

Hartmann, D. L. (2016), *Global Physical Climatology*, 2nd ed., Elsevier, Amsterdam, Netherlands.

Hawcroft, M., J. M. Haywood, M. Collins, A. Jones, A. C. Jones, and G. Stephens (2017), Southern Ocean albedo, inter-hemispheric energy transports and the double ITCZ: global impacts of biases in a coupled model, *Climate Dynamics*, 48(7), 2279–2295, doi:10.1007/s00382-016-3205-5.

Haywood, J. M., A. Jones, N. Bellouin, and D. Stephenson (2013), Asymmetric forcing from stratospheric aerosols impacts Sahelian rainfall, *Nature Climate Change*, 3, 660–665, doi:10.1038/NCLIMATE1857.

Haywood, J. M., et al. (2016), The impact of equilibrating hemispheric albedos on tropical performance in the HadGEM2-ES coupled climate model, *Geophysical Research Letters*, 43(1), 395–403, doi:10.1002/2015GL066903, 2015GL066903.

Hazeleger, W., et al. (2012), EC-Earth V2.2: description and validation of a new seamless earth system prediction model, *Climate Dynamics*, 39(11), 2611–2629, doi:10.1007/s00382-011-1228-5.

- Heckendorn, P., D. Weisenstein, S. Fueglistaler, B. P. Luo, E. Rozanov, M. Schraner, L. W. Thomason, and T. Peter (2009), The impact of geoengineering aerosols on stratospheric temperature and ozone, *Environmental Research Letters*, 4(4), 045,108, doi:10.1088/1748-9326/4/4/045108.
- Held, I. M., and B. J. Soden (2006), Robust responses of the hydrological cycle to global warming, *Journal of Climate*, 19, 5686–5699.
- Holland, M. M., and C. M. Bitz (2003), Polar amplification of climate change in coupled models, *Climate Dynamics*, 21(3), 221–232, doi:10.1007/s00382-003-0332-6.
- Hong, Y., J. C. Moore, S. Jevrejeva, D. Ji, S. J. Phipps, A. Lenton, S. Tilmes, S. Watanabe, and L. Zhao (2017), Impact of the GeoMIP G1 sunshade geoengineering experiment on the Atlantic meridional overturning circulation, *Environmental Research Letters*, 12, 034009, doi: 10.1088/1748-9326/aa5fb8.
- Huang, Y., and M. Zhang (2014), The implication of radiative forcing and feedback for meridional energy transport, *Geophysical Research Letters*, 41(5), 1665–1672, doi: 10.1002/2013GL059079.
- Huneeus, N., et al. (2014), Forcings and feedbacks in the GeoMIP ensemble for a reduction in solar irradiance and increase in CO₂, *Journal of Geophysical Research: Atmospheres*, 119(9), 5226–5239, doi:10.1002/2013JD021110.
- Hurrell, J. W., et al. (2013), The Community Earth System Model: A framework for collaborative research, *Bulletin of the American Meteorological Society*, 94(9), 1339–1360, doi: 10.1175/BAMS-D-12-00121.1.
- Hwang, Y.-T., and D. M. W. Frierson (2010), Increasing atmospheric poleward energy transport with global warming, *Geophysical Research Letters*, 37(24), L24807, doi: 10.1029/2010GL045440.

Hwang, Y.-T., D. M. W. Frierson, and J. E. Kay (2011), Coupling between Arctic feedbacks and changes in poleward energy transport, *Geophysical Research Letters*, 38(17), L17704, doi: 10.1029/2011GL048546.

Hwang, Y.-T., D. M. W. Frierson, and S. M. Kang (2013), Anthropogenic sulfate aerosol and the southward shift of tropical precipitation in the late 20th century, *Geophysical Research Letters*, 40(11), 2845–2850, doi:10.1002/grl.50502.

IPCC (2013), *Climate Change 2013: The Physical Science Basis. Contribution of Working Group I to the Fifth Assessment Report of the Intergovernmental Panel on Climate Change*, 1535 pp., Cambridge University Press, Cambridge, United Kingdom and New York, NY, USA, doi: 10.1017/CBO9781107415324.

Irvine, P. J., A. Ridgwell, and D. J. Lunt (2010), Assessing the regional disparities in geoengineering impacts, *Geophysical Research Letters*, 37(18), L18702, doi:10.1029/2010GL044447.

Ji, D., et al. (2014), Description and basic evaluation of Beijing Normal University Earth System Model (BNU-ESM) version 1, *Geoscientific Model Development*, 7(5), 2039–2064, doi: 10.5194/gmd-7-2039-2014.

Jones, A., et al. (2013), The impact of abrupt suspension of solar radiation management (termination effect) in experiment G2 of the Geoengineering Model Intercomparison Project (GeoMIP), *Journal of Geophysical Research: Atmospheres*, 118(17), 9743–9752, doi: 10.1002/jgrd.50762.

Kang, S. M., I. M. Held, D. M. W. Frierson, and M. Zhao (2008), The response of the ITCZ to extra-tropical thermal forcing: Idealized slab-ocean experiments with a GCM, *Journal of Climate*, 21(14), 3521–3532, doi:10.1175/2007JCLI2146.1.

Kay, J. E., C. Wall, V. Yettella, B. Medeiros, C. Hannay, P. Caldwell, and C. Bitz (2016), Global climate impacts of fixing the southern ocean shortwave radiation bias in the Community Earth System model (CESM), *Journal of Climate*, 29(12), 4617–4636, doi:10.1175/JCLI-D-15-0358.1.

Keith, D. (2013), *A Case for Climate Engineering*, The MIT Press, Cambridge, Massachusetts.

Keith, D. W., and H. Dowlatabadi (1992), A serious look at geoengineering, *Eos, Transactions American Geophysical Union*, 73(27), 289–293, doi:10.1029/91EO00231.

Keith, D. W., R. Duren, and D. G. MacMartin (2014), Field experiments on solar geoengineering: report of a workshop exploring a representative research portfolio, *Philosophical Transactions of the Royal Society A*, 372, 20140,175, doi:10.1098/rsta.2014.0175.

Keith, D. W., D. K. Weisenstein, J. A. Dykema, and F. N. Keutsch (2016), Stratospheric solar geoengineering without ozone loss, *Proceedings of the National Academy of Sciences*, 113(52), 14,910–14,914, doi:10.1073/pnas.1615572113.

Klein, S. A., and D. L. Hartmann (1993), The seasonal cycle of low stratiform clouds, *Journal of Climate*, 6, 1587–1606.

Klein, S. A., and C. Jakob (1999), Validation and sensitivities of frontal clouds simulated by the ECMWF model, *Monthly Weather Review*, 127(10), 2514–2531, doi:10.1175/1520-0493(1999)127<2514:VASOFC>2.0.CO;2.

Kravitz, B., A. Robock, O. Boucher, H. Schmidt, K. E. Taylor, G. Stenchikov, and M. Schulz (2011a), The Geoengineering Model Intercomparison Project (GeoMIP), *Atmospheric Science Letters*, 12(2), 162–167, doi:10.1002/asl.316.

Kravitz, B., A. Robock, O. Boucher, H. Schmidt, and K. E. Taylor (2011b), Specifications for GeoMIP experiments G1 through G4, URL: http://climate.envsci.rutgers.edu/GeoMIP/docs/specificationsG1_G4_v1.0.pdf [Accessed March 2015], Version 1.0.

Kravitz, B., et al. (2013a), Climate model response from the Geoengineering Model Intercomparison Project (GeoMIP), *Journal of Geophysical Research: Atmospheres*, 118(15), 8320–8332, doi:10.1002/jgrd.50646.

Kravitz, B., et al. (2013b), Sea spray geoengineering experiments in the geoengineering model intercomparison project (GeoMIP): Experimental design and preliminary results, *Journal of Geophysical Research: Atmospheres*, 118(19), 11,175–11,186, doi:10.1002/jgrd.50856, 2013JD020351.

Kravitz, B., et al. (2013c), An energetic perspective on hydrological cycle changes in the Geoengineering Model Intercomparison Project, *Journal of Geophysical Research: Atmospheres*, 118(23), 13,087–13,102, doi:10.1002/2013JD020502, 2013JD020502.

Kravitz, B., D. G. MacMartin, D. T. Leedal, P. J. Rasch, and A. J. Jarvis (2014), Explicit feedback and the management of uncertainty in meeting climate objectives with solar geoengineering, *Environmental Research Letters*, 9(4), 044,006, doi:10.1088/1748-9326/9/4/044006.

Kravitz, B., et al. (2015a), The Geoengineering Model Intercomparison Project Phase 6 (GeoMIP6): simulation design and preliminary results, *Geoscientific Model Development*, 8(10), 3379–3392, doi:10.5194/gmd-8-3379-2015.

Kravitz, B., D. G. MacMartin, P. J. Rasch, and A. J. Jarvis (2015b), A new method of comparing forcing agents in climate models, *Journal of Climate*, 28(20), 8203–8218, doi:10.1175/JCLI-D-14-00663.1.

Kravitz, B., D. MacMartin, H. Wang, and P. Rasch (2016), Geoengineering as a design problem, *Earth System Dynamics*, 7, 469–497, doi:10.5194/esd-7-469-2016.

Kuebbeler, M., U. Lohmann, and J. Feichter (2012), Effects of stratospheric sulfate aerosol geo-engineering on cirrus clouds, *Geophysical Research Letters*, 39, L23803, doi: 10.1029/2012GL053797.

Laguë, M. M., and A. L. S. Swann (2016), Progressive midlatitude afforestation: Impacts on clouds, global energy transport, and precipitation, *Journal of Climate*, 29(15), 5561–5573, doi: 10.1175/JCLI-D-15-0748.1.

Lamb, D., and J. Verlinde (2011), *Physics and Chemistry of Clouds*, 584 pp., Cambridge University Press, Cambridge, UK.

Lambert, F. H., and N. E. Faull (2007), Tropospheric adjustment: The response of two general circulation models to a change in insolation, *Geophysical Research Letters*, 34(3), L03701, doi: 10.1029/2006GL028124.

Latham, J., et al. (2012), Marine cloud brightening, *Philosophical Transactions of the Royal Society A*, 370(1974), 4217–4262, doi:10.1098/rsta.2012.0086.

Lenferna, G. A., R. D. Russotto, A. Tan, S. M. Gardiner, and T. P. Ackerman (2017), Relevant climate response tests for stratospheric aerosol injection: A combined ethical and scientific analysis, *Earth's Future*, 5(6), 577–591, doi:10.1002/2016EF000504.

MacMartin, D. G., K. Caldeira, and D. W. Keith (2014), Solar geoengineering to limit the rate of temperature change, *Philosophical Transactions of the Royal Society A*, 372, 20140,134.

MacMynowski, D. G., D. W. Keith, K. Caldeira, and H.-J. Shin (2011), Can we test geoengineering?, *Energy Environ. Sci.*, 4, 5044–5052, doi:10.1039/C1EE01256H.

Manabe, S., and R. T. Wetherald (1975), The effects of doubling the CO₂ concentration on the climate of a general circulation model, *Journal of the Atmospheric Sciences*, 32(1), 3–15, doi: 10.1175/1520-0469(1975)032<0003:TEODTC>2.0.CO;2.

McCusker, K. E., K. C. Armour, C. M. Bitz, and D. S. Battisti (2014), Rapid and extensive warming following cessation of solar radiation management, *Environmental Research Letters*, 9(2), 024005.

Merlis, T. M. (2014), Interacting components of the top-of-atmosphere energy balance affect changes in regional surface temperature, *Geophysical Research Letters*, 41(20), 7291–7297, doi:10.1002/2014GL061700.

Merlis, T. M. (2015), Direct weakening of tropical circulations from masked CO₂ radiative forcing, *Proceedings of the National Academy of Sciences*, 112(43), 13,167–13,171, doi: 10.1073/pnas.1508268112.

Mitchell, D. L., and W. Finnegan (2009), Modification of cirrus clouds to reduce global warming, *Environmental Research Letters*, 4, 045102, doi:10.1088/1748-9326/4/4/045102.

Mitchell, J. F. B. (1983), The seasonal response of a general circulation model to changes in CO₂ and sea temperatures, *Quarterly Journal of the Royal Meteorological Society*, 109, 113–152.

Modak, A., G. Bala, L. Cao, and K. Caldeira (2016), Why must a solar forcing be larger than a CO₂ forcing to cause the same global mean surface temperature change?, *Environmental Research Letters*, 11, 044013.

Myhre, G., et al. (2013), Anthropogenic and natural radiative forcing, in *Climate Change 2013: The Physical Science Basis. Contribution of Working Group I to the Fifth Assessment Report of the Intergovernmental Panel on Climate Change*, edited by T. Stocker, D. Qin, G.-K. Plattner, M. Tignor, S. Allen, J. Boschung, A. Nauels, Y. Xia, V. Bex, and P. Midgley, chap. 8, pp. 659–740, Cambridge University Press, Cambridge, United Kingdom and New York, NY, USA, doi: 10.1017/CBO9781107415324.018.

Myhre, G., et al. (2017), Pdrmip: A precipitation driver and response model intercomparison project – protocol and preliminary results, *Bulletin of the American Meteorological Society*, 98(6), 1185–1198, doi:10.1175/BAMS-D-16-0019.1.

Nemani, R. R., C. D. Keeling, H. Hashimoto, W. M. Jolly, S. C. Piper, C. J. Tucker, R. B. Myneni, and S. W. Running (2003), Climate-driven increases in global terrestrial net primary production from 1982 to 1999, *Science*, 300(5625), 1560–1563, doi:10.1126/science.1082750.

Newell, R. E., and S. Gould-Stewart (1981), A stratospheric fountain?, *Journal of the Atmospheric Sciences*, 38, 2789–2796.

Niemeier, U., H. Schmidt, K. Alterskjær, and J. E. Kristjánsson (2013), Solar irradiance reduction via climate engineering: Impact of different techniques on the energy balance and the hydrological cycle, *Journal of Geophysical Research: Atmospheres*, 118(21), 11,905–11,917, doi: 10.1002/2013JD020445.

NOAA (1976), *U.S. Standard Atmosphere: 1976*, National Oceanographic and Atmospheric Administration, Washington, DC, NOAA-S/T 76-1562.

North, G. R. (1975), Theory of energy-balance climate models, *Journal of the Atmospheric Sciences*, 32(11), 2033–2043.

Pendergrass, A. G., and D. L. Hartmann (2014), The atmospheric energy constraint on global-mean precipitaton change, *Journal of Climate*, 27, 757–768.

Pendergrass, A. G., A. Conley, and F. M. Vitt (2018), Surface and top-of-atmosphere radiative feedback kernels for CESM-CAM5, *Earth System Science Data*, 10(1), 317–324, doi: 10.5194/essd-10-317-2018.

Phipps, S. J., L. D. Rotstain, H. B. Gordon, J. L. Roberts, A. C. Hirst, and W. F. Budd (2011), The CSIRO Mk3L climate system model version 1.0 – Part 1: Description and evaluation, *Geoscientific Model Development*, 4(2), 483–509, doi:10.5194/gmd-4-483-2011.

Pithan, F., and T. Mauritsen (2014), Arctic amplification dominated by temperature feedbacks in contemporary climate models, *Nature Geoscience*, 7, 181–184, doi:10.1038/ngeo2071.

Qu, X., A. Hall, S. Klein, and P. M. Caldwell (2014), On the spread of changes in marine low cloud cover in climate model simulations of the 21st century, *Climate Dynamics*, 42, 2603–2626.

Robock, A. (2008), 20 reasons why geoengineering may be a bad idea, *Bulletin of the Atomic Scientists*, 64(2), 14–18, 59, doi:10.2968/064002006.

Robock, A., L. Oman, and G. Stenchikov (2008), Regional climate responses to geoengineering with tropical and Arctic SO₂ injections, *J. Geophys. Res.*, 113, D16101.

- Rose, B. E. J., and L. Rayborn (2016), The effects of ocean heat uptake on transient climate sensitivity, *Current Climate Change Reports*, 2(4), 190–201, doi:10.1007/s40641-016-0048-4.
- Rose, B. E. J., K. C. Armour, D. S. Battisti, N. Feldl, and D. D. B. Koll (2014), The dependence of transient climate sensitivity and radiative feedbacks on the spatial pattern of ocean heat uptake, *Geophysical Research Letters*, 41(3), 1071–1078, doi:10.1002/2013GL058955.
- Rossow, W. B., and R. A. Schiffer (1999), Advances in understanding clouds from ISCCP, *Bulletin of the American Meteorological Society*, 80(11), 2261–2287, doi:10.1175/1520-0477(1999)080<2261:AIUCFI>2.0.CO;2.
- Russotto, R. D., and T. P. Ackerman (2018a), Energy transport, polar amplification, and ITCZ shifts in the GeoMIP G1 ensemble, *Atmospheric Chemistry and Physics*, 18, 2287–2305, doi:10.5194/acp-18-2287-2018.
- Russotto, R. D., and T. P. Ackerman (2018b), Changes in clouds and thermodynamics under solar geoengineering and implications for required solar reduction, *Atmospheric Chemistry and Physics Discussions*, doi:10.5194/acp-2018-345, in review.
- Salzmann, M. (2016), Global warming without global mean precipitation increase?, *Science Advances*, 2(6), doi:10.1126/sciadv.1501572.
- Santer, B., et al. (2003), Contributions of anthropogenic and natural forcing to recent tropopause height changes, *Science*, 301, 479–483, doi:10.1126/science.1084123.
- Schaller, N., J. Cermak, M. Wild, and R. Knutti (2013), The sensitivity of the modeled energy budget and hydrological cycle to CO₂ and solar forcing, *Earth System Dynamics*, 4, 253–266, doi:10.5194/esd-4-253-2013.
- Schaller, N., J. Sedlacek, and R. Knutti (2014), The asymmetry of the climate system's response to solar forcing changes and its implications for geoengineering scenarios, *Journal of Geophysical Research: Atmospheres*, 119(9), 5171–5184, doi:10.1002/2013JD021258.

Schmidt, G. A., et al. (2014), Configuration and assessment of the GISS ModelE2 contributions to the CMIP5 archive, *Journal of Advances in Modeling Earth Systems*, 6(1), 141–184, doi: 10.1002/2013MS000265.

Schmidt, H., et al. (2012), Solar irradiance reduction to counteract radiative forcing from a quadrupling of CO₂: climate responses simulated by four earth system models, *Earth System Dynamics*, 3(1), 63–78, doi:10.5194/esd-3-63-2012.

Seidel, D. J., G. Feingold, A. R. Jacobson, and N. Loeb (2014), Detection limits of albedo changes induced by climate engineering, *Nature Climate Change*, 4, 93–98, doi: 10.1038/NCLIMATE2076.

Seo, J., S. M. Kang, and T. M. Merlis (2017), A model intercomparison of the tropical precipitation response to a CO₂ doubling in aquaplanet simulations, *Geophysical Research Letters*, 44(2), 993–1000, doi:10.1002/2016GL072347.

Shell, K. M., J. T. Kiehl, and C. A. Shields (2008), Using the radiative kernel technique to calculate climate feedbacks in NCAR's Community Atmospheric Model, *Journal of Climate*, 21(10), 2269–2282, doi:10.1175/2007JCLI2044.1.

Sherwood, S. C., S. Bony, and J.-L. Dufresne (2014), Spread in model climate sensitivity traced to atmospheric convective mixing, *Nature*, 505, 37–42, doi:10.1038/nature12829.

Slingo, J. (1987), The development and verification of a cloud prediction scheme for the ECMWF model, *Quarterly Journal of the Royal Meteorological Society*, 113, 899–927.

Smyth, J. E., R. D. Russotto, and T. Storelvmo (2017), Thermodynamic and dynamic responses of the hydrological cycle to solar dimming, *Atmospheric Chemistry and Physics*, 17(10), 6439–6453, doi:10.5194/acp-17-6439-2017.

Soden, B. J., and I. M. Held (2006), An assessment of climate feedbacks in coupled ocean-atmosphere models, *Journal of Climate*, 19(14), 3354–3360, doi:10.1175/JCLI3799.1.

Soden, B. J., I. M. Held, R. Colman, K. M. Shell, J. T. Kiehl, and C. A. Shields (2008), Quantifying climate feedbacks using radiative kernels, *Journal of Climate*, 21, 3504–3520.

Swann, A. L. S., I. Y. Fung, and J. C. H. Chiang (2012), Mid-latitude afforestation shifts general circulation and tropical precipitation, *Proceedings of the National Academy of Sciences*, 109(3), 712–716, doi:10.1073/pnas.1116706108.

Taylor, K. E., M. Crucifix, P. Braconnot, C. D. Hewitt, C. Doutriaux, A. J. Broccoli, J. F. B. Mitchell, and M. J. Webb (2007), Estimating shortwave radiative forcing and response in climate models, *Journal of Climate*, 20(11), 2530–2543, doi:10.1175/JCLI4143.1.

Taylor, K. E., R. J. Stouffer, and G. A. Meehl (2012), An overview of CMIP5 and the experiment design, *Bulletin of the American Meteorological Society*, 93, 485–198.

Tilmes, S., et al. (2013), The hydrological impact of geoengineering in the Geoengineering Model Intercomparison Project (GeoMIP), *Journal of Geophysical Research: Atmospheres*, 118(19), 11,036–11,058, doi:10.1002/jgrd.50868.

Tilmes, S., M. J. Mills, U. Niemeier, H. Schmidt, A. Robock, B. Kravitz, J.-F. Lamarque, G. Pitari, and J. M. English (2015), A new Geoengineering Model Intercomparison Project (GeoMIP) experiment designed for climate and chemistry models, *Geoscientific Model Development*, 8(1), 43–49, doi:10.5194/gmd-8-43-2015.

Tilmes, S., B. M. Sanderson, and B. C. O'Neill (2016), Climate impacts of geoengineering in a delayed mitigation scenario, *Geophysical Research Letters*, 43(15), 8222–8229, doi:10.1002/2016GL070122.

Vial, J., J.-L. Dufresne, and S. Bony (2013), On the interpretation of inter-model spread in CMIP5 climate sensitivity estimates, *Climate Dynamics*, 41(11-12), 3339–3362, doi:10.1007/s00382-013-1725-9.

Viale, F., and T. M. Merlis (2017), Variations in tropical cyclone frequency response to solar and CO₂ forcing in aquaplanet simulations, *Journal of Advances in Modeling Earth Systems*, 9(1), 4–18, doi:10.1002/2016MS000785.

Vimont, D. (accessed 2018), Dan Vimont's Matlab Libraries, <http://www.aos.wisc.edu/~dvimont/matlab/>.

Visioni, D., G. Pitari, and V. Auqila (2017), Sulfate geoengineering: a review of the factors controlling the needed injection of sulfur dioxide, *Atmospheric Chemistry and Physics*, 17, 3879–3889, doi:10.5194/acp-17-3879-2017.

Visioni, D., G. Pitari, and G. di Genova (2018), Upper tropospheric ice sensitivity to sulfate geoengineering, *Atmospheric Chemistry and Physics Discussions*, 2018, 1–37, doi:10.5194/acp-2018-107.

Waliser, D. E., and C. Gautier (1993), A satellite-derived climatology of the ITCZ, *Journal of Climate*, 6(11), 2162–2174, doi:10.1175/1520-0442(1993)006<2162:ASDCOT>2.0.CO;2.

Watanabe, S., et al. (2011), MIROC-ESM 2010: model description and basic results of CMIP5-20c3m experiments, *Geoscientific Model Development*, 4(4), 845–872, doi:10.5194/gmd-4-845-2011.

Webb, M., C. Senior, S. Bony, and J.-J. Morcrette (2001), Combining ERBE and ISCCP data to assess clouds in the Hadley Centre, ECMWF and LMD atmospheric climate models, *Climate Dynamics*, 17(12), 905–922, doi:10.1007/s003820100157.

Wetherald, R. T., and S. Manabe (1975), The effects of changing the solar constant on the climate of a general circulation model, *Journal of the Atmospheric Sciences*, 32, 2044–2059.

Wood, R., and C. S. Bretherton (2006), On the relationship between stratiform low cloud cover and lower-tropospheric stability, *Journal of Climate*, 19, 6425–6432.

World Meteorological Organization (2017), WMO Greenhouse Gas Bulletin, No. 13, https://library.wmo.int/opac/doc_num.php?explnum_id=4022.

Yang, F., A. Kumar, M. E. Schlesinger, and Q. Wang (2003), Intensity of hydrological cycles in warmer climates, *Journal of Climate*, 16, 2419–2423.

Yoshimori, M., and A. J. Broccoli (2008), Equilibrium response of an atmosphere–mixed layer ocean model to different radiative forcing agents: Global and zonal mean response, *Journal of Climate*, 21(17), 4399–4423, doi:10.1175/2008JCLI2172.1.

Zelinka, M. D., S. A. Klein, and D. L. Hartmann (2012a), Computing and partitioning cloud feedbacks using cloud property histograms. Part II: Attribution to changes in cloud amount, altitude, and optical depth, *J. Climate*, 25, 3736–3754.

Zelinka, M. D., S. A. Klein, and D. L. Hartmann (2012b), Computing and partitioning cloud feedbacks using cloud property histograms. Part I: Cloud radiative kernels, *J. Climate*, 25, 3715–3735.

Zhang, M., and Y. Huang (2014), Radiative forcing of quadrupling CO₂, *Journal of Climate*, 27(7), 2496–2508, doi:10.1175/JCLI-D-13-00535.1.

Appendix A

RESULTS FROM CH. 2 USING A DRY INSTEAD OF A MOIST EBM

There were several errors in the original version of Chapter 2 that were noticed because of comments made by one of the reviewers. Most notably, the EBM was originally run with only 1% of the specific humidity that it should have had, due to a unit conversion error (specifying saturation vapor pressure in hPa instead of Pa) in my Python implementation of the EBM. Therefore, I was effectively running a dry EBM instead of a moist EBM. The original results obtained in this configuration are interesting because comparing the results from the moist versus the dry EBM can shed light on the role of moisture transport in the response of meridional energy transport to various forcings.

This error was noticed because of a different error that the reviewer pointed out. Originally, when running the “greenhouse”, “all_G1”, and “all_4xCO₂” EBM attribution experiments, I re-fit both coefficients a and b in the OLR fit equation ($\text{OLR} = aT_s - b$) to account for the enhanced greenhouse effect, instead of just b . (The values of the coefficients fit this way are listed in Table A.1.) I did this because I could not originally reproduce the inter-model spread associated with the equivalent of the “greenhouse” experiment shown in Figure 4 of *Hwang and Frierson* (2010) when re-fitting only b . The reviewer pointed out that comparing the values of b and b' when doing this implied unreasonable values for the CO₂ radiative forcing from CO₂ quadrupling, ranging from 0 to -16 W m⁻². Also, Dargan Frierson confirmed to me that *Hwang and Frierson* (2010) did in fact re-fit only b , as stated in that paper. I then revisited the question of why I could not produce non-negligible energy transport changes from the “greenhouse” experiment this way, which led to the discovery of the EBM error.

With a dry EBM, changing only the intercept in the OLR- T_s linear fit would not be expected to change meridional energy transport, because the net energy input to the atmosphere would

Table A.1: Values of fit coefficients for clear-sky OLR as a function of temperature used in the original EBM analysis, when I re-fit both a and b instead of just b .

Model	a ($\text{W m}^{-2} \text{K}^{-1}$)	a' (G1)	a' (abrupt4xCO ₂)	b (W m^{-2})	b' (G1)	b' (abrupt4xCO ₂)
CanESM-2	2.0667	1.9934	2.0139	326.83	314.74	320.04
CCSM4	2.1604	2.0898	2.0946	350.06	338.74	341.84
CESM-CAM5.1-FV	2.0724	1.9907	1.9837	328.98	315.19	316.62
HadGEM2-ES	2.1531	2.0942	2.1200	349.37	341.00	349.61
IPSL-CM5A-LR	2.2149	2.1429	2.1504	363.39	350.70	352.36
MIROC-ESM	2.0512	1.9585	1.9732	327.40	310.59	313.99
MPI-ESM-LR	2.0157	1.9284	1.9314	315.55	300.22	300.50
NorESM1	2.1403	2.0665	2.1043	346.36	333.94	344.57

be having the same constant subtracted from it at all latitudes, so that the gradient would not change. With a moist EBM, however, due to the nonlinear dependence of saturation vapor pressure on temperature, the same decrease in OLR causes a greater increase in MSE in the tropics than near the poles, leading to increased poleward energy transport. Allowing the slope of the OLR- T_s fit to change also allows for meridional energy transport to increase in the greenhouse experiment, but not in a way consistent with physics.

Figures A.1 through A.4 show the equivalents of Figures 2.7, 2.10, 2.11, and 2.12 with the EBM having been run in the (accidental) dry configuration. Even in the dry configuration, there is a good correlation between the change in energy transport calculated by the EBM and that diagnosed from the GCM output (Figure A.1), but the change in energy transport across 40° N or S in G1 and abrupt4xCO₂ is only about half what it is in the moist configuration. For G1 - piControl, the change in mid-latitude energy transport is consistently less in the dry EBM than in the GCMs (Figure A.1b), whereas it is consistently greater in the moist EBM than in the GCMs (Figure 2.7b). Also, for abrupt4xCO₂ - piControl, the dry EBM predicts a decrease in poleward energy transport across 40° S in most models (Figure A.1c), but including moisture transport results in an increase in poleward energy transport across 40°N and S in all models and brings

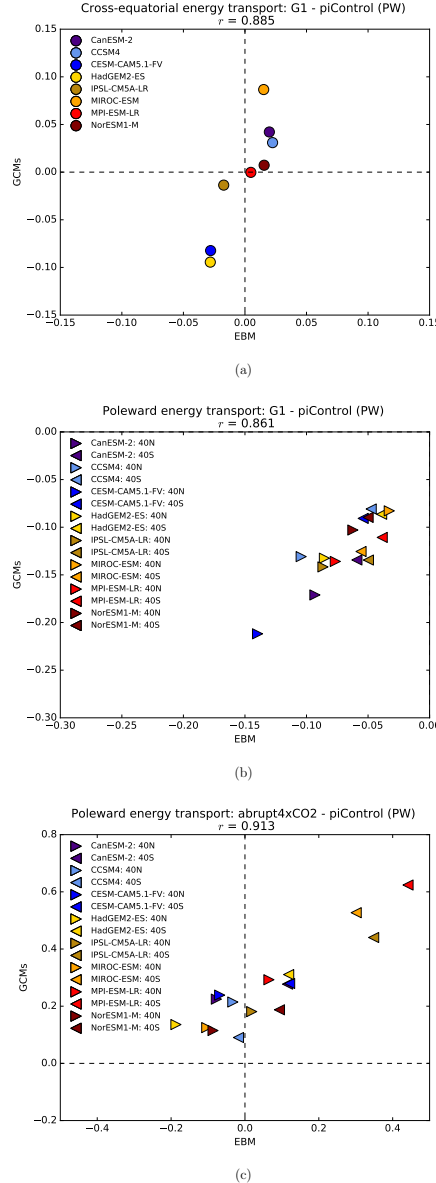


Figure A.1: Meridional energy transport changes calculated by dry EBM (x -axis) versus those diagnosed from the GCM output (y -axis). (a): northward energy transport across the equator, for G1 minus piControl; (b): poleward energy transport changes across 40° N and S, for G1 minus piControl; (c): as in (b) but for abrupt4xCO₂ minus piControl. *cf.* Figure 2.7.

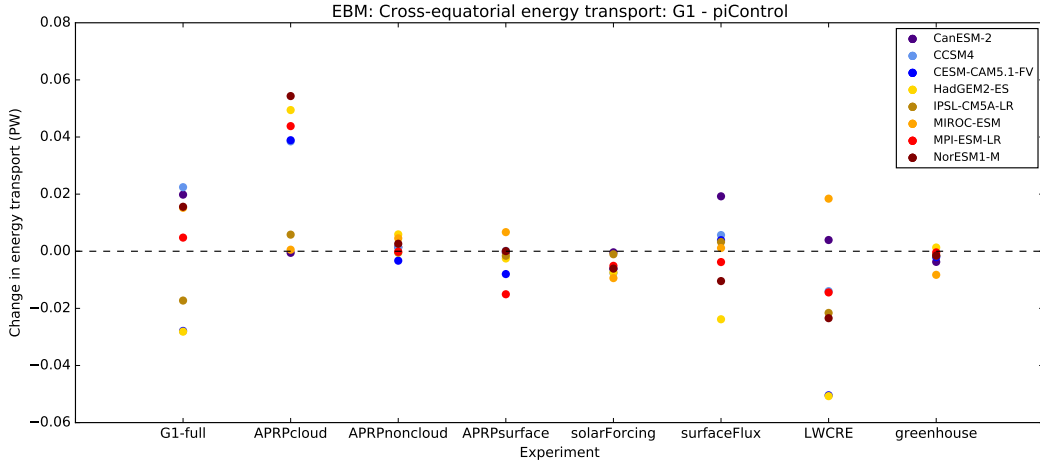


Figure A.2: Changes in northward cross-equatorial energy transport calculated by dry EBM for G1 minus piControl in various attribution experiments. *cf.* Figure 2.10. The “all_G1” experiment was called “G1-full” when this plot was made. OLR fit coefficients in the “greenhouse” and “G1-full” experiments involved re-fitting both the slope and intercept of the OLR- T_s fit (Table A.1), versus only the intercept for the version in Chapter 2 (Table 2.2).

the changes in this experiment closer into line with the GCMs (Figure 2.7c).

For the attribution experiments for changes in cross-equatorial energy transport, the results are generally fairly similar using the dry (Figure A.2) versus the moist (Figure 2.10) EBM. For most experiments, the inter-model spread is similar in the two versions. For the solarForcing experiment, however, there is much greater inter-model spread using the moist EBM. This may be because the solar forcing is particularly concentrated in the tropics, and changes in moisture in the tropics (which can occur due to a uniform percentage change in the solar constant if there are hemispheric asymmetries in the albedo) would affect latent energy transport across the equator more than feedbacks such as surface albedo that primarily act in higher latitudes. Comparing these figures also illustrates how the greenhouse experiment produces greater inter-model spread when re-fitting only the intercept of the OLR- T_s fit and using a moist EBM than when re-fitting both the slope and intercept and using a dry EBM. (When re-fitting only the

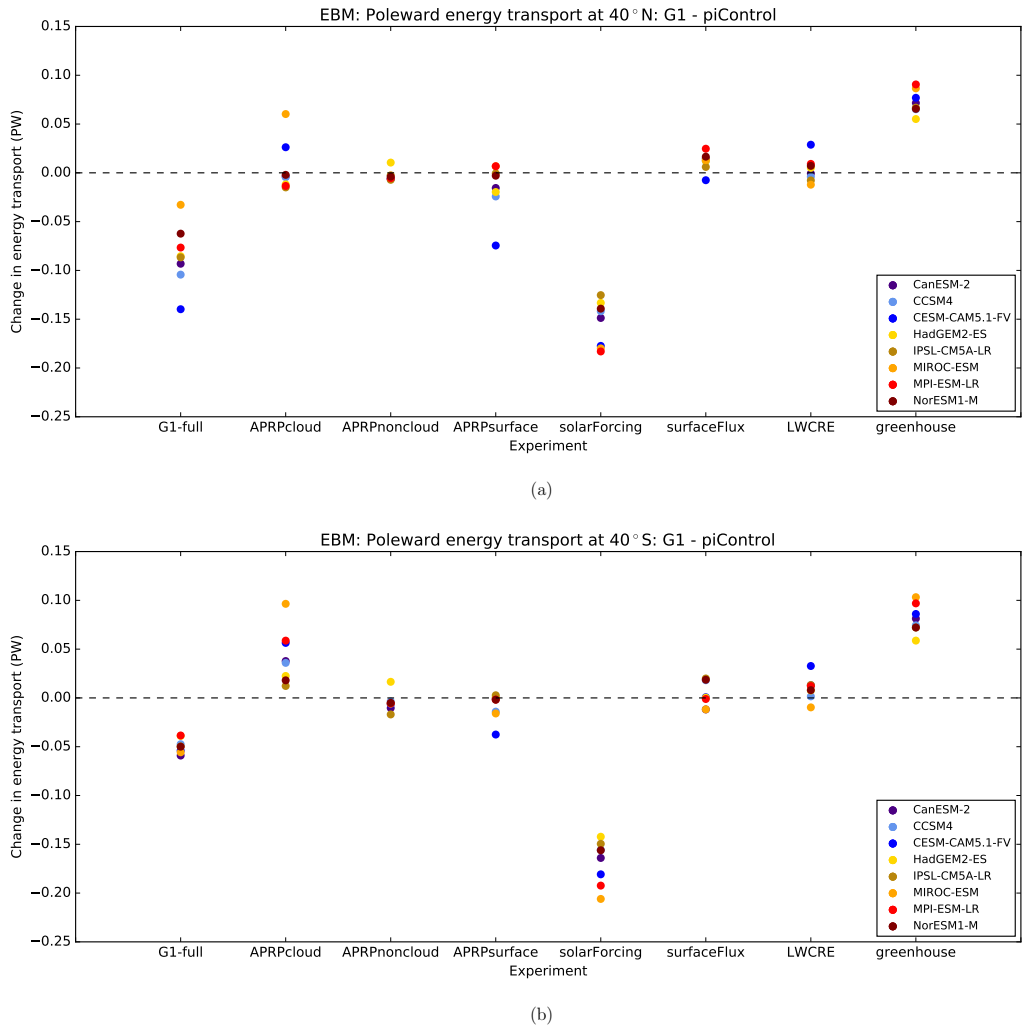


Figure A.3: As in Figure A.2 but for changes in poleward atmospheric energy transport across 40°N (a) and 40°S (b), for G1 minus piControl. *cf.* Figure 2.11.

slope before the moisture bug was fixed, the dots for the greenhouse experiment were all virtually zero, with any differences due to the 1% of normal moisture that was included in the EBM.)

For the changes in energy transport across 40°N and S in G1 - piControl in the various attribution experiments, the results from the dry EBM (Figure A.3) are similar to those from the moist EBM (Figure 2.11), apart from having re-scaled the y-axis since the changes in energy

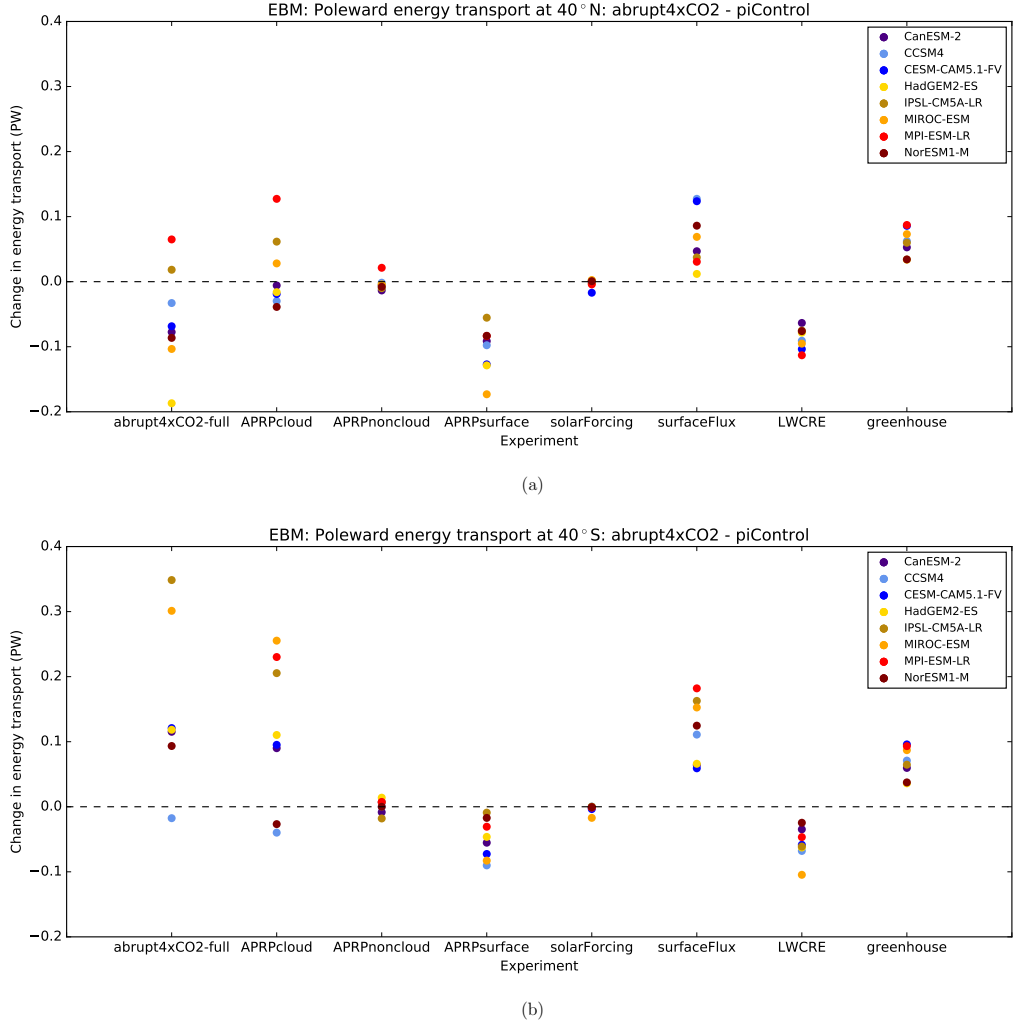


Figure A.4: As in Figure A.3 but for abrupt4xCO2 minus piControl. *cf.* Figure 2.12.

transport are consistently greater when latent heat transport is taken into account. There is a similar story for abrupt4xCO2 - piControl (Figures A.4 and 2.12), except that there are positional shifts in the dots for the all_4xCO2 and greenhouse experiments, in which the OLR- T_s fit coefficients were changed as well as the treatment of moisture.

Overall, the major conclusions of the paper were not qualitatively changed whether a dry or a moist EBM was used, which was fortunate since I did not have to do much rewriting. The sim-

ilarity of the relative changes in each of the experiments shows that perturbations to the atmosphere's energy budget must be resolved by changes in energy transport, whether atmospheric moisture content is allowed to adjust or not. A perturbation that varies greatly between models, such as that associated with the SW cloud adjustment, will cause a larger inter-model spread in the EBM-derived energy transport changes than a perturbation that does not vary much between models, such as the SW non-cloud atmospheric adjustment, regardless of whether latent heat transport is allowed to contribute to the resolution of the energy imbalance. The same logic applies to perturbations causing large multi-model mean changes, such as the solarForcing experiment for mid-latitude transport in the G1 scenario.

It is not surprising that overall changes in energy transport are greater when latent heat transport is included than when this important medium of energy transport is left out entirely. That the *ratios* of the changes in energy transport in the different experiments and models are so similar regardless of the inclusion or exclusion of moisture transport is striking, especially considering the nonlinearity of the dependence of moisture on temperature. This may be because the changes in energy transport in these experiments are small compared to the total energy transport, so there is not much room for the higher-order terms in the power series expansion of the exponential function to become very important.

Appendix B

TIME SERIES PLOTS OF APRP RESULTS

One question related to the exploration of radiative adjustments in the G1 experiment is how consistent the adjustments are over time. This has implications for whether it is necessary to draw a distinction between “rapid adjustments” and “radiative adjustments” more generally in this context, and for how much the G1 experiment can tell us about rapid adjustments in forcing scenarios that, unlike G1, involve a global mean temperature change.

To investigate this question, Figure B.1 shows time series plots of the three SW radiative adjustments calculated using the APRP method in each model. I made these plots by repeatedly running the APRP code taking the one-year averages for each year of the G1 experiment as the perturbation climate, rather than an average of years 11-50 as in Chapters 2 and 3, and using the first 40 years of piControl as the baseline climate. The radiative adjustments are quite consistent throughout the experiment. None of the models have any adjustments with long-term trends that exceed the interannual variability, with the exception of the non-cloud atmosphere and surface albedo adjustments for HadGEM2-E, which has the largest global mean temperature increase in G1 at 0.24 K (Table 1.2). This implies that we do not need to worry about the time scale we are talking about when discussing radiative adjustments in G1, and suggests that radiative adjustments calculated in G1 are relevant for understanding differences between rapid adjustments to solar and CO₂ forcings. However, there are some cases, such as the cloud adjustment in the CESM and HadGEM2-ES models, where the adjustment in the first year is either the weakest or the strongest of the entire 50-year time period, illustrating that the changes taking place at the very beginning of the experiment are not well resolved by the annual averaging time scale and suggesting that similar changes are taking place in the first few months in the other models.

The time series plots also help us interpret the physical causes of the radiative adjustments. Since the ocean has a high heat capacity, it takes a long time to change sea surface temperatures. The lack of a drift in the cloud and surface albedo responses over time in most models suggests that the changes in cloud properties and surface albedo in G1 are not the result of local changes in sea surface temperatures, *i.e.* warming near the poles and cooling near the tropics. To verify this, it would be useful to look at time series of SST changes in G1 in different parts of the ocean, to see how long the SST changes take to manifest.

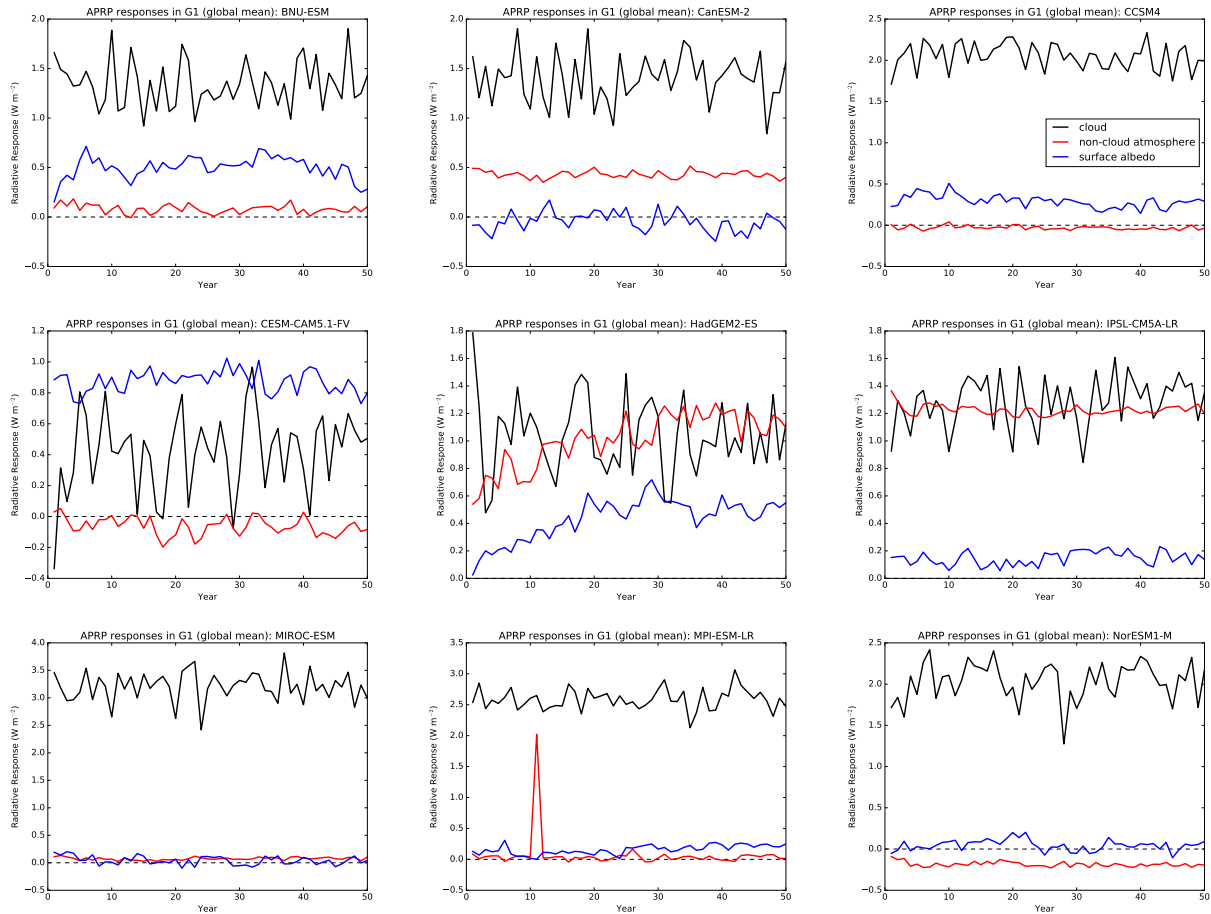


Figure B.1: Global mean SW radiative responses calculated using APRP for each year of G1 minus the piControl baseline, in each of nine models.